



# **Image guided surgical navigation for pedicle screw placement**

**Anup Saha**

Thesis to obtain the Master of Science Degree in

## **Mechanical Engineering**

Supervisors: Prof. Jorge Manuel Mateus Martins  
Prof. Dario Petri

### **Examination Committee**

Chairperson: Prof. Carlos Baptista Cardeira  
Supervisor: Jorge Manuel Mateus Martins  
Member of the Committee: Prof. João Rogério Caldas Pinto

**November 2018**



Dedicated to my family.



## Acknowledgments

Firstly, I would like to express my sincere gratitude to my advisor Prof Jorge Martins for the guidance, for the ideas provided during this thesis and for constantly challenging me to overcome myself. I would like to thank Prof. Dario Petri for his willingness and availability to supervise my thesis.

I express my very profound gratitude to my parents for providing me with constant support and continuous encouragement, specially to my mother and father who always encouraged me 'you can do it'. They were my source of energy that has been present throughout my years.

I thank my friend Adnan for the motivation, support, and for all the fun. we have had in all these years, my friend Tomas for the friendship, motivation and relaxing moments, Lisa di and Gias vai who even with the distance makes themselves present, and also for all my friends that were not mentioned, however, have been important to make my life, to all of them I am forever grateful.



## **Abstract**

Image guided navigation system has revolutionized the field of surgery. Surgical navigation system helps surgeon to enhance their knowledge about patient's anatomy and to perform pre-operative diagnosis and planning. The aim of this study is to develop an image guided surgical navigation system for pedicle screw placement. Firstly, a computed tomography (CT) imaging based virtual 3D model of pig spine is reconstructed, where CT images are segmented based on Hounsfield unit (HU) intensity values as threshold. Subsequently, Landmark registration was done between landmarks on pedicle screw and landmarks on pedicle of vertebra model developed from CT, where four landmarks were chosen respectively on pedicle screw and on pedicle of vertebrae. The pedicle screws were successfully placed into the pedicles of vertebra using the Landmark registration. Finally, a non-rigid landmark registration is done between US imaging based inverse image of vertebra and CT model of vertebra.

**Key words:** Image guided surgical navigation system, Hounsfield unit (HU) intensity value, CT images, Pedicle screw, Landmark registration, US imaging.



# Table of contents

Title	Page
Acknowledgments.....	v
Abstract.....	vii
List of Table .....	xi
List of Figure .....	xiii
Nomenclature .....	xvii
<b>1. Introduction</b> .....	<b>1</b>
1.1 The Thesis Structure .....	1
1.2 Vertebrae .....	2
1.3 Surgical Navigation Systems .....	3
1.3 Goal of the Thesis.....	3
<b>2. Image Processing Technique</b> .....	<b>5</b>
2.1 Image.....	6
2.2 Source of Digital Image .....	6
2.2.1 Gamma Ray Imaging .....	7
2.2.2 X-Ray Imaging .....	8
2.2.3 Ultraviolet Band Imaging .....	8
2.2.4 Visible Light.....	9
2.2.4.1 RGB Color Space.....	9
2.2.5 Infrared Band Imaging.....	10
2.2.6 Microwave Band Imaging.....	11
2.2.7 Radio Band Imaging.....	11
2.2.8 Ultrasound Imaging .....	12
2.3 Morphological Image Processing .....	12
2.3.1 Fundamental Morphological Operations .....	13
2.4 Image Segmentation.....	14
<b>3. Medical Imaging</b> .....	<b>15</b>
3.1 Computed tomography (CT) scan .....	15
3.2 CT Image acquisition .....	20
3.3 Ultrasound Imaging.....	20
3.4 Ultrasound Imaging acquisition.....	21
3.5 DICOM Image Format .....	22
<b>4. Acquiring a 3d Model</b> .....	<b>23</b>
4.1 Volume Reconstruction from CT Scan .....	23
4.2 Cropping CT.....	24
4.3 Segmentation CT .....	25
4.3.1 Threshold based segmentation.....	26

4.4 3D Model Reconstruction from Ultrasound Imaging.....	27
<b>5. Image Registration .....</b>	<b>31</b>
5.1 Closed-Form Solution .....	31
5.1.1 Finding the Translation.....	32
5.1.2 Centroids of the sets of measurements .....	32
5.1.3 Finding the Scale .....	33
5.1.4 Symmetry in Scale .....	34
5.1.5 Unit Quaternions and Rotation.....	35
5.1.6 Composition of Rotation.....	36
5.1.8 Matrix of Sums of Product.....	37
5.1.9 Eigenvector Maximizes Matrix Product.....	37
5.1.10 Rotation in the Plane.....	38
5.2 Rigid Registration .....	39
5.2.1 Point Cloud based Rigid Registration .....	39
5.3 Point Cloud based Affine Registration .....	40
5.4 Non-Rigid Registration (NRR): .....	41
<b>6. Results and Discussion .....</b>	<b>45</b>
6.1 Pedicle Screw Placement Process.....	45
6.1.1 Fiducial Registration.....	46
6.1.2 Discussion .....	60
6.2 Registration between CT and US .....	61
6.1.2 Discussion .....	62
<b>7. Conclusions and Future Work .....</b>	<b>63</b>
<b>Bibliography.....</b>	<b>65</b>
<b>Picture Reference .....</b>	<b>69</b>

## List of Table

Table 2. 1: RGB value for different color.....	10
Table 3. 1: HU Values .....	19
Table 3. 2: Sound wave velocity .....	21
Table 4. 1: All vertebrae dimension and frame location.....	24



# List of Figure

Fig 1. 1: The five regions of the spinal column <sup>(7)</sup> .....	2
Fig 1. 2: Different component of vertebrae <sup>(8)</sup> .....	2
Fig 2. 1: Fundamental steps in image proceesing <sup>[2]</sup> .....	5
Fig 2. 2: a) Digital image <sup>[1]</sup> , b) pixel (x, y) <sup>[2]</sup> .....	6
Fig 2. 3: The electromagnetic spectrum. The visible spectrum is shown zoomed to facilitate explanation, but that the visible spectrum is a rather narrow portion of the EM spectrum <sup>[2]</sup> .....	7
Fig 2. 4: a) Gamma-ray imaging a) in nuclear medicine b) in radioisotope diagnostic <sup>[2]</sup> .....	7
Fig 2. 5: Different parts of the X-ray spectrum <sup>[4]</sup> .....	8
Fig 2. 6: Examples of ultraviolet imaging a) Normal corn, b) Smut corn <sup>[2]</sup> .....	8
Fig 2. 7: Examples of visible light image <sup>[2]</sup> .....	9
Fig 2. 8: RGB color space <sup>(3)</sup> .....	9
Fig 2. 9: Examples of infrared (“thermal”) image <sup>[2]</sup> .....	10
Fig 2. 10: Spaceborne radar image of mountains in southeast Tibet. <sup>[2]</sup> .....	11
Fig 2. 11: MRI images of a human a) knee, b) spine, and c) brain <sup>[2]</sup> .....	11
Fig 2. 12: a) Ultrasound image acquisition device, b) Ultrasound Baby image during pregnancy <sup>[2]</sup> .....	12
Fig 2. 13: Probing of an image with a structuring element .....	12
Fig 2. 14: examples dilation operation <sup>(12)</sup> a) original image, b) Dilated image .....	13
Fig 2. 15: examples erosion operation <sup>(12)</sup> a) original image, b) Eroded image .....	14
Fig 3. 1: CT scanner <sup>(4)</sup> .....	16
Fig 3. 2: Functional flowchart of CT scanner <sup>(4)</sup> .....	17
Fig 3. 3: Volume construction in CT scanner <sup>(4)</sup> .....	17
Fig 3. 4: slice reconstruction by overlapping all the views at 22.5-degree and 45-degree step over the object, and 3d representation of the slice <sup>(6)</sup> .....	18
Fig 3. 5 : X-rays attenuation projection <sup>(5)</sup> .....	18
Fig 3. 6: Abdominal ultrasonography <sup>(9)</sup> .....	20
Fig 3. 7 : Ultrasound imaging system <sup>(10)</sup> .....	22
Fig 4. 1: Phantom column <sup>[28]</sup> .....	23
Fig 4. 2: Reconstructed Volume: a) 3D grid or volume is obtained by stacking all the slices together, b) the same volume using a different colormap for better visualization the vertebrae anatomy. C) cropped vertebrae .....	24
Fig 4. 3: a) Top left: red screen shows Left axis, b) Bottom left: yellow screen shows Superior axis, ..	25
Fig 4. 4: Segmented vertebra: a) Top left: shows Left axis, b) Bottom left: yellow screen shows .....	26
Fig 4. 5: 3d reconstructed model: a) Top left: red screen shows Left axis, b) Bottom left: yellow screen .....	27

Fig 4. 6: (a) echograph used to acquire the images of US-linear probe and coupled to an instrument Spectra Polaris system. (b) Framegrabber used to view the Pictures of the computer <sup>[28]</sup> .....	27
Fig 4. 7: Reconstructed Volume: a) 3D grid or volume is obtained by stacking all the ultrasound slices together, b) the same volume using a different colormap for better visualization the inverse structure of the vertebra no 2 and 3. C) cropped the region of interest 25 115.....	28
Fig 4. 8: Segmented ultrasound imaging: a) Top left: red screen shows Left axis, b) Bottom left: yellow .....	28
Fig 4. 9: 3d reconstructed model: a) Top left: red screen shows Left axis, b) Bottom left: yellow screen .....	29
Fig 5. 1: The coordinates of a number of points is measured in two different coordinate systems. <sup>[30]</sup> 32	
Fig 5. 2: a) Two coordinate systems have been aligned and superimposed. b) The second rotation, when both sets of measurements are coplanar, is about the normal of one of the planes. <sup>[30]</sup> .....	38
Fig 5. 3: Transformation types <sup>(13)</sup> .....	41
Fig 5. 4: Non-rigid registration: Vector field (aka deformation field) T is computed from A to B <sup>(15)</sup> .....	42
Fig 5. 5: Graphical representation of the energy term for point <sup>(14)</sup> .....	42
Fig 5. 6: Graphical representation of the energy term for plane <sup>(14)</sup> .....	42
Fig 5. 7: Graphical representation of the term Efit <sup>(14)</sup> .....	43
Fig 6. 1: Landmarks on pedicle screw .....	45
Fig 6. 2: Left axis view of left pedicle of vertebra 1: a) Top left: Landmarks on vertebra, b) Top right: Pedicle screw placed into vertebra, c) Bottom left: Translated Landmarks on pedicle screw, and d) Bottom right: Vertebra after the registration.....	46
Fig 6. 3: Left axis view of right pedicle of vertebra 1: a) Top left: Landmarks on vertebra, b) Top right: Pedicle screw placed into vertebra, c) Bottom left: Translated Landmarks on pedicle screw, and d) Bottom right: Vertebra after the registration.....	47
Fig 6. 4: Left axis view of left pedicle of vertebra 2: a) Top left: Landmarks on vertebra, b) Top right: Pedicle screw placed into vertebra, c) Bottom left: Translated Landmarks on pedicle screw, and d) Bottom right: Vertebra after the registration.....	48
Fig 6. 5: Left axis view of right pedicle of vertebra 2: a) Top left: Landmarks on vertebra, b) Top right: Pedicle screw placed into vertebra, c) Bottom left: Translated Landmarks on pedicle screw, and d) Bottom right: Vertebra after the registration.....	49
Fig 6. 6: Left axis view of left pedicle of vertebra 3: a) Top left: Landmarks on vertebra, b) Top right: Pedicle screw placed into vertebra, c) Bottom left: Translated Landmarks on pedicle screw, and d) Bottom right: Vertebra after the registration.....	50
Fig 6. 7: Left axis view of right pedicle of vertebra 3: a) Top left: Landmarks on vertebra, b) Top right: Pedicle screw placed into vertebra, c) Bottom left: Translated Landmarks on pedicle screw, and d) Bottom right: Vertebra after the registration.....	51

Fig 6. 8: Left axis view of left pedicle of vertebra 4: a) Top left: Landmarks on vertebra, b) Top right: Pedicle screw placed into vertebra, c) Bottom left: Translated Landmarks on pedicle screw, and d) Bottom right: Vertebra after the registration.....	52
Fig 6. 9: Left axis view of right pedicle of vertebra 4: a) Top left: Landmarks on vertebra, b) Top right: Pedicle screw placed into vertebra, c) Bottom left: Translated Landmarks on pedicle screw, and d) Bottom right: Vertebra after the registration.....	53
Fig 6. 10: Left axis view of left pedicle of vertebra 5: a) Top left: Landmarks on vertebra, b) Top right: Pedicle screw placed into vertebra, c) Bottom left: Translated Landmarks on pedicle screw, and d) Bottom right: Vertebra after the registration.....	54
Fig 6. 11: Left axis view of right pedicle of vertebra 5: a) Top left: Landmarks on vertebra, b) Top right: Pedicle screw placed into vertebra, c) Bottom left: Translated Landmarks on pedicle screw, and d) Bottom right: Vertebra after the registration.....	55
Fig 6. 12: Left axis view of left pedicle of vertebra 6: a) Top left: Landmarks on vertebra, b) Top right: Pedicle screw placed into vertebra, c) Bottom left: Translated Landmarks on pedicle screw, and d) Bottom right: Vertebra after the registration.....	56
Fig 6. 13: Left axis view of right pedicle of vertebra 6: a) Top left: Landmarks on vertebra, b) Top right: Pedicle screw placed into vertebra, c) Bottom left: Translated Landmarks on pedicle screw, and d) Bottom right: Vertebra after the registration.....	57
Fig 6. 14: Left axis view of left pedicle of vertebra 7: a) Top left: Landmarks on vertebra, b) Top right: Pedicle screw placed into vertebra, c) Bottom left: Translated Landmarks on pedicle screw, and d) Bottom right: Vertebra after the registration.....	58
Fig 6. 15: Left axis view of right pedicle of vertebra 7: a) Top left: Landmarks on vertebra, b) Top right: Pedicle screw placed into vertebra, c) Bottom left: Translated Landmarks on pedicle screw, and d) Bottom right: Vertebra after the registration.....	59
Fig 6. 16: a) Top left: intersection markups placed on vertebra in posterior view, b) Bottom left: Pedicle screw placed into semitransparent vertebra posterior view, c) Top right: Pedicle screw placed into vertebra posterior view, and d) Bottom right: Pedicle screw placed into semitransparent vertebra left view .....	60
Fig 6. 17: Vertebra no 2 and 3: a) CT model, b) US model inverse image of the vertebra .....	61
Fig 6. 18: Registration between CT model and US model: a) view from Superior axis, b) view from Inferior axis.....	61
Fig 6. 19: Registration between CT model and US model: a) Top left: view from Left axis, b) Bottom left: view from Posterior axis, c) Top right: view from Right axis, and d) Bottom right: view from Anterior axis .....	62



# Nomenclature

## Subscripts

HU Hounsfield unit Intensity Value

3D Three Dimensional

CT Computed Tomography

DICOM Digital Imaging and Communication in Medicine

DOF Degree of freedom

HU Hounsfield scale

mm millimeter

m/s meter per second

MRI Magnetic resonance imaging

NMV Net magnetization vector

PET Positron Emission Tomography

RF Radio-frequency

ROI Region of interest

SE Structural element

SPECT Single Proton Emission Computed Tomography

ACR American college of radiology

NEMA National electrical manufacturers association

NRR Non-Rigid Registration

RMS Root Mean Square



# Chapter 1

## Introduction

Surgery involves higher risk than other medical treatment [39]. The use of image guided tracking technology and navigation system reduce the health risk and increase the treatment accuracy. Image guided surgical navigation is the process that uses image processing techniques for developing medical image based virtual 3D model. While, 3D model allows surgeon to make pre-operative planning.

Pedicle screw placement is the treatment that performed when a person is subjected to column fusion surgery due to a degenerative disease traumatic, neoplastic, or infectious or due to a deformation of the spine, such as scoliosis. It is a surgery that required navigation system for tracking specific point and orientation on the vertebra to place pedicle screws. The main function of pedicle screws placement is to stabilize the spine by fixing and / or joining neighboring vertebrae. However, this process involves high complexity due to vertebrae has complex anatomy and vertebrae holds the vital vascular and the spinal cord [28]. Image guided surgical navigation is used to handle this complex process. It allows surgeon to visualize the virtual model before surgery and to visualize the trajectory of the screw within the real-time patient's body. As a result. Pedicle screw placement become more accurate and reliable [40].

The aim of this study is to present the methods used for medical images acquisition, processing and 3D model construction in order to help surgeon for pre-operative planning before the surgery and real-time tracking during the surgery.

## 1.1 The Thesis Structure

The thesis is organized as follows: the first chapter is to understand what pedicle screw placement is, and what is surgical navigation. In addition, the goal of the thesis is presented. The chapter two presents the image processing technique which includes digital image, source of lights, morphological images processing and image segmentation. In chapter three medical imaging technologies and their application are presented. The chapter four presents how to construct a 3d model for vertebrae, which includes volume reconstruction from CT scan, structure and composition, cropping, HU Intensity threshold-based segmentation. The chapter five presents the image registration which includes Closed-Form Solution for Landmark registration and the description of the Rigid, Affine and Non-Rigid method of registration. The sixth Chapter, Results and discussion on the results obtained from Landmark registration Finally, the seventh chapter, Conclusions, presents the conclusion of the work and propose a future work to be developed.

## 1.2 Vertebrae

Vertebrae are complex structure composed of irregular bones that interlock each other for forming the spinal column, Fig 1.1. There are total 33 vertebrae in human spinal column, where seven cervical vertebrae, twelve thoracic vertebrae, five lumbar vertebrae, five fused vertebrae of the sacral region and four fused vertebrae forming coccyx. Each of the region has their specific function. The mobility in spine is possible for facet joints of interconnected vertebrae.

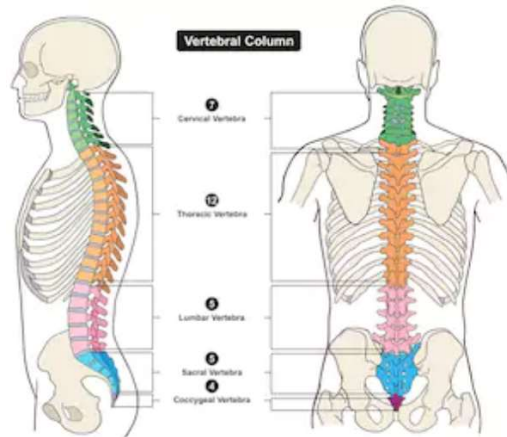


Fig 1. 1: The five regions of the spinal column <sup>(7)</sup>

The function of vertebral components are very essential, where vertebral body bear load, vertebral arch protect spinal cord, and transverse process for ligament attachment. Fig 1.2 shows different components of vertebrae.

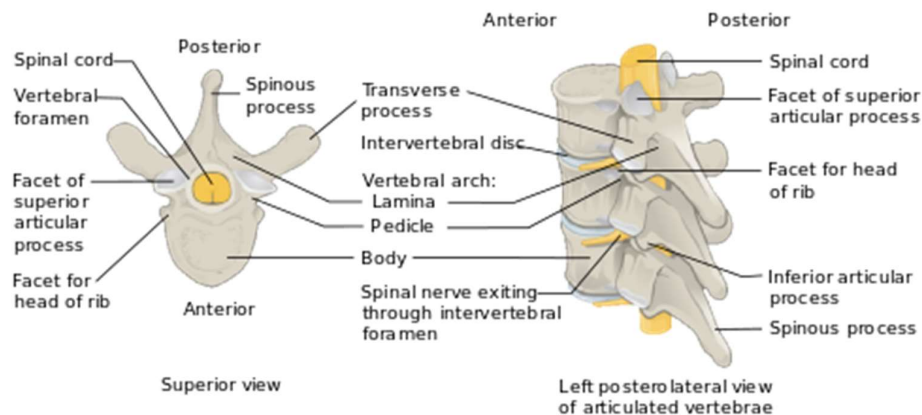


Fig 1. 2: Different component of vertebrae <sup>(8)</sup>

The pedicle is a cylindrical stub of bone that form the vertebral arch by connecting the lamina to the vertebral body. A hollow archway is formed by joining two short, stout processes extend from the sides of the vertebral body with laminae (broad flat plates of bone). It protects the spinal cord. The pedicles also form the base of the articular processes which are the points of articulation for the ribs. Pedicle screws have been used as adjuncts to spinal fusion surgery as a means of anchoring a spinal segment.

## **1.3 Surgical Navigation Systems**

Over the past decade, with the improvement of computer technology, navigation has become an integral part in medical surgery [38]. Surgical navigation is a technique that allows surgeon to precisely track the location of the surgical instruments relative to real-time patient's anatomy. The most important component of surgical navigation is to develop an accurate 3D model of the patient, where computed tomography (CT) or magnetic resonance imaging (MRI) or any other type of examination is used to obtain images of the area to be operated. This 3D model helps surgeon to make pre-operative planning. Here, surgeon gets the information such as position, length and diameter of the area of operation. In addition, real-time surgical navigation system is considered for tracking, since there may be anatomical changes during surgery. During surgery, the actual organ is registered to the virtual model, through real time tracking systems using ultrasound imaging technique. Thus, the surgeon can visualize the position of the instrument relative to the patient anatomy in the virtual model. Here, in this thesis, the pedicle screw placement navigation is based on registration between CT imaging-based 3D virtual model and ultrasound imaging model of pig vertebrae.

### **1.3 Goal of the Thesis**

In this thesis, it is intended to implement a surgical navigation system for assisting placement of pedicle screws in the spine phantom of a pig, using the 3D slicer open-source software ([www.slicer.org](http://www.slicer.org)). The first part of the work was the development of a system based on computerized tomography (CT) preoperative. Through these images is intended to reconstruct a 3D model of the column, so it can view the location of the surgical instrument in relation to the actual column. Secondly, a HU intensity based automated segmentation is done for finally reconstructing 3D virtual model of vertebrae column. Thirdly, point to point based landmark registration is done between landmarks on pedicle screw and landmarks on pedicle wall. By using the result of registration all the pedicle screws are placed into vertebrae. Lastly, non-rigid based landmark registration is done between CT imaging of vertebrae and ultrasound imaging of vertebrae.



# Chapter 2

## Image Processing Technique

In 1960s, digital image processing techniques were developed at the Jet Propulsion Laboratory, Massachusetts Institute of Technology, Bell Laboratories and University of Maryland [1]. The initial application of image processing technology includes photo enhancement, satellite imagery, video phone, character recognition and medical imaging. It was moderately expensive. During 1970s, dedicated hardware and cheaper computer became widely available as a result real time images could be processed for television standards conversion. As general-purpose computer became faster from the beginning of twenty first century, digital image processing has become most common in use and cheaper.

Image processing is a method where an image is acquired, analyzed and manipulated for getting an enhanced image or extracting some useful information from it. There are two types of image processing: digital image processing and analogue image processing. Analog image processing is visual techniques where image analysts use personal knowledge and various fundamentals of interpretation for the hard copies like printouts and photographs.

Digital image processing is a technique that manipulate digital image using computers. In this image processing technique digital image go through the pre-processing phase, enhancement phase, and display & information extraction phase. This chapter describes fundamental steps in image processing technique, which include source of digital image, morphological processing and image segmentation. Fig 2.1 represents fundamental steps in image processing.

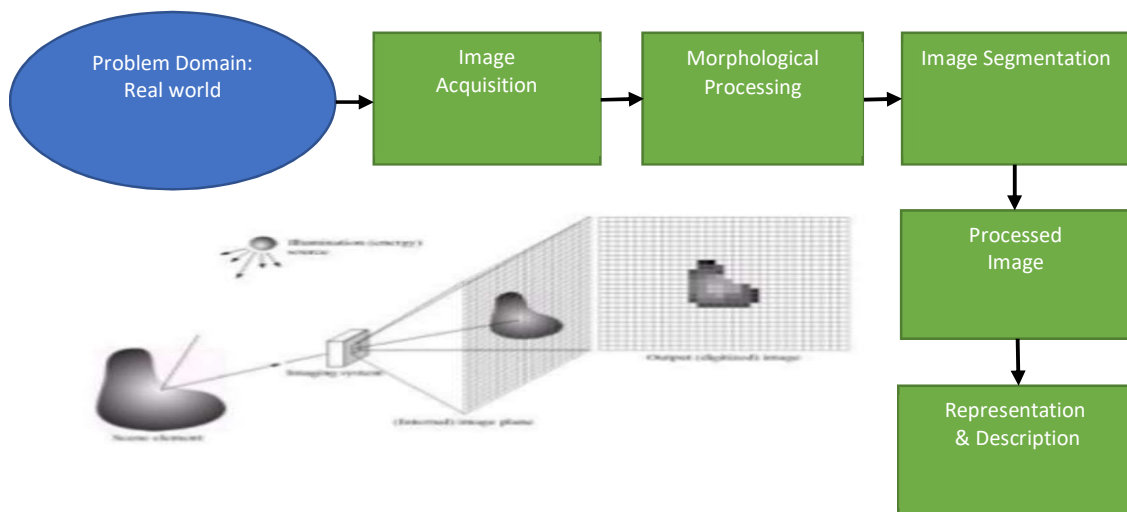


Fig 2. 1: Fundamental steps in image processing [2]

## 2.1 Image

An image is a two dimensional function  $f(x, y)$ , where  $x$  and  $y$  are the spatial (plane) coordinates, and the amplitude of  $f$  at any pair of coordinates  $(x, y)$  is called the intensity of the image at that level [2].

An image is called digital image if  $(x, y)$  and the amplitude values of  $f$  are finite and discrete quantities. A digital image is a discrete signal composed of small squared elementary structures called pixels, each of which has a specific location and value. As much smaller as the pixel is, the higher the quality of image will be. This is because there is more information in the same small space, this is called resolution. The higher resolution can be achieved by gathering more pixels into the width and height of an image [53]. Fig 2.2 shows digital image.

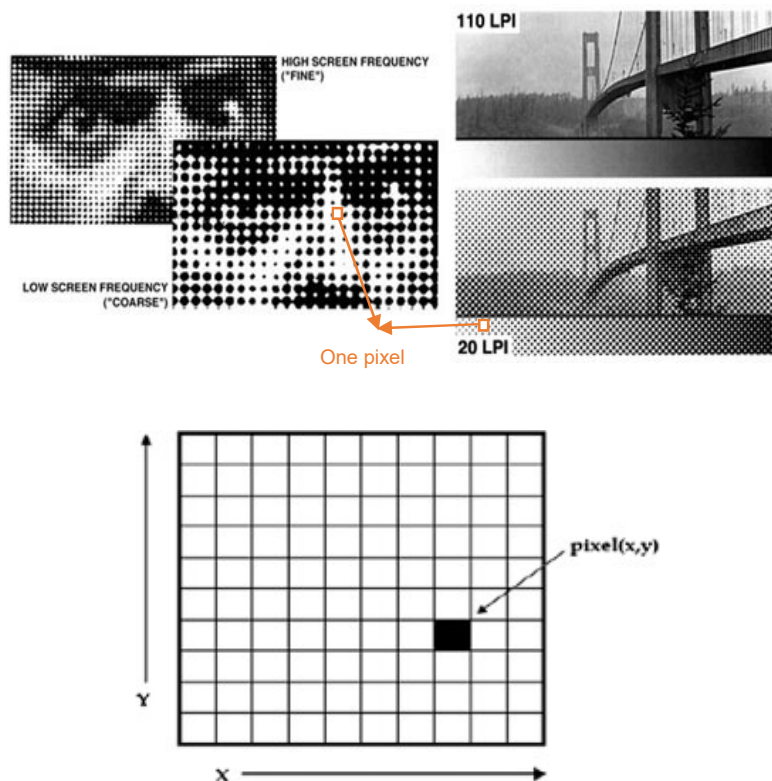


Fig 2. 2: a) Digital image [1], b) pixel  $(x, y)$  [2]

## 2.2 Source of Digital Image

The electromagnetic energy spectrum is the main source of images. The spectral bands are grouped according to energy per photon. It is ranging from the gamma rays to the radio waves. Fig 2.3 illustrates the electromagnetic spectrum.

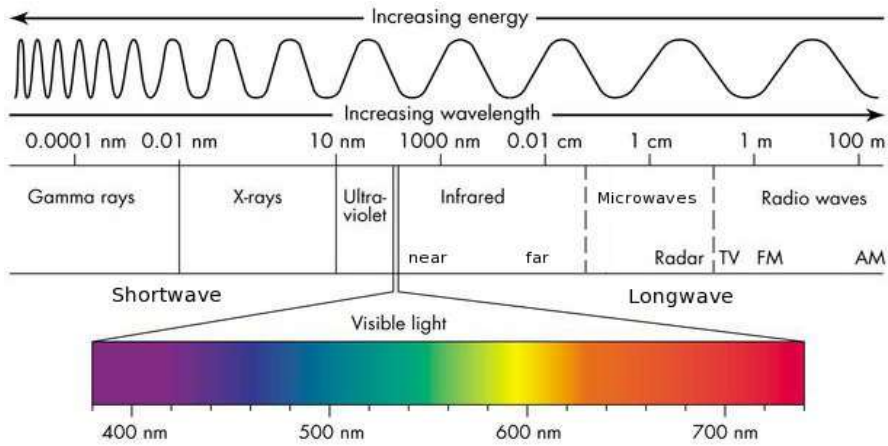


Fig 2. 3: The electromagnetic spectrum. The visible spectrum is shown zoomed to facilitate explanation, but that the visible spectrum is a rather narrow portion of the EM spectrum [2]

### 2.2.1 Gamma Ray Imaging

Gamma ray is the electromagnetic spectrum, that has highest energy and shortest wavelengths among all the spectrum. It has energy range from a few keV to  $\sim 8 \text{ MeV}$  and wavelengths range from 0.0001 nanometer to 0.01 nanometer. Imaging with gamma rays is creating medical diagnostic images using gamma rays emitted by tiny amounts of radionuclides administered to patients, photons of penetrating electromagnetic radiation emitted from an atomic nucleus [3]. This technique permits whole body scans (PET), or more organ and tissue specific scans (SPECT) like bone, brain, heart and lung scan. Fig 2.4 shows gamma ray imaging.

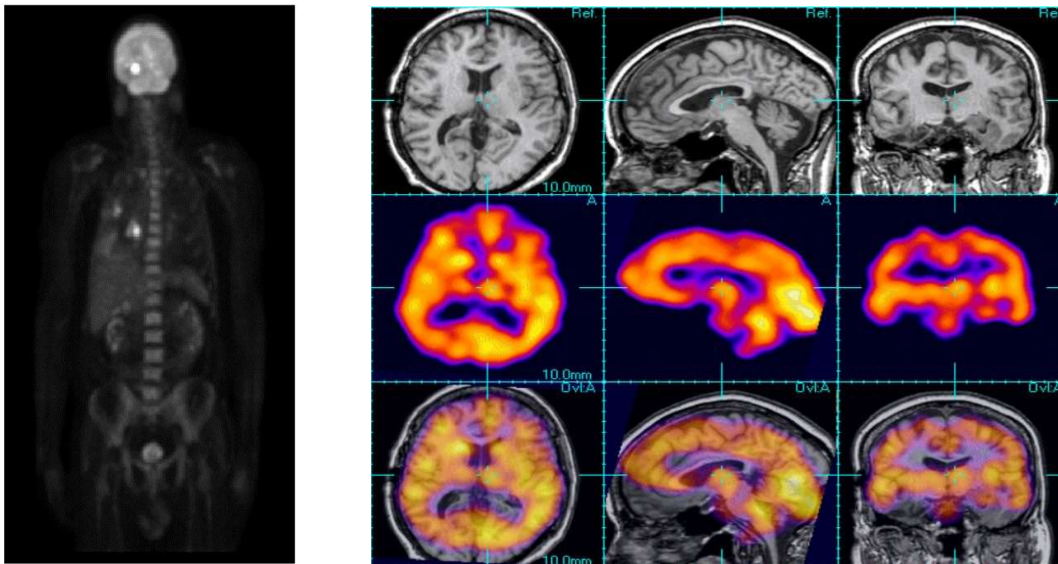


Fig 2. 4: a) Gamma-ray imaging a) in nuclear medicine b) in radioisotope diagnostic [2]

## 2.2.2 X-Ray Imaging

X-rays emit the second highest energy among all of electromagnetic radiation and the energies ranging from 100 eV to 100 keV. X-ray wavelengths are ranging from 0.01 nanometers to 10 nanometers. It is longer than gamma rays and shorter than ultraviolet rays. It has uses in medical diagnostic like medical CT, etc. Fig 2.5 shows different parts of the x-ray spectrum.

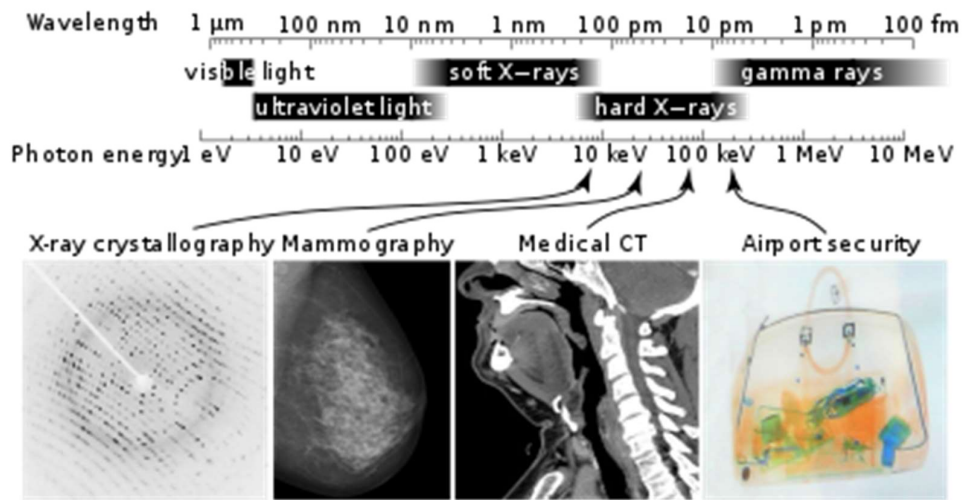


Fig 2. 5: Different parts of the X-ray spectrum [4]

## 2.2.3 Ultraviolet Band Imaging

Ultraviolet is electromagnetic radiation longer wavelength than X-rays and shorter wavelength than that of visible light. It has wavelengths ranging from 10 nanometers to 400 nanometers. Around 10% of the total sunlight is ultraviolet radiation. Ultraviolet light has uses in microscopy, lasers, biological imaging and astronomy. Fig 2.6 shows some examples of ultraviolet imaging.

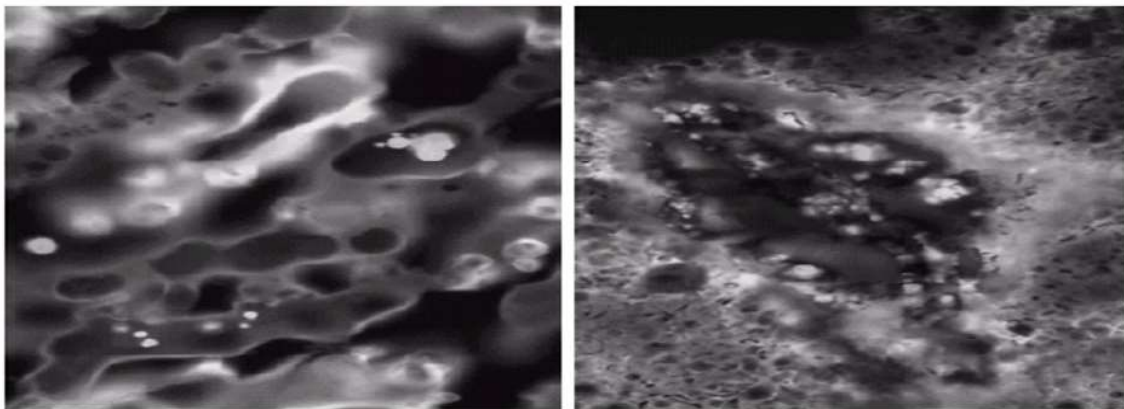


Fig 2. 6: Examples of ultraviolet imaging a) Normal corn, b) Smut corn [2]

## 2.2.4 Visible Light

Visible light is the region of electromagnetic spectrum which is visible to human eyes. It is also called light. Human eyes can respond to the wavelength ranging from around 390 nanometers to 700 nanometers. Apart from the spectrum, human eyes can distinguish unsaturated colors such as pink, or purple variations like magenta. These colors are made from mixture of multiple wavelengths. The Applications of visible light include all the images acquired by our cameras, electron microscope, and monitoring environmental conditions. Fig 2.7 shows examples of visible light image.



Fig 2. 7: Examples of visible light image [2]

### 2.2.4.1 RGB Color Space

RGB color space consist of three components Red, Green and Blue that describes a specific color of a pixel. A non-pure color is a mixture of Red, Green and Blue (RGB). Each pixel of an image has an intensity value of RGB components ranging from 0 to 255. It is imaginable that, 16777216 colors can be produced on the screen by using only these three colors. RGB color space follows the same process as Young-Helmholtz theory of trichromatic color vision [27, 16]. In the 19th century, Thomas Young and Hermann Helmholtz developed this theory. According to the theory, the human retina contains three different receptors ('red, green and blue') that combines the colors to produce the perception of any color [27].

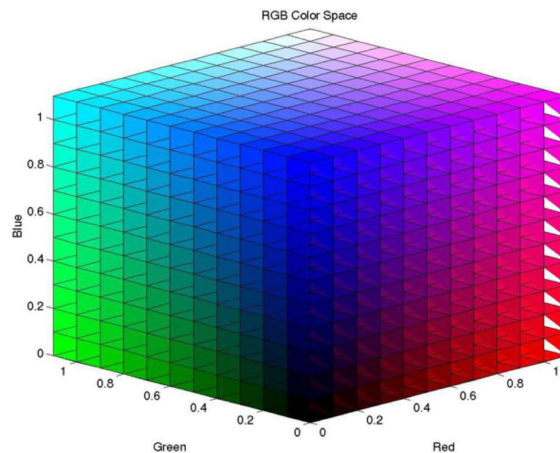


Fig 2. 8: RGB color space (3)

Each pixel is a vector, Figure 2.8 [8]:

Table 2. 1 RGB value for different color

Color	RGB value
Black	[0; 0; 0]
White	[255; 255; 255]
Red	[255; 0; 0]
Green	[0; 255; 0]
Blue	[0; 0; 255]
Magenta	[255; 0; 255]
Pink	[255; 192; 203]
Purple	[160; 32; 240]

It is clearly seen that other colors are the mixture of Red-Green-Blue values. A grey shade can be observed, if all the components of RGB has the same intensity ( $R = G = B$ ). The greyscale is a range of shades of grey without apparent color, where black is darkest possible shade and the lightness is white. The intermediate shades of grey are represented by equal brightness levels of RGB [53]. The binary representation of colors can be described by 8, 12, 16, 18, 24 bits. For example, for a 12-bit digital image there are 4096 possible levels for each primary color.

### 2.2.5 Infrared Band Imaging

Infrared radiation is electromagnetic radiation with shorter wavelengths than microwave and longer than the visible light. It is mostly invisible to the human eye, but human eyes can see infrared light at wavelengths up to 1050 nanometer specially pulsed lasers up to 1050 under certain conditions [1][2][3][4]. Between the range 700 nm to 1 mm, Infrared radiation wavelengths extend from the nominal red edge of the visible spectrum. Most of the thermal radiation emitted by objects near room temperature is infrared [6]. Fig 2.9 shows examples of infrared image.

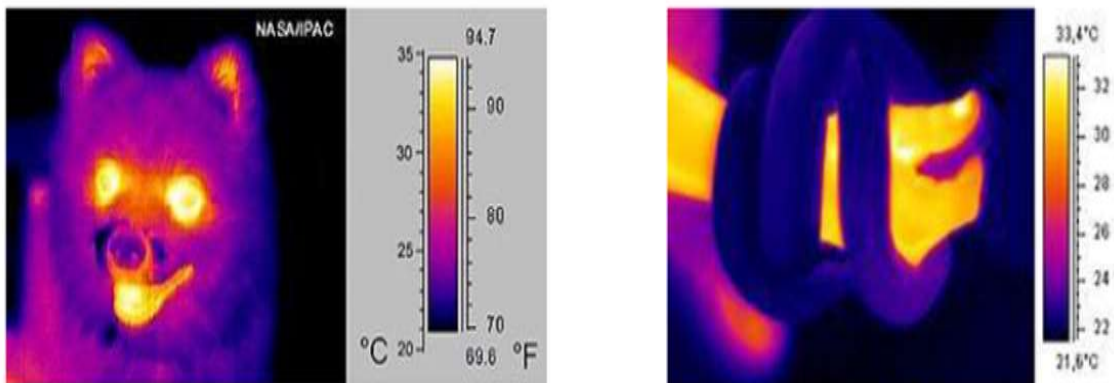
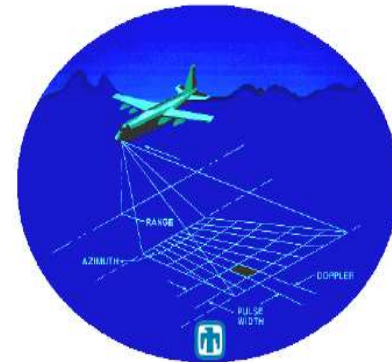


Fig 2. 9: Examples of infrared (“thermal”) image [2]

## 2.2.6 Microwave Band Imaging

Microwave is electromagnetic wave ranging from about 300 MHz to 300 GHz. It is used for detecting or locating and evaluating hidden or embedded objects in a structure. Engineering and application oriented microwave imaging for non-destructive testing is called microwave testing [5]. Some examples of microwave band imaging shows in Fig 2.10.



**Synthetic Aperture Radar System**

Fig 2. 10: Spaceborne radar image of mountains in southeast Tibet. [2]

## 2.2.7 Radio Band Imaging

Radio wave is the electromagnetic spectrum, that has lowest energy and longest wavelengths among all the spectrum. It is ranging from 20 kHz to around 300 GHz, roughly between the upper limit of audio frequencies and the lower limit of infrared frequencies [7]. The radio waves use in Magnetic Resonance Imaging- MRI to generate images of the human body. MRI images of a human shows in Fig 2.11.



a b

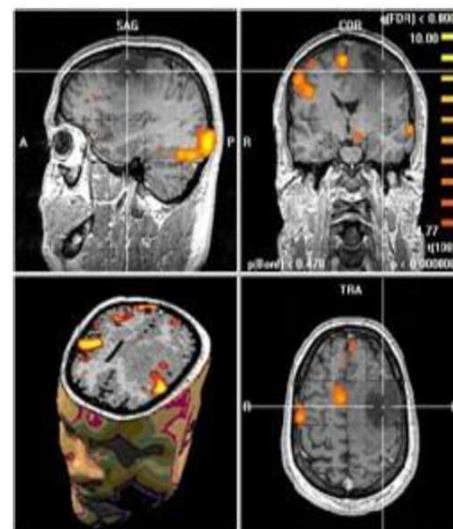


Fig 2. 11: MRI images of a human a) knee, b) spine, and c) brain [2]

## 2.2.8 Ultrasound Imaging

Ultrasound is a cyclic sound pressure wave with frequencies larger than human hearing level [8]. It has same physical properties as audible sound, but human cannot hear it. The operational frequencies of ultrasound devices (Fig 2.12 a) are ranging from 20 kHz up to several gigahertz. Sonography to produce pictures of fetuses in the human womb (Fig 2.12 b) is the renowned application of ultrasound.

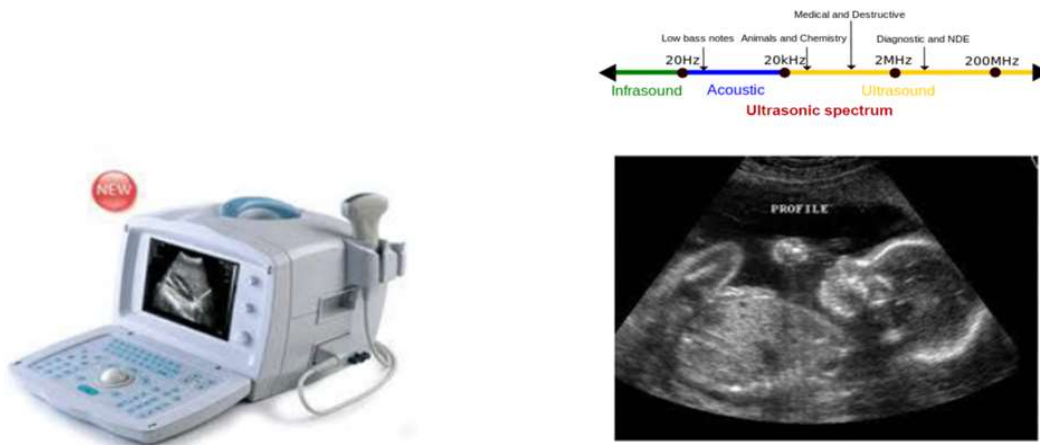


Fig 2. 12: a) Ultrasound image acquisition device, b) Ultrasound Baby image during pregnancy [2]

## 2.3 Morphological Image Processing

Morphological image processing is a technique for the analysis and processing of geometrical structures, based on Minkowski set theory, theory of finite lattices, topology, and random functions. It is a gathering of non-linear operations related to the shape or morphology of features in an image. Morphological operations mainly suited for binary images, as it relies on the relative ordering of pixel values not on their numeric values. The main application of Morphological operations is image enhancement, image restoration, edge detection, texture analysis, feature generation, shape analysis, component analysis, feature detection, and noise reduction.

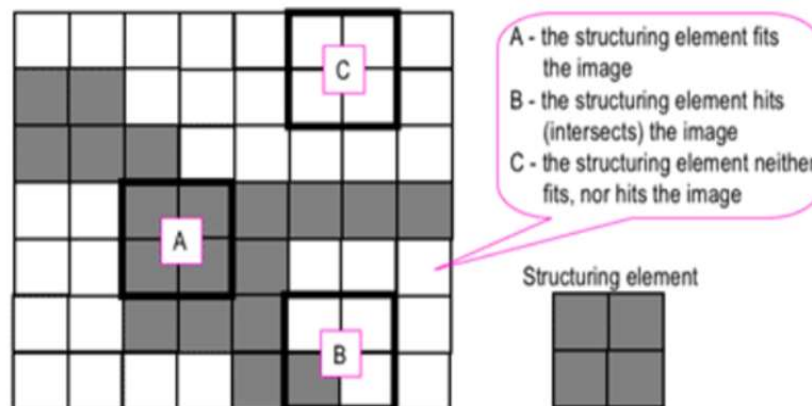


Fig 2. 13: Probing of an image with a structuring element (white pixel has zero value and grey pixel has non-zero value) (11)

A small image or template called structuring element (SE) (Fig 2.13) used for probing in morphological operation. It is being check whether the structural element fits within the neighborhood of pixels by placing it at all possible locations in the image and comparing with the corresponding pixels. Morphological technique creates a new binary image where pixel value is zero if test is unsuccessful at that location of input image. On the other hand, pixel value is nonzero if the test is successful.

## 2.3.1 Fundamental Morphological Operations

### 2.3.1.1 Dilation

Dilation is a mathematical morphological operation that typically applied to binary images. However, it is applied also to grayscale images. Dilation convert every background pixel that touching an object pixel into object pixel. It is gradually enlarging the boundaries of foreground pixels [18]. As a result, undesired holes within the regions become smaller, objects become larger, and merge multiple objects into one. In Dilation operation, structural element or kernel passes through pixel by pixel of input image and improve the shapes, adding new pixels in the neighboring regions [18,22]. Fig 2.14 shows examples of dilation operation.

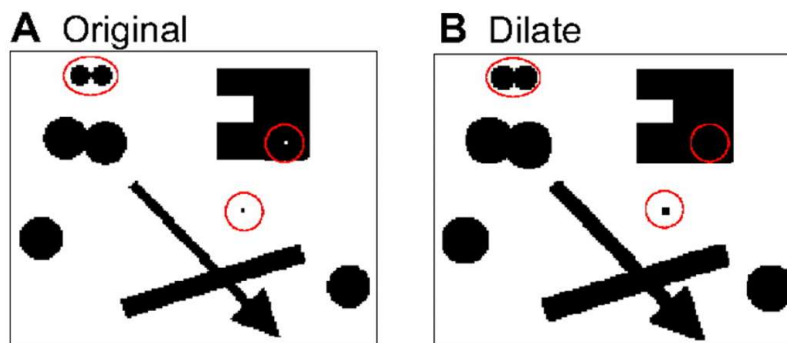


Fig 2. 14: examples dilation operation <sup>(12)</sup> a) original image, b) Dilated image

Here, input image is  $\bar{I}$  and SE is  $Z$ . After dilation technique applied, that produces new binary image,  $g = \bar{I} \oplus Z$ . Where,  $g(x, y) = 1$  for all location  $(x, y)$  that hits SE  $Z$ . Elsewhere,  $g(x, y) = 0$ .

### 2.3.1.2 Erosion

As like dilation operation, erosion operation needs input image which is to be eroded and a structuring element consist of a matrix of zeros and ones. Structuring elements are much smaller than the input image. Erosion operation convert every object pixel that touching a background pixel into background pixel. It makes objects smaller and splits a single object into multiple objects [17]. In Erosion operation, small scale details is removed from a binary image. As the same time, it reduces the size of region of interest (ROI). Fig 2.15 shows examples of erosion operation.

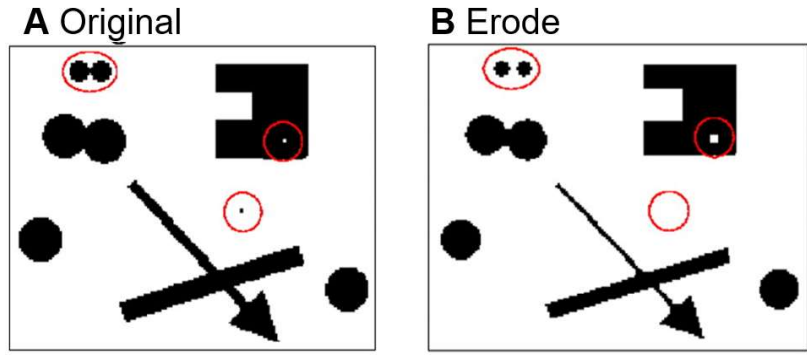


Fig 2. 15: examples erosion operation <sup>(12)</sup> a) original image, b) Eroded image

Here, input image is  $\bar{I}$  and SE is  $Z$ . After erosion technique applied, that produces new binary image,  $g = \bar{I} \ominus Z$ . Where,  $g(x, y) = 1$  for all location  $(x, y)$  that fits SE  $Z$ . Elsewhere,  $g(x, y) = 0$ .

## 2.4 Image Segmentation

Image Segmentation is a widely used image processing technique that is used for partition an image into meaningful parts having similar properties and features. This is the first step of image analysis for shapes and objects detection. Image segmentation is principally two types, local segmentation and global segmentation [19]. Local segmentation concerned with specific region of image, where as global segmentation concerned with the whole image. There are several ways to perform image segmentation which includes thresholding method, edge-based method, region-based method, clustering based method, watershed-based method, PDE based method and ANN based method. Thresholding, edge-based and region-based methods are widely used segmentation method. Thresholding is the simplest method which is based on the histogram peaks of the image to find particular threshold values. The edge-based segmentation based on discontinuity detection that uses edge filter for characterizing pixels in the edge. In region-based segmentation image is partitioned into homogeneous regions by grouping the neighbor's pixels which have the similar pixel value [42, 43].

# Chapter 3

## Medical Imaging

Modern medical technology is capable to diagnose and treat patients without any harmful side effects. Medical imaging is one of the techniques that allows diagnose the body without the surgery or other invasive procedures. It helps to create visual representations of the interior of a body and of the function of some organs or tissues. it can also be used to establish a database of a normal anatomy and physiology in order to identify abnormality. Different medical imaging technique are used for acquiring the different structures inside of the human body.

The journey of medical imaging began much earlier, when Wilhelm Röntgen discovered the X-ray [9]. Radiography was the first medical imaging technique. In 1946 nuclear medicine imaging tool was used to make cocktail of radioactive iodine for curing a patient with thyroid cancer [44]. Nuclear medicine includes PET (positron emission tomography) and SPECT (single photon emission computed tomography). Although, it was capable to acquire accurate and detailed image, it was very expensive. Sir Godfrey Hounsfield invented the first commercially viable computed tomography (CT) scanner in 1972 [45]. 3D volume of the inside of the object can create using Digital geometry processing of a large series of 2D radiographic images of CT. During 80s, magnetic resonance imaging (MRI) technique used in radiology to form pictures of the anatomy and the physiological processes of the body in both health and disease. It was a good but each MRI machines cost millions of euros. On the other hand, ultrasound was cheaper technique of diagnostic imaging based on the principal of the sonar. It sends high-frequency sound waves into the body by passing the organs and the returning waves vibrate the transducer turning the vibrations into electrical pulses which are sent to the ultrasonic scanner where they are converted into an image. Ultrasound has no adverse bio-effects, as a result it has become a very popular imaging technique [44].

This chapter describes the different type of medical imaging used in this study: computed tomography (CT) and ultrasound imaging. In addition, it describes the file format used to store the information of medical imaging. It also describes the Surgical navigation procedure which uses these two kinds of technology.

### 3.1 Computed tomography (CT) scan

The word Tomography comes from the Greek words Tomos and Graphein which means slice imaging and Computed is associated to the algorithms used to reconstruct that slice. So, the entire meaning of Computed Tomography (CT) become 'slice imaging reconstructed by the algorithm'. British engineer sir Godfrey Hounsfield invented computed tomography (CT) in 1972 based on the theoretical work of

Allan Cormack [48][49], who introduced computed axial transverse scanning [46, 47]. CT was a very importance invention in medicine, sir Godfrey Hounsfield received the Nobel prize and the Knighthood title for his great invention. This invention helped to overcome the limitations of X-ray, which was the well-known medical imaging modality for the last 100 years. X-ray maps a 3D volume object into a 2D image, that causes highly reduction in image contrast and difficulty in imaging soft tissues. Moreover, quantitative data is missing in standard film-based technology. CT scan maps a scanned volume into a 3D platform that create exact perception of real object. CT scan (Fig 3.1) is widely used in modern diagnoses and treatment.

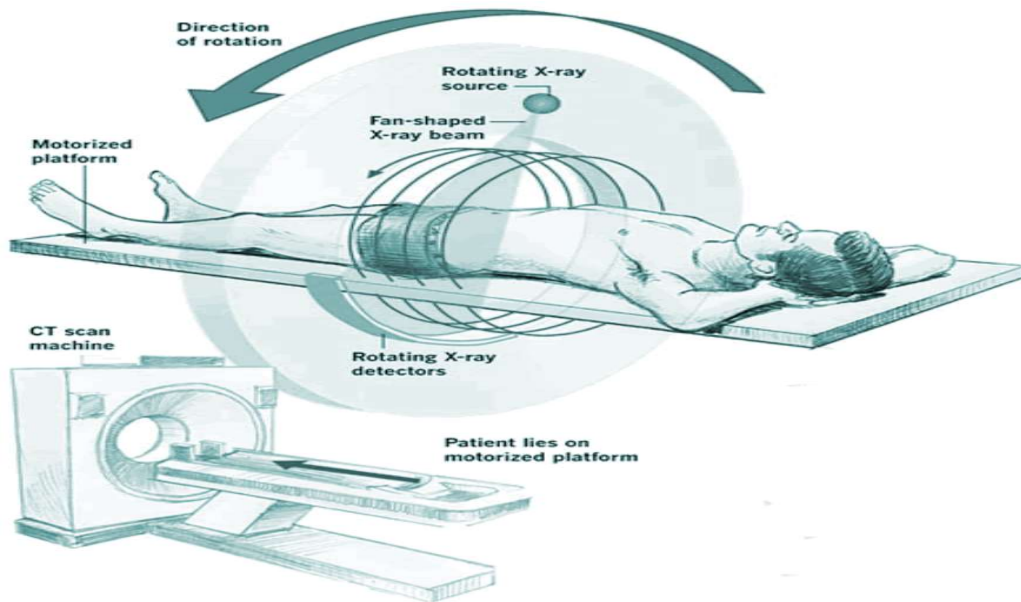


Fig 3. 1: CT scanner <sup>(4)</sup>

The basic principle of CT scan is same as X-ray. X-ray uses a fixed X-ray tube where as CT scanner is a motorized x-ray source that rotates around the circular shape like a donut called gantry. During the CT scan, a series of X-ray detectors and a tube rotate synchronously around the patient lies on a bed and the x-ray tube shooting narrow beams of x-rays through the body. X-ray detectors are located opposite of x-ray tube, which measures how much the respective incoming X-ray passing through the tissues inside the human body were attenuated by its internal materials at a specific angular orientation. As x-ray passes through the tissues inside the human body produces shadow with different intensities that penetrates into matter called attenuation. CT scanners makes a lot of attenuation detailed the plane of the thickness cross section of the body and transmit this data to a computer for reconstruct a digital image of the cross section. Fig 3.2 illustrates the functional flowchart of CT scanner.

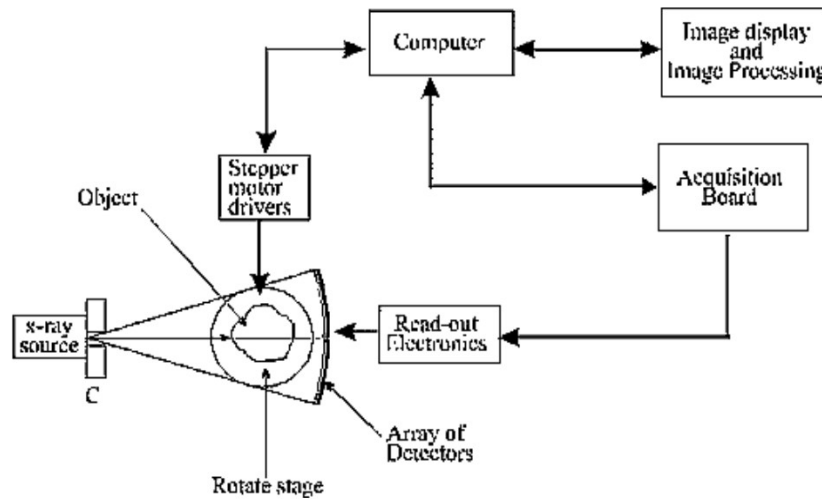


Fig 3. 2: Functional flowchart of CT scanner <sup>(4)</sup>

During one full rotation of x-ray source, CT computer takes different views around the patient body. A gray-scale image reveals the different densities of the interior of the human body. By overlapping all the views CT computer construct a single two-dimensional image slice of the patient. A better image representation of the interior of the human body is achieved by Increasing the number of views around the patient. Therefore, a three-dimensional image or slice is constructed (Fig 3.3) from a two-dimensional image using the beam width. Beam width represents the thickness in image. The thickness of the tissue ranging from 1mm to 10mm. The motorized bed is moved forward incrementally towards the gantry after completing rotation of full slice. This process is being repeated until the desired number of image slices is collected. Fig 3.4 shows slice reconstruction by overlapping all the views at 22.5-degree and 45-degree step over the object.

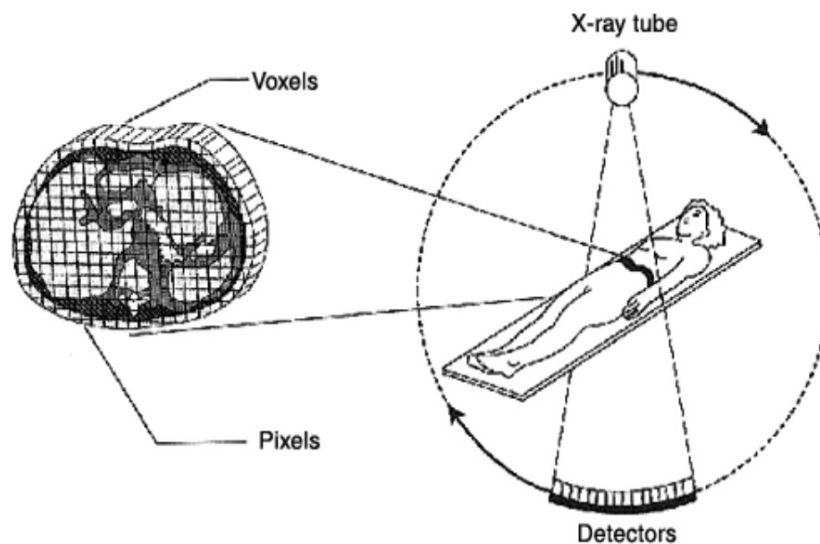


Fig 3. 3: Volume construction in CT scanner <sup>(4)</sup>

The attenuation measurement follows the Beer's law [51],

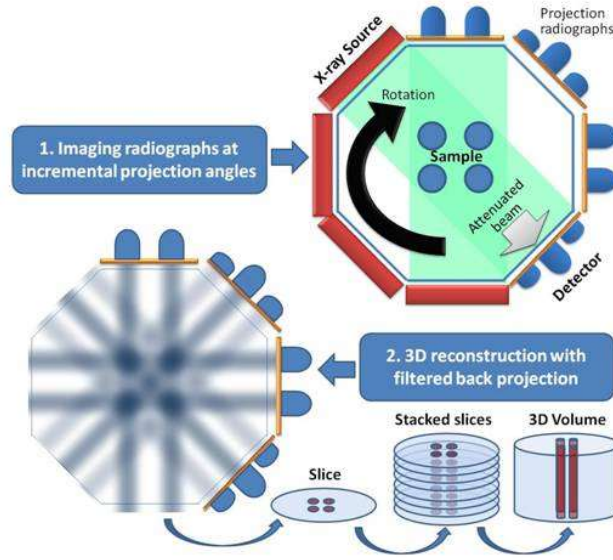


Fig 3. 4: slice reconstruction by overlapping all the views at 22.5-degree and 45-degree step over the object, and 3d representation of the slice <sup>(6)</sup>

and expresses as, where X-rays attenuation projection are shows in Fig 3.5,

$$I = I_0 * e^{-\mu\Delta x} \quad (3.1)$$

$$I = I_0 * e^{-(\mu_1 + \mu_2 + \mu_3)\Delta x} \text{ whereas, } \mu_i = \mu_i X_{v,i} \quad (3.2)$$

$I_0$ : intensity of incident x – ray

$I$ : intensity of attenuated x – ray

$\mu$ : linear attenuation coefficient

$\Delta x$ : thickness of object

$X_v$ : volume fraction

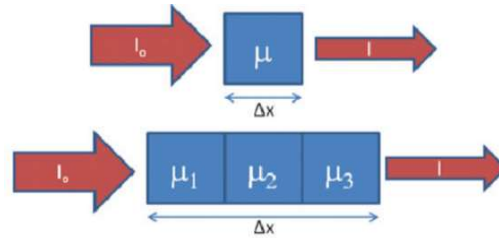


Fig 3. 5 : X-rays attenuation projection <sup>(5)</sup>

$$p = -\ln \frac{I}{I_0} = \int \mu(x) dx \quad (3.3)$$

where  $p$  is the output value from each detector. The integrals of the attenuated coefficients are evaluated for each view. As the different views used to reconstruct slice, that also reconstructs these attenuation coefficients. Godfrey Hounsfield invent a scale for measuring the radiodensity by normalizing these attenuation coefficients in relation to the water attenuation coefficient of the water. It is an important measurement in CT diagnosis exams. Where the units are the tissue density.

$$HU = \frac{\mu - \mu_{water}}{\mu_{water} - \mu_{air}} * 1000 \quad (3.4)$$

Here,  $\mu_{air}$  and  $\mu_{water}$  are the attenuation coefficient of air and water air respectively. The HU values of 0 and -1000 for water and air respectively. Typically, CT scanners are calibrated for these two values (Brooks and Chiro 1976). The lower HU value, the darker is the shade. The air is black, and the soft tissues are represented by a greyscale color. The meaning of these values is important to understand the anatomy and the tissues inside the human body.

Table 3. 1 : HU Values

HU values	
Air	-1000
Lung	-900 to -500
Fat	-200 to 50
Water	0
Intestine	5 to 35
Kidney	20 to 40
Heart and Tumor	20 to 50
Pancreas	30 to 50
Muscle	40 to 50
Blood	50 to 60
Liver	60 to 70
Thyroid	60 to 80
Spongy Bone	50 to 250
Bone	250 to 3000

It is clearly seen at table that different organs have different range of HU values. The reason why HU is not fixed value, but range is mainly because the attenuation coefficients are dependent of the incident beam energy. Moreover, CT scanner calibration, patient age, sex and small fluctuations from patient to patient tissue densities are responsible for not having a fixed value of HU for each organ. Form the table, it is also seen that the HU ranges from -1000 to 3000. For this reason, a 12-bit value per voxel is usually used ranging from -1024 HU to +3071 HU. The 12-bit integer unsigned format is a better compression representation because CT scanners output values ranging between 0 to 4095 for the CT data. The CT scanner manufactures encode two additional tag constants called *RescaleSlope* and *RescaleIntercept* in the output image, due to convert the output CT data value for each voxel and the HU. These tags are just the parameters of the linear function which relates the input CT scanner values [0 4095] to the output HU values [-1024 3071]. Equation 2.4 presents this relationship. *RescaleSlope* and *RescaleIntercept* have common values respectively 1 and -1024.

$$HU = RescaleIntercept + VoxelValue * RescaleSlope \quad (3.5)$$

### 3.2 CT Image acquisition

As seen before, CT scan point x-ray source to a particular area on the patient body, where as digital detectors are located opposite to the x-ray source. X-ray source emits electromagnetic radiation to the patient body. Then, the radiation passes through the body and reaches to the detectors. Therefore, detectors upload the image to the computer. Sensitivity, efficiency, linearity, energy resolution and dead time are the main characteristics of the detectors. These features help to get accurate image which is error free and smooth. Detectors are two types, scintillation detectors and detector filled with gas. Scintillation detectors are most common, and it uses materials such as sodium iodide, bismuth germanium oxide, cesium iodide and cadmium tungstate. The detectors mainly measure the transmission of a thin beam ranging from 1mm to 10 mm of the cross-section image is taken from different angles and measure the depth in the third dimension [43,44]. It does not produce directly the image. CT scanner produce image using the measurement provided by detectors.

### 3.3 Ultrasound Imaging

Ultrasound (US) imaging is a medical tool that produces image on the reflection of the waves of the body structures for helping a physician to evaluate, diagnose and treat medical conditions. The basis physics of ultrasound was studied for the first time by physiologist Lazzaro Spallanzani in 1794 [53]. The next improvements of ultrasound device were done in 1877 [53], when Jacques and Pierre Currie discovered piezoelectricity. It was very important discovery for ultrasound. Piezoelectric effect used for emitting and receiving sound waves by ultrasound probes or transducers. Next eighty years ultrasound went through several stages of development. Later in 1956, iconic black and white ultrasound images are in use for clinical purpose. Obstetrician Ian Donald and engineer Tom Brown developed first prototype system for ultrasound in Glasgow [11]. Therefore, ultrasound became widely used in American hospitals during 1970s. In 1980s, first three-dimensional ultrasound technology invented by Kazunori Baba from the University of Tokyo. 1986 is the year when first three-dimensional image of fetus was taken by ultrasound. Ultrasound adopted four-dimensional capabilities during 1990s, where ultrasound guided biopsies started to surface [11].

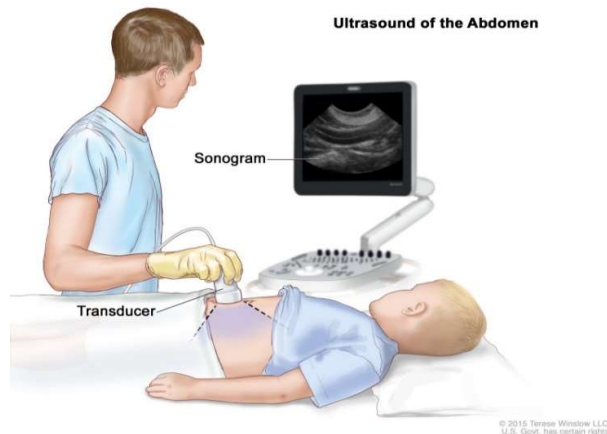


Fig 3. 6: Abdominal ultrasonography <sup>(9)</sup>

Ultrasound sound use sound waves to create image. Sound waves can be quantified by their wavelength, frequency and velocity. Where, sound waves have inverse relationship between frequency and wavelength. The higher the frequency causes shorter the wavelength. Higher frequency ultrasound creates high resolution images but unable to penetrated deeper tissue due to their short wavelength. On the other hand, the scenario is opposite for lower frequency. So, the frequency-wavelength relationship is considered before selecting an appropriate transducer. The ultrasound machine transmits high frequency sound waves usually ranging from 2 to 12 MHz [13] into the body using a transducer or probe. This sound waves travel into the body and hit boundary between fluid and soft tissue or soft tissue and bone. Where, some sound get reflected and go back to probe, and some sound waves travel further until they reach to other boundary and get reflected. Reflected sound waves are received by the probe and transmitted to the machine. Therefore, ultrasound machine calculates the distance from the probe to the bone or tissue or organ boundaries using the speed of sound in tissue and the time of each echo returns. Lastly, 2D image is formed using the distances and intensities of the echoes [12]. Fig 3.6 shows an example of ultrasonography.

Table 3. 2: Sound wave velocity

Sound wave velocity	
Air	331 m/s
Tissue	1540 m/s
Bone	4080 m/s

### 3.4 Ultrasound Imaging acquisition

The ultrasound is generated and launch by electrical excitation from ceramic crystals in piezoelectric transducer. An electric signal applied to the crystal, that causes vibration and deformation in crystal. Ultrasound beam generated from this vibration. Therefore, ultrasound beam produces discontinuous pluses for emitting and receiving electrical signal. Firstly, transducer emits pluses and then receives reflected ultrasound waves. Reflected sound waves deform again the crystal in transducer and produce electric signal that is then converted into an image. Transducer typically spend 1% of the time for emitting ultrasound waves, rest of the time it only receives waves. Basic ultrasound imaging system is shown below, Fig 3.7,

an amplitude modulated sinusoid:  $p(t) = a(t)e^{-i\omega_0 t}$  where  $\omega_0 = 2\pi f_0$

distance = velocity  $\times$  time

$z$ : distance

$c$ : sound velocity in the body

transducer causes a pulse at time:  $t = 2z$

depth:  $z = \frac{ct}{2}$

wavelength:  $\lambda = \frac{c}{f_0}$

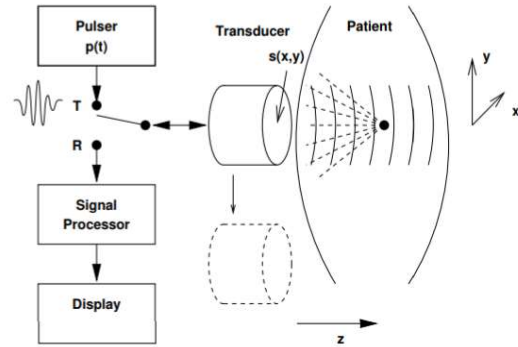


Fig 3. 7 : Ultrasound imaging system <sup>(10)</sup>

### 3.5 DICOM Image Format

Digital Imaging and Communications in Medicine (DICOM) is most commonly used for transmitting, storing, retrieving, printing, processing, and displaying medical imaging information [14]. Earlier, before 1980s, it was very difficult for computer tomography devices manufacturers to integrate distribution systems that use a range of hardware and software platforms. Moreover, image information was highly complex and unstructured. To deal with this problem, in 1983, the American college of radiology (ACR) and the National electrical manufacturers association (NEMA) join forces formed a standardized image format DICOM [15]. DICOM includes workflow and data management, protocols for image exchange, image compression. Visualization, image presentation, and results reporting [16].

# Chapter 4

## Acquiring a 3d Model

The importance of 3d modeling in medical diagnosis have grown significantly. Acquiring a 3D model prior to the surgery is very essential for reducing the risk of surgery. It allows the surgeon to better plan the surgery intervention by knowing in advance the exact anatomical structures. As a result, surgeons are capable to provide highly accurate diagnosis. That helps them to determine the best treatment [27]. There are three main medical imaging approaches are widely used for acquiring 3d model representation of the bone. CT, MRI and ultrasound imaging.

In this chapter, CT and ultrasound imaging of pig vertebra are used for reconstructing 3d model of a pig column phantom. The column was placed inside a box, emerged in a gel, as shown in Fig 4.1.



Fig 4. 1: Phantom column [28]

### 4.1 Volume Reconstruction from CT Scan

The 3d reconstruction of the pig column was made using 3D slicer open-source software ([www.slicer.org](http://www.slicer.org)). The CT images were taken at the Hospital Santa Maria in Lisbon [28]. CT imaging modality is most suitable for bone detection. It enhances the compact bone contrast, since the HU intensity values of bone is higher in relation to the other soft tissues. CT based on the X-ray absorption by different fabrics, such as conventional X-ray, but it allows to obtain cross-sectional images - slices. The CT images are formed by a set of pixels distributed in rows and columns forming a matrix. The images obtained from the CT performed phantom having a matrix of  $512 \times 512$  pixels (Fig 4.3 (a)). A total of 304 images acquired, which forms a volume of  $512 \times 512 \times 304$  voxels. It is possible to calculate the spacing between pixels is 0.4883mm, and the spacing between rows and columns slices is 1.5 mm by knowing voxel for milliliter:  $(250 = 512 \cdot 0.4883)$  mm  $\times$   $(250 = 512 \cdot 0.4883)$  mm  $\times$   $(456 = 304 \cdot 1.5)$  mm. In addition, thickness of each vertebrae is calculated using the slice thickness.

Table 4. 1: All vertebrae dimension and frame location

Vertebrae no	Start (mm)	End (mm)	No. frame	Thickness (mm)
1	-416.225	-378.225	38	$38 \times 1.5 = 57$
2	-376.725	-340.725	25	$25 \times 1.5 = 37.5$
3	-339.225	-303.225	25	$25 \times 1.5 = 37.5$
4	-301.725	-267.225	24	$24 \times 1.5 = 36$
5	-265.725	-231.225	24	$24 \times 1.5 = 36$
6	-229.725	-196.725	23	$23 \times 1.5 = 34.5$
7	-195.225	-160.725	23	$23 \times 1.5 = 34.5$

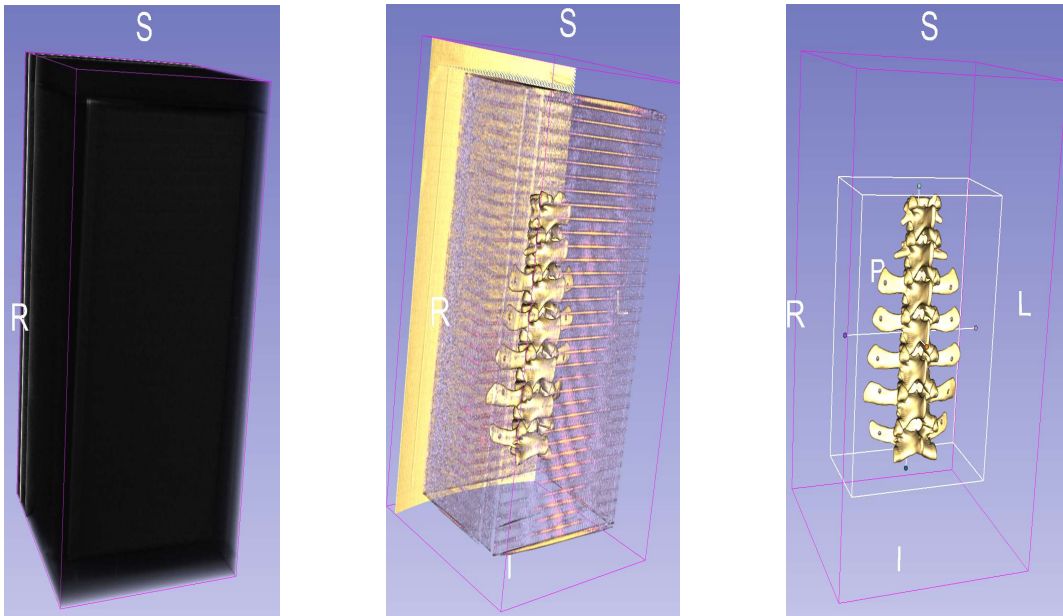


Fig 4. 2: Reconstructed Volume: a) 3D grid or volume is obtained by stacking all the slices together, b) the same volume using a different colormap for better visualization the vertebrae anatomy. C) cropped vertebrae

## 4.2 Cropping CT

The volume reconstruction module evaluates a volume directly from a CT scan (Fig 4.3). However, it is mandatory to crop region of interest (ROI) or vertebrae, before performing automatic segmentation. Volume cropping is performed for extracting from the main volume the sub-volumes containing only the vertebrae (Fig 4.3(b)). In order to achieve this, a crop volume module of 3d slicer was applied. In detail, the module was used to find the bounding boxes containing the vertebrae. The main idea behind this module is to set the bounding box along the Left axis (Fig 4.3(a)), the bounding box along the Superior axis (Fig 4.3(b)), and the bounding box along the Posterior axis (Fig 4.3(d)).

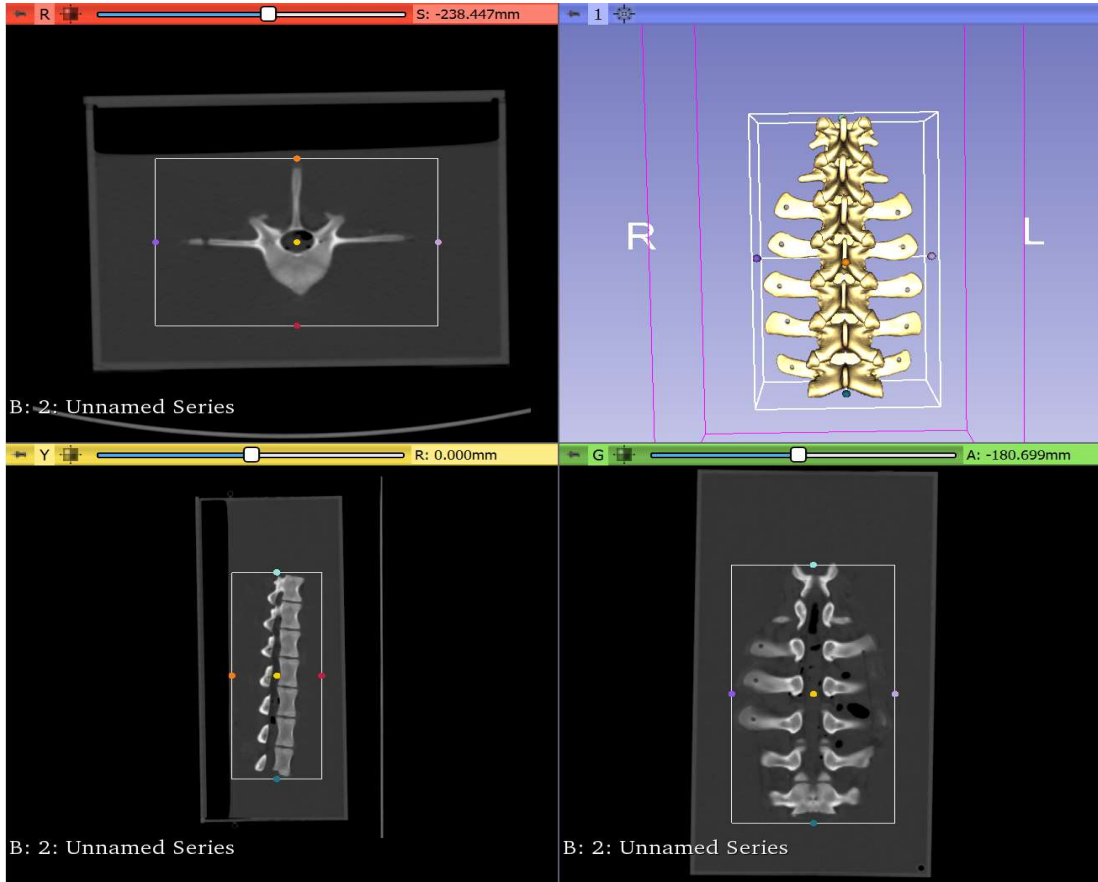


Fig 4. 3: a) Top left: red screen shows Left axis, b) Bottom left: yellow screen shows Superior axis, c) Top right: 3d view, and d) Bottom right: green screen shows Posterior axis

### 4.3 Segmentation CT

Today's doctors are using imaging technology to observe in detail the patient's internal structures, such as bones. A stack of cross-sectional CT images of vertebrae was taken and analyzed image by image until a diagnosis is performed or a vertebral 3D reconstruction of the structure is made. However, it requires a high level of expertise. Bone segmentation provides a realistic 3D representation of those structures in which the clinician could easily and quickly inspect its diseases, perform a diagnosis or preoperatively planning a surgery.

Image segmentation technique can be express by the equations below:

$$I(x) \in R \quad (4.1)$$

$$x \in Z \quad (4.2)$$

where an image  $I$  can be defined over its domain  $Z$ , which is an  $N$ -dimensional grid. A specific intensity value for each grid point is taken for the  $N$ -dimensional Image function  $I$ . Where, the grid points are the pixels of a 2D image and voxels of a 3D image. The simplest and widely used image segmentation method is threshold segmentation [25,29]. Here, in this study, the segmentations module of 3D slicer was applied for obtaining threshold based automated 3D segmentation from a CT.

### 4.3.1 Threshold based segmentation

A simple threshold segmentation was performed based on the HU intensity values of the volume voxels. The value of the threshold changes for capturing demanding features along each direction, which depends on the direction where the bounding box is to be constricted. All pixels with HU intensity values between the range become one, defining the object pixels, and all the pixels out of the threshold range become zero, defining the background pixels. The threshold segmentation method was proposed due to the fact that the bone presents the high HU intensity value almost throughout its geometry. Fig 4.4 shows the yellow region, the result of the segmentation using a HU intensity value ranging from 265 to 1300 as threshold. A high HU intensity threshold to capture the main geometry of the vertebral bones while disregarding the low intensities present in the joint regions. this way, a volume of vertebrae is obtained.

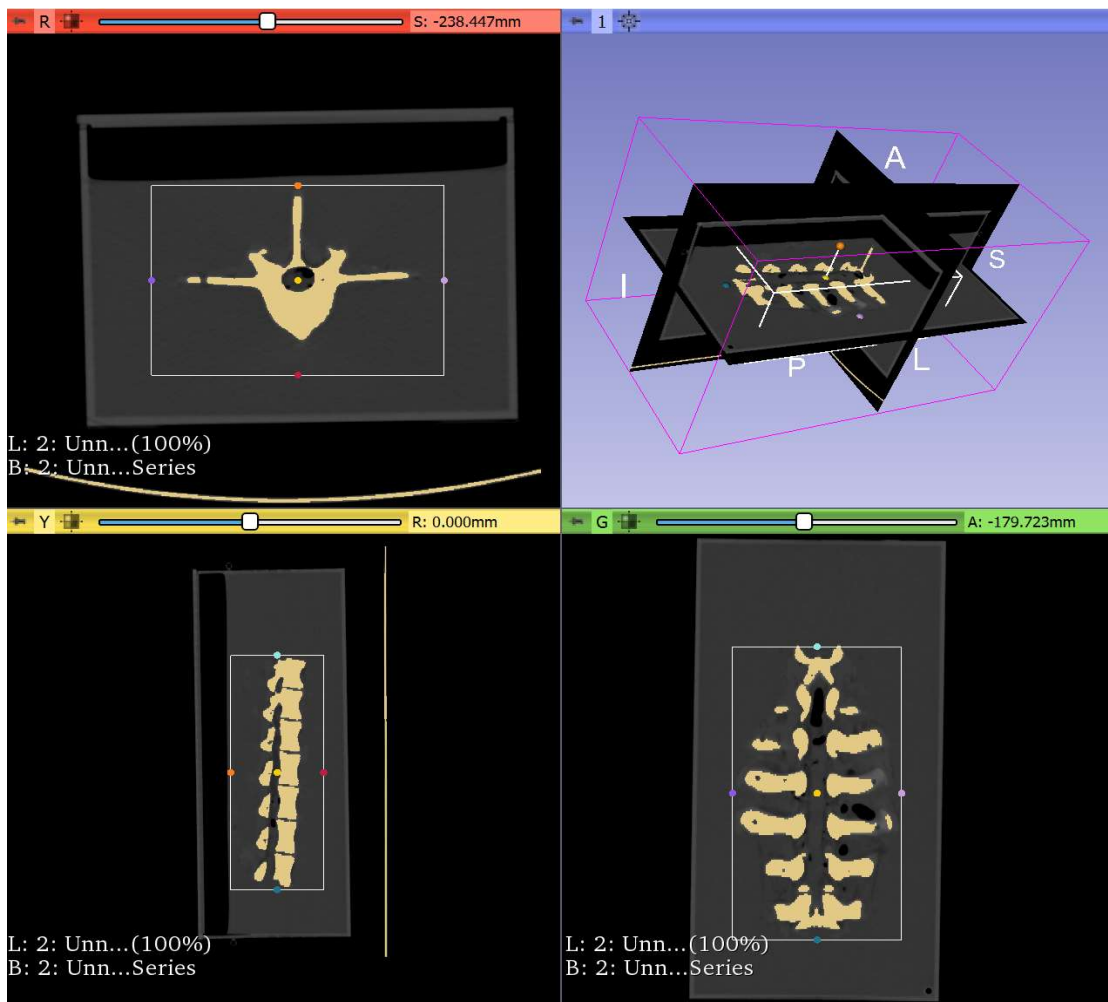


Fig 4. 4: Segmented vertebra: a) Top left: shows Left axis, b) Bottom left: yellow screen shows Superior axis, c) Top right: 3d view, and d) Bottom right: green screen shows Posterior axis

Finally, a 3d model of vertebrae was reconstructed using MakeModelEffect operator of the editor module in 3d slicer. It shows in the Fig 4.5.

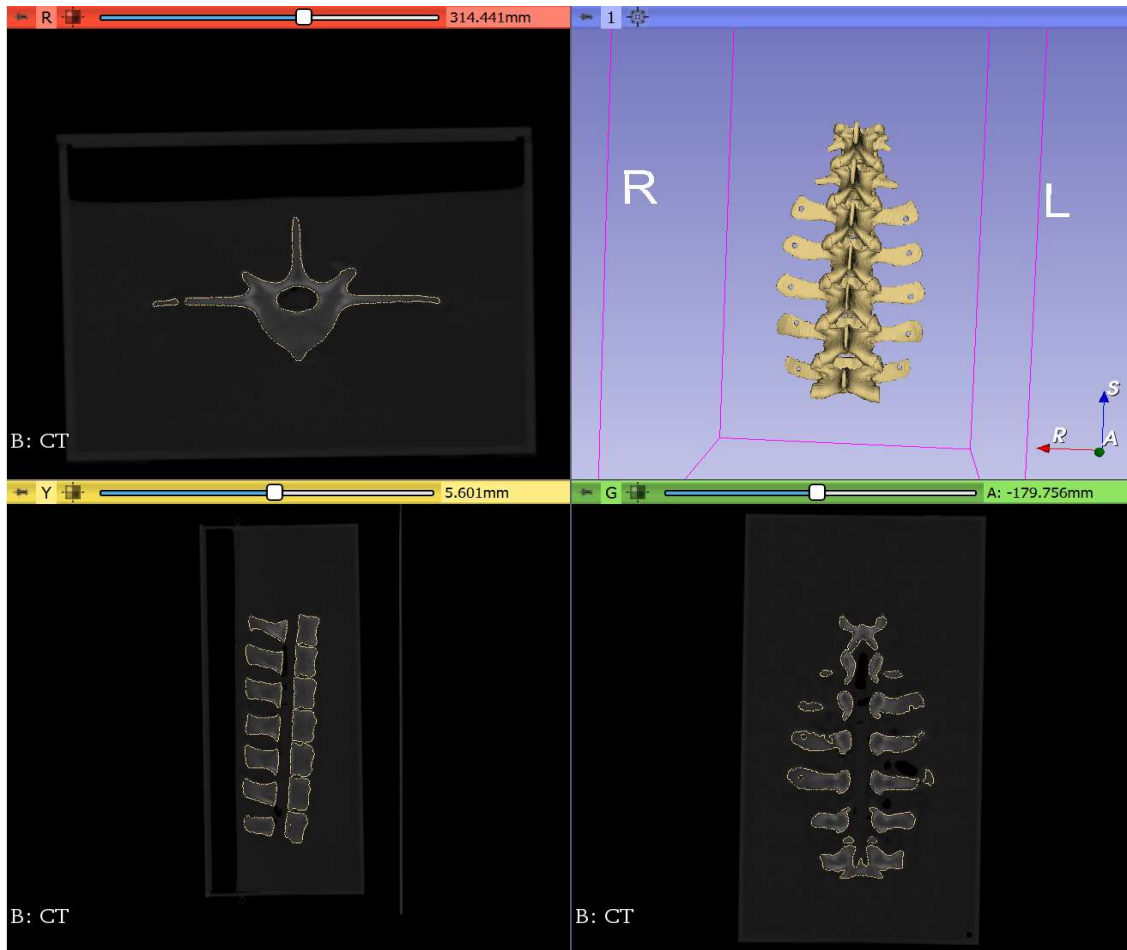


Fig 4. 5: 3d reconstructed model: a) Top left: red screen shows Left axis, b) Bottom left: yellow screen shows Superior axis, c) Top right: 3d view, and d) Bottom right: green screen shows Posterior axis

#### 4.4 3D Model Reconstruction from Ultrasound Imaging

Ultrasound imaging is the most important medical imaging technique that allows capturing images in real time [26]. It shows movement of the internal organs of human body as well as blood flow. Doctors could easily inspect diseases and perform a diagnosis in real time. Ultrasound imaging uses high frequency sound that travel through the different types of tissue in the body. However, it is reflected by the bone. As a result, in the bone inspection, 3d model created using ultrasound is the inverse image of the bone structure. Here, in this thesis, a 3d vertebrae model was reconstructed using 3D slicer.



Fig 4. 6: (a) echograph used to acquire the images of US-linear probe and coupled to an instrument Spectra Polaris system. (b) Framegrabber used to view the Pictures of the computer [28]

### 4.4.1 Volume reconstruction from Ultrasound imaging

A 3d volume is reconstructed using the ultrasound imaging taken by ProSound 2, Aloka Medical marketed by Hitachi, Ltd., with a linear tube coupled to an instrument Polaris Spectra, as can be seen in Fig 4.6(a). One framegrabber (Fig 4.6(b)) was used for acquiring images at 33 frames per second and to visualize them in computer. The images obtained from the ultrasound performed phantom having a matrix of  $576 \times 760$  pixels (Figure 2.1 (b)). A total of 276 images acquired, which forms a volume of  $512 \times 512 \times 276$  voxels. It is the ultrasound image of the vertebra no 2 and 3 mentioned in table 4.1.

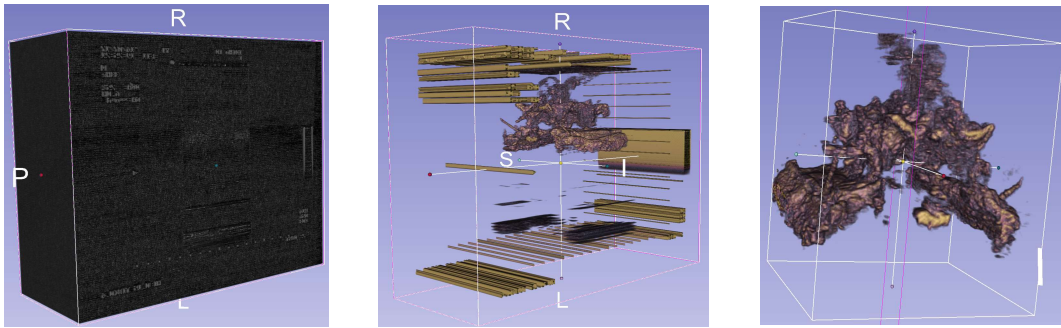


Fig 4. 7: Reconstructed Volume: a) 3D grid or volume is obtained by stacking all the ultrasound slices together, b) the same volume using a different colormap for better visualization the inverse structure of the vertebra no 2 and 3. C) cropped the region of interest

In order to extract the surface of the column in the US acquired images was necessary to cropped and segmentation. The crop volume module of 3d slicer was applied for getting region of interest (Fig 4). Therefore, a HU intensity value-based thresholding segmentation was perform using segmentations module of slicer that shown earlier this chapter. The Fig 4.8 shows the segmented ultrasound images below,

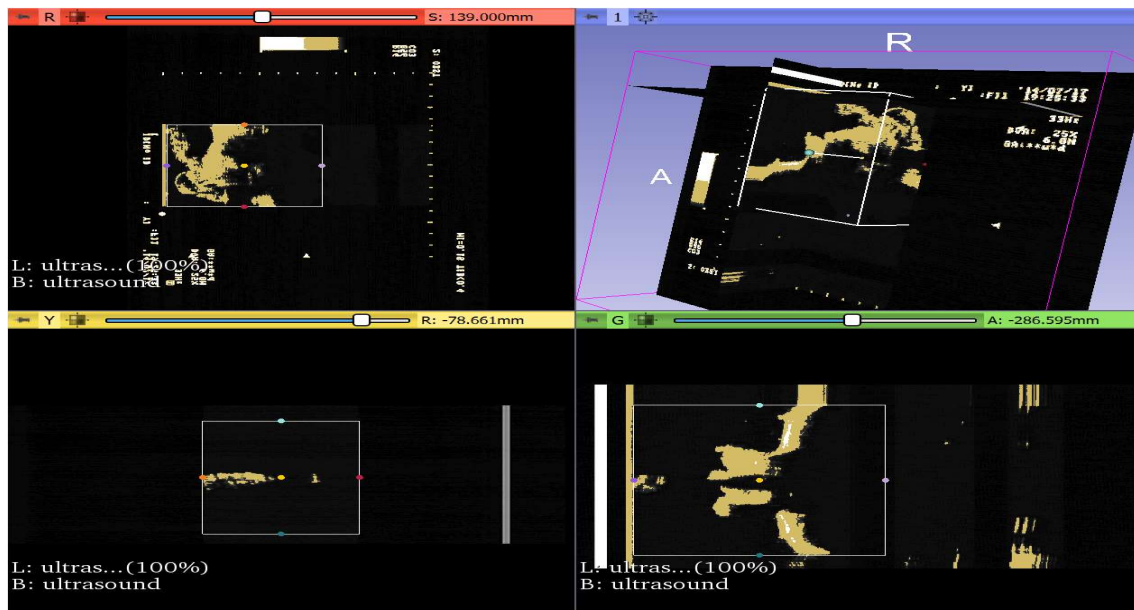


Fig 4. 8: Segmented ultrasound imaging: a) Top left: red screen shows Left axis, b) Bottom left: yellow screen shows Superior axis, c) Top right: 3d view, and d) Bottom right: green screen shows Posterior axis

Finally, a 3d model of inverse vertebra no 2 and 3 was reconstructed using MakeModelEffect operator of the editor module in 3d slicer. It shows in the Fig 4.9.

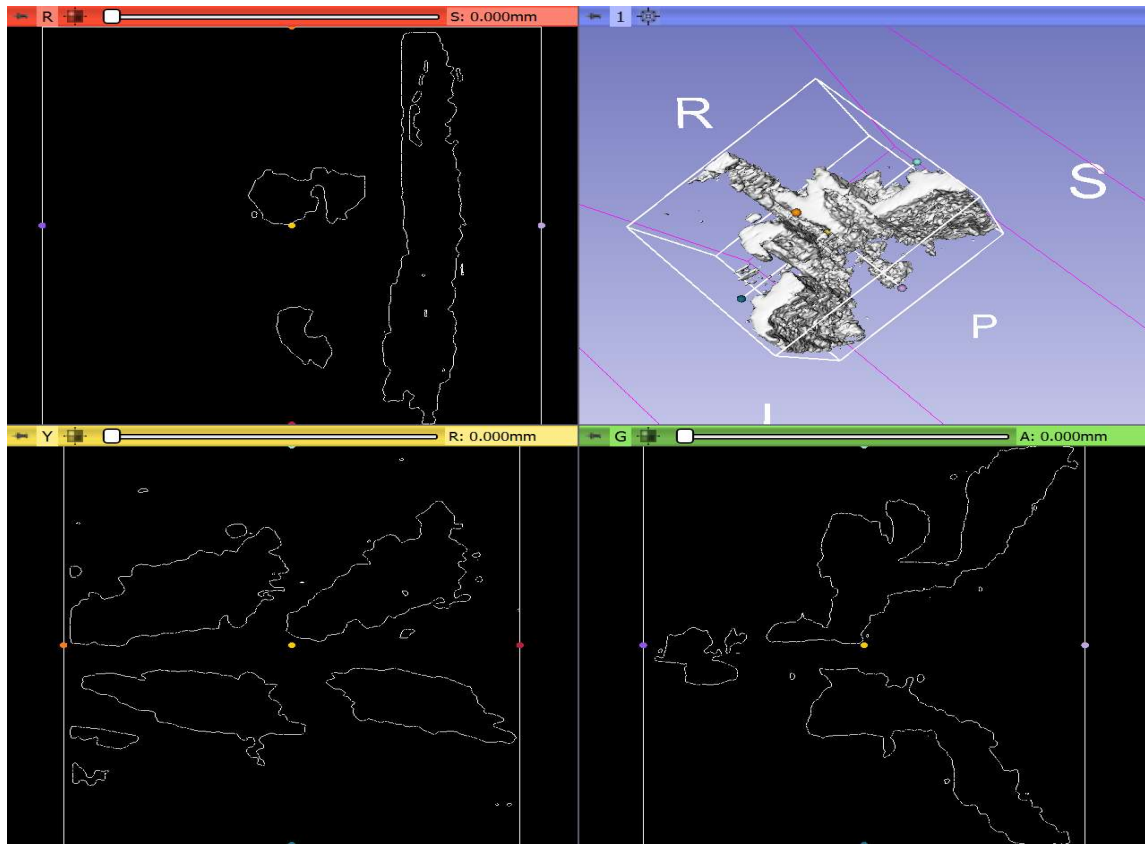


Fig 4. 9: 3d reconstructed model: a) Top left: red screen shows Left axis, b) Bottom left: yellow screen shows Superior axis, c) Top right: 3d view, and d) Bottom right: green screen shows Posterior axis



# Chapter 5

## Image Registration

Image registration methods are widely used in digital medical imaging for diagnosis of various disease and impacting to the treatment. It is an image processing technique that align one to one correspondence between the coordinates of two or more images, where images are taken by the single camera or different cameras at different times and at numerous viewpoints. The images and the objects with different scaling are co-registered, aligned, and geometrically transform [20]. Entirely, image registration technique finds the optimal geometric transformation which maximizes the correspondence between the images [52]. Each point  $x$  of the source image will be mapped an automatically corresponding location in the moving image  $T(x)$  after coordinate transform. Image registration technique are two types according to transformation [21]. The first type is linear transformations, which includes rotation, scaling, translation, and other affine transform [22]. They are global in nature and cannot model local geometric between images [23]. The second type is nonlinear transformations, which allows nonrigid or elastic transformations. They are capable of locally warping the target image to align with the reference image. However, it is very challenging to use image registration technique in medical imaging due to different patient positions, variation in the acquisition of the parameters, different equipment with different physical principles and coordinate systems, and structural variation due to disease or normal temporal variation [24]. The best image registration technique for images acquired from soft tissues such as breast, liver, prostate and brain is non-rigid registration. A rigid transformation is more suitable for bones, such as pelvis, femur and skull. In this chapter, closed form solution is presented, as Landmark registration module of 3d slicer are based on closed from solution. In addition, this chapter includes the description of the three different method of registration (Rigid, Affine and Non-Rigid) applied to the images and the point cloud.

### 5.1 Closed-Form Solution

Closed form solution is the method that provide absolute orientation to the least square problems for three or more points. This method does not involve any iteration process, it delivers the best possible solution in a single step. Closed from solution gives the best translational offset by measuring the difference between the centroid of the coordinates in one system and the rotated and scaled centroid of the coordinates in the other system. Moreover, the ratio of the root mean square deviations of the coordinates in the two systems from their respective centroids is the best scale. It uses unit quaternions

to represent the best rotations, where the eigenvector of a symmetric  $4 \times 4$  matrices associated with the most positive eigenvalue [30].

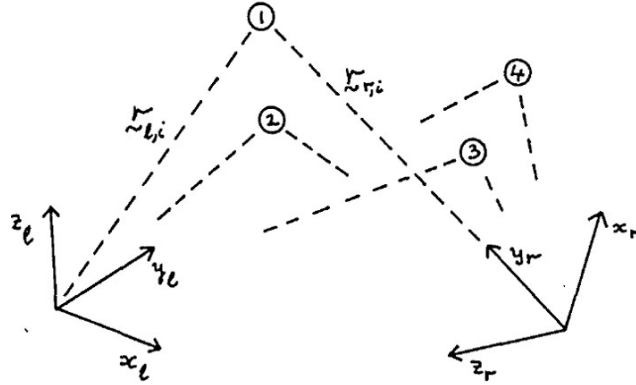


Fig 5. 1: The coordinates of a number of points is measured in two different coordinate systems. [30]

### 5.1.1 Finding the Translation

For  $n$  points, the left and right measured coordinates symbolized as  $\{r_{l,i}\}$  and  $\{r_{r,i}\}$ , where  $i$  ranges from 1 to  $n$ . The transformation from the left to right coordinate system represented as

$$r_r = s R(r_l) + r_0 \quad (5.1)$$

Here,  $s$  is a scale factor,  $R(r_l)$  represented the rotated version of the vector  $r_l$ , and  $r_0$  is the translational offset. The rotation is a linear operation and that it preserves lengths so that,

$$\|R(r_l)\|^2 = \|r_l\|^2 \quad (5.2)$$

Where  $\|r\|^2 = r \cdot r$  is the square of the length of the vector  $r$ .

As data are not perfect, there will be a residual error,

$$e_i = r_{r,i} - s R(r_{l,i}) - r_0 \quad (5.3)$$

The sum of the squats of the errors will be minimized.

$$\sum_{i=1}^n \|e_i\|^2 \quad (5.4)$$

Firstly, the total error with translation is considered, then scale, and finally with respect to rotation is considered.

### 5.1.2 Centroids of the sets of measurements

The centroid  $s$  of left and right coordinates defined as,

$$\bar{r}_l = \frac{1}{n} \sum_{i=1}^n r_{l,i} \quad \text{and} \quad \bar{r}_r = \frac{1}{n} \sum_{i=1}^n r_{r,i} \quad (5.5)$$

The new coordinates denoted by

$$r'_{l,i} = r_{l,i} - \bar{r}_l \quad \text{and} \quad r'_{r,i} = r_{r,i} - \bar{r}_r \quad (5.6)$$

Note that,

$$\sum_{i=1}^n r'_{l,i} = 0 \quad \text{and} \quad \sum_{i=1}^n r'_{r,i} = 0 \quad (5.7)$$

The error term can be rewritten as,

$$e_i = r'_{r,i} - s R(r'_{l,i}) - r'_0 \quad (5.8)$$

Where,

$$r'_0 = r_0 - \bar{r}_r + s R(\bar{r}_l) \quad (5.9)$$

The sum of the squares of the error,

$$\sum_{i=1}^n \|r'_{r,i} - s R(r'_{l,i}) - r'_0\|^2, \quad \text{or} \quad (5.10)$$

$$\sum_{i=1}^n \|r'_{r,i} - s R(r'_{l,i})\|^2 - 2r'_0 \cdot \sum_{i=1}^n (r'_{r,i} - s R(r'_{l,i})) + n\|r'_0\|^2 \quad (5.11)$$

The middle of this expression is zero, as the sum of the vectors  $\{r'_{r,i}\}$  and  $\{r'_{l,i}\}$  are zero. Moreover, the first term does not depend on  $r'_0$  and the last term cannot be negative. The total error minimized with  $r'_0 = 0$ , or  $r_0 = \bar{r}_r - s R(\bar{r}_l)$

The translation is gotten by the difference of the right centroid and the scaled and rotated left centroid. After finding scale and rotation the equation of the translational offset can be return. This method is based on measurements of one or a few selected points to estimate the translation.

The error term can be simplified as,

$$e_i = r'_{r,i} - s R(r'_{l,i}), \quad (5.12)$$

The total error minimized with  $r'_0 = 0$ ,

$$\sum_{i=1}^n \|r'_{r,i} - s R(r'_{l,i})\|^2 \quad (5.13)$$

### 5.1.3 Finding the Scale

Expanding the total error

$$\|R(r'_{l,i})\|^2 = \|r'_{l,i}\|^2, \quad (5.14)$$

$$\text{we obtain,} \quad \sum_{i=1}^n \|r'_{r,i}\|^2 - 2s \sum_{i=1}^n r'_{r,i} \cdot R(r'_{l,i}) + s^2 \sum_{i=1}^n \|r'_{l,i}\|^2 \quad (5.15)$$

which can be written in the form

$$S_r - 2sD + s^2 S_l \quad (5.16)$$

Where  $S_r$  and  $S_l$  are the sums of the squares of the measurement vector and  $D$  is the sum of the dot products of corresponding coordinates in the right system with the rotated coordinates in the left system. The square is completing in  $s$ ,

$$\text{We get, } (s\sqrt{S_l} - \frac{D}{\sqrt{S_l}})^2 + \frac{(S_l S_r - D^2)}{S_l} \quad (5.17)$$

When the first term is zero or  $s = \frac{D}{S_l}$ , this is minimized with respect to scale  $s$ ,

$$s = \frac{\sum_{i=1}^n r'_{r,i} \cdot R(r'_{l,i})}{\sum_{i=1}^n \|r'_{l,i}\|^2} \quad (5.18)$$

### 5.1.4 Symmetry in Scale

If, as an alternative of finding the best fit to the transformation,

$$r_r = s R(r_l) + r_0 \quad (5.19)$$

The best fit to the inverse transformation,

$$r_l = \bar{s} \bar{R}(r_r) + \bar{r}_0 \quad (5.20)$$

$$\bar{s} = \frac{1}{s}, \quad \bar{r}_0 = -\frac{1}{s} R^{-1}(r_0), \quad \bar{R} = R^{-1} \quad (5.21)$$

By replacing left and right, we find  $\bar{s} = \frac{\bar{D}}{S_r}$  or

$$\bar{s} = \frac{\sum_{i=1}^n r'_{r,i} \cdot \bar{R}(r'_{l,i})}{\sum_{i=1}^n \|r'_{l,i}\|^2} \quad (5.22)$$

For similar errors, symmetrical error term is

$$e_i = \frac{1}{\sqrt{s}} r'_{r,i} - \sqrt{s} R(r'_{l,i}), \quad (5.23)$$

Therefore, the total error becomes

$$\frac{1}{s} \sum_{i=1}^n \|r'_{r,i}\|^2 - 2 \sum_{i=1}^n r'_{r,i} \cdot (R(r'_{l,i})) + s \sum_{i=1}^n \|r'_{l,i}\|^2 \quad (5.24)$$

$$\text{Or } \frac{1}{s} S_r - 2D + s S_l \quad (5.25)$$

$$\text{Where, } S_r = \sum_{i=1}^n \|r'_{r,i}\|^2, \quad D = \sum_{i=1}^n r'_{r,i} \cdot (R(r'_{l,i})), \quad \text{and } S_l = \sum_{i=1}^n \|r'_{l,i}\|^2 \quad (5.26)$$

Completing the square in  $s$ , we obtain

$$(\sqrt{s} S_l - \frac{1}{\sqrt{s}} S_r)^2 + 2(S_l S_r - D) \quad (5.27)$$

When the first term is zero or  $s = \frac{S_r}{S_l}$ , this is minimized with respect to scale  $s$ ,

$$s = \sqrt{\frac{\sum_{i=1}^n \|r'_{r,i}\|^2}{\sum_{i=1}^n \|r'_{t,i}\|^2}} \quad (5.28)$$

This symmetrical result allows to determine the scale without knowing the rotation. But the determination of the rotation is not affected by the value of the scale factor. The remaining error can be minimized for each case by making  $D$  as large as possible. Moreover, the rotation must be chosen that make it as large as possible.

$$\sum_{i=1}^n r'_{r,i} \cdot (R(r'_{t,i})) \quad (5.29)$$

### 5.1.5 Unit Quaternions and Rotation

The angle between vectors and the rotation has no effect on the vector length. Where rotation preserves dot product and reflection also preserves dot products. The rotation can be represented by unit quaternions by mapping purely imaginary quaternions into purely imaginary quaternions in a way that dot products are preserved, as is the sense of cross products. The multiplication by unit quaternion preserves dot products between two quaternions.

$$(\dot{q}\dot{p}) \cdot (\dot{q}\dot{r}) = \dot{p} \cdot \dot{r}, \quad \text{where, } \dot{q} \cdot \dot{q} = 1 \quad (5.30)$$

Simple multiplication is not possible to represent rotation. The composite product is in used

$$\dot{r}' = \dot{q}\dot{r}\dot{q}^* \quad (5.31)$$

The purely imaginary is shown by expanding

$$\dot{q}\dot{r}\dot{q}^* = (Q\dot{r})\dot{q}^* = \bar{Q}^T(Q\dot{r}) = (\bar{Q}^T Q)\dot{r} \quad (5.32)$$

$Q$  and  $\bar{Q}$  are the  $4 \times 4$  matrices corresponding to  $\dot{q}$ .

$$\bar{Q}^T Q = \begin{bmatrix} \dot{q} \cdot \dot{q} & 0 & 0 & 0 \\ 0 & (q_0^2 + q_x^2 - q_y^2 - q_z^2) & 2(q_y q_x - q_0 q_z) & 2(q_z q_x + q_0 q_y) \\ 0 & 2(q_y q_x + q_0 q_z) & (q_0^2 - q_x^2 + q_y^2 - q_z^2) & 2(q_z q_y - q_0 q_x) \\ 0 & 2(q_z q_x - q_0 q_y) & 2(q_z q_y + q_0 q_x) & (q_0^2 - q_x^2 - q_y^2 + q_z^2) \end{bmatrix} \quad (5.33)$$

If  $\dot{q}$  is a unit quaternion,  $Q$  and  $\bar{Q}$  are orthonormal. Whereas,  $\dot{r}'$  is purely imaginary because  $\dot{r}$  is purely imaginary. Therefore,  $3 \times 3$  submatrix of the lower right of  $\bar{Q}^T Q$  have to be orthonormal. Finally, the rotation matrix  $R$  between  $r$  and  $r'$  can be

$$r' = Rr \quad (5.34)$$

The reflection is not being dealt, only rotation is considered. Because, the cross products are preserved by the composite product  $\dot{q}\dot{r}\dot{q}^*$ ,

$$(-\dot{q})\dot{r}(-\dot{q}^*) = \dot{q}\dot{r}\dot{q}^* \quad (5.35)$$

The computation of the orthonormal rotation matrix shows above is explicit. While, unit quaternion can be recovered from an orthonormal matrix. Where, the unit quaternion can be represented by unit vector  $\hat{\omega} = (\omega_x, \omega_y, \omega_z)^T$  and angle  $\theta$  about the axis

$$\hat{q} = \cos \frac{\theta}{2} + \sin \frac{\theta}{2} (i\omega_x + j\omega_y + k\omega_z) \quad (5.36)$$

### 5.1.6 Composition of Rotation

Considering the rotation  $r' = \hat{q}r\hat{q}^*$  and apply a second rotation

$$r'' = \hat{p}r'\hat{p}^* = \hat{p}(\hat{q}r\hat{q}^*)\hat{p}^* \quad (5.37)$$

After easy verification with  $(q^*p^*) = (pq)^*$ , it can be written as

$$r'' = (\hat{p}\hat{q})r(\hat{p}\hat{q})^* \quad (5.38)$$

By unit quaternion  $(\hat{p}\hat{q})$ , the overall rotation is represented

### 5.1.7 Finding the Best Rotation

It is the main challenge to find the unit quaternion  $\hat{q}$ , that maximizes

$$\sum_{i=1}^n (\hat{q}r'_{l,i}\hat{q}^*) \cdot r'_{r,i} \quad (5.39)$$

The equation can be written applying one of the results derived above,

$$\sum_{i=1}^n (\hat{q}r'_{l,i}) \cdot (r'_{r,i}\hat{q}) \quad (5.40)$$

Considering that  $r'_{l,i} = (x'_{l,i}, y'_{l,i}, z'_{l,i})^T$  and  $r'_{r,i} = (x'_{r,i}, y'_{r,i}, z'_{r,i})^T$ , We obtain

$$\hat{q}r'_{l,i} = \begin{bmatrix} 0 & -x'_{l,i} & -y'_{l,i} & -z'_{l,i} \\ x'_{l,i} & 0 & z'_{l,i} & -y'_{l,i} \\ y'_{l,i} & -z'_{l,i} & 0 & x'_{l,i} \\ z'_{l,i} & y'_{l,i} & -x'_{l,i} & 0 \end{bmatrix} \hat{q} = \bar{\mathbb{R}}_{l,i} \hat{q} \quad (5.41)$$

$$r'_{r,i}\hat{q} = \begin{bmatrix} 0 & -x'_{r,i} & -y'_{r,i} & -z'_{r,i} \\ x'_{r,i} & 0 & z'_{r,i} & -y'_{r,i} \\ y'_{r,i} & -z'_{r,i} & 0 & x'_{r,i} \\ z'_{r,i} & y'_{r,i} & -x'_{r,i} & 0 \end{bmatrix} \hat{q} = \mathbb{R}_{r,i} \hat{q} \quad (5.42)$$

$\mathbb{R}_{r,i}$  and  $\bar{\mathbb{R}}_{l,i}$  are orthogonal and skew symmetric. The sum written below must be maximize

$$\sum_{i=1}^n (\bar{\mathbb{R}}_{l,i} \hat{q}) \cdot (\mathbb{R}_{r,i} \hat{q}) \quad \text{or} \quad \sum_{i=1}^n \hat{q}^T \bar{\mathbb{R}}_{l,i}^T \cdot \mathbb{R}_{r,i} \hat{q} \quad (5.43)$$

$$\text{That is, } \hat{q}^T (\sum_{i=1}^n \bar{\mathbb{R}}_{l,i}^T \cdot \mathbb{R}_{r,i}) \hat{q} \quad \text{or} \quad \hat{q}^T (\sum_{i=1}^n N_i) \hat{q} = \hat{q}^T N \hat{q} \quad (5.44)$$

where  $N_i = \bar{\mathbb{R}}_{l,i}^T \mathbb{R}_{r,i}$  and  $N = \sum_{i=1}^n N_i$ . If each of the  $N_i$  matrices are symmetric, so  $N$  must be symmetric.

### 5.1.8 Matrix of Sums of Product

$M$  is a  $3 \times 3$  matrix whose elements are sums of products of coordinates measured in the left system with coordinates measures in the right system.

$$M = \sum_{i=1}^n r'_{l,i} r'_{r,i}{}^T \quad (5.45)$$

$M$  matrix contains all the information that needed to solve the least square problem for rotation.  $M$  can be written as

$$M = \begin{bmatrix} S_{xx} & S_{xy} & S_{xz} \\ S_{yx} & S_{yy} & S_{yz} \\ S_{zx} & S_{zy} & S_{zz} \end{bmatrix} \quad (5.46)$$

$$\text{where, } S_{xx} = \sum_{i=1}^n x'_{l,i} x'_{r,i}, \quad S_{xy} = \sum_{i=1}^n x'_{l,i} y'_{r,i} \quad (5.47)$$

$$N = \begin{bmatrix} S_{xx} + S_{yy} + S_{zz} & S_{xx} - S_{yy} & S_{zx} - S_{xz} & S_{xy} - S_{yx} \\ S_{yz} - S_{zy} & S_{xx} - S_{yy} - S_{zz} & S_{xy} + S_{yx} & S_{zx} + S_{xz} \\ S_{zx} - S_{xz} & S_{xy} + S_{yx} & -S_{xx} + S_{yy} - S_{zz} & S_{yz} + S_{zy} \\ S_{xy} - S_{yx} & S_{zx} + S_{xz} & S_{yz} + S_{zy} & -S_{xx} - S_{yy} + S_{zz} \end{bmatrix} \quad (5.48)$$

### 5.1.9 Eigenvector Maximizes Matrix Product

The unit quaternion that maximizes the eigen vector corresponding to the most

$$\dot{q}^T N \dot{q} \quad (5.49)$$

positive eigenvalue of matrix  $N$ .

$$\det(N - \lambda I) = 0 \quad (5.50)$$

where  $I$  is the  $4 \times 4$  identity matrix. The coefficients of the polynomial can be computed from the elements of the matrix  $N$  using the equation above.

The eigenvector  $\dot{e}_m$  was calculating by solving the homogeneous equation below after selecting the largest eigenvalue  $\lambda_m$ .

$$[N - \lambda_m I] \dot{e}_m = 0 \quad (5.51)$$

### 5.1.10 Rotation in the Plane

The rotation in the plane of the righthand measurements must be found in a way that minimizes the sum of squares of distances between corresponding measurements.

$$\sum_{i=1}^n \|r'_{r,i} - r''_{l,i}\|^2 \quad (5.52)$$

The angle between corresponding measurements is  $\alpha_i$

$$r'_{r,i} r''_{l,i} \cos \alpha_i = r'_{r,i} \cdot r''_{l,i} \quad \text{and} \quad r'_{r,i} r''_{l,i} \sin \alpha_i = (r'_{r,i} \times r''_{l,i}) \cdot \widehat{n}_r \quad (5.53)$$

$$\text{where } r'_{r,i} = \|r'_{r,i}\|, \quad r''_{l,i} = \|r''_{l,i}\| = \|r'_{l,i}\| \quad (5.54)$$

$r'_{r,i} \times r''_{l,i}$  is parallel to  $\widehat{n}_r$  and the dot product between them has a magnitude

$$\|r'_{r,i} \times r''_{l,i}\| \quad (5.55)$$

However, the sign depends on the order of  $r'_{r,i}$  and  $r''_{l,i}$  in the plane.

The square of the distance between corresponding measurement is achieved using the cosine rule for triangle.

$$(r'_{r,i})^2 + (r''_{l,i})^2 - 2r'_{r,i}r''_{l,i} \cos \alpha_i \quad (5.56)$$

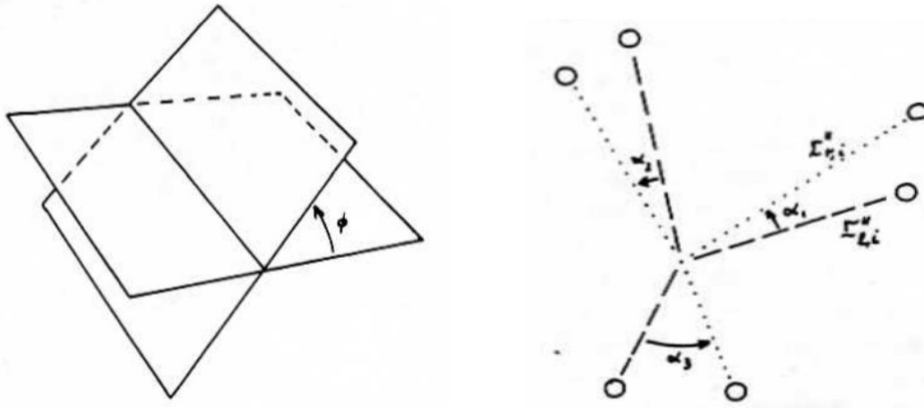


Fig 5. 2: a) Two coordinate systems have been aligned and superimposed. b) The second rotation, when both sets of measurements are coplanar, is about the normal of one of the planes. <sup>[30]</sup>

The angles  $\alpha_i$  are reduced by  $\theta$ , while the left measurements are rotated in the plane through an angle  $\theta$ .

$$\sum_{i=1}^n r'_{r,i} r''_{l,i} \cos(\alpha_i - \theta) \quad \text{or} \quad C \cos \theta + S \sin \theta \quad (5.57)$$

$$\text{where, } C = \sum_{i=1}^n r'_{r,i} r''_{l,i} \cos \alpha_i = \sum_{i=1}^n (r'_{r,i} \cdot r''_{l,i}) \quad (5.58)$$

$$\text{and } S = \sum_{i=1}^n r'_{r,i} r''_{l,i} \sin \alpha_i = (\sum_{i=1}^n r'_{r,i} \times r''_{l,i}) \cdot \widehat{n}_r \quad (5.59)$$

This expression has extrema where

$$C \cos \theta = S \sin \theta \quad (5.60)$$

$$\text{or } \sin \theta = \pm \frac{S}{\sqrt{S^2+C^2}}, \quad \cos \theta = \pm \frac{C}{\sqrt{S^2+C^2}} \quad (5.61)$$

$$\text{The extreme values are } \pm\sqrt{S^2+C^2} \quad (5.62)$$

The second rotation can be presented by the unit quaternion

$$\dot{q}_p = \cos \frac{\theta}{2} + \sin \frac{\theta}{2} (in_x + jn_y + kn_z) \quad (5.63)$$

The overall rotation is presented as

$$\dot{q} = \dot{q}_p \dot{q}_a \quad \text{or} \quad R = R_p R_a \quad (5.64)$$

## 5.2 Rigid Registration

The rigid registration is one of the simplest image registration method that are related by rotation and translation [31]. It is a linear coordinate transform that describes six degrees of freedom which includes three rotation and three translations. Rigid registration can be measured by feature based and intensity based. Features includes points, lines, vectors, surfaces, volumes, that are extracted from images prior to similarity measure. The main step of features-based registration is to identify and extract the homologous points or control points. In medical imaging registration, these points can be bones or artificial spots introduced in body for helping the registration.

### 5.2.1 Point Cloud based Rigid Registration

For optimizing the points distance between homologous points, a features-based rigid registration is used. Where, the least squares rigid motion using SVD method is introduced to compute the rigid registration.

least squares rigid motion using SVD method

Problem statement:

The two sets of points  $P = p_1, p_2, p_3, p_4$  and  $Q = q_1, q_2, q_3, q_4$  are placed corresponding to pedicle screw and CT of vertebrae. Finding a rigid transformation is the principle goal where optimally aligns the two sets in the least squares sense.

$$(R, T) = \text{argmin} \sum_{i=1}^n \omega_i \|(R * p_i + T) - q_i\|^2 \quad (5.65)$$

where,  $\omega_i > 0$  are weights for each point pair. Each point will have the same weight 1 in the first analysis. Later the weights for the inside points will be lighter than the outside points. R is assumed to be fixed for computing the translation, T.

The center of mass for point set P and Q is

$$\bar{p} = \frac{\sum_{i=1}^n \omega_i p_i}{\sum_{i=1}^n \omega_i} \quad \bar{q} = \frac{\sum_{i=1}^n \omega_i q_i}{\sum_{i=1}^n \omega_i} \quad (5.66)$$

The derivative of Eq. 5.65 is taken for finding optimal translation [32]. After computing the derivative and rearranging the terms

$$t = \bar{q} - R\bar{p} \quad (5.67)$$

The optimal translation T maps the transformed weighted centroid of P to the weighted centroid of Q. Compute the distance from each point to the centroid.

$$x_i = p_i - \bar{p}, \quad y_i = q_i - \bar{q} \quad (5.68)$$

The Eq. 5.65 becomes

$$(R, T) = \operatorname{argmin} \sum_{i=1}^n \omega_i \|(Rx_i) - y_i\|^2 \quad (5.69)$$

Singular Value Decomposition (SVD):

Singular Value Decomposition is used for finding optimal rotation. Where covariance matrix E is

$$E = x' * W * y \quad (5.70)$$

where, x and y are matrices and  $x_i, y_i$  as their columns. W is a diagonal with the weight  $\omega_i$  on diagonal entry i. The matrix E is factorized or decomposed into three other matrices using SVD. The rotation matrix is found using this method [33].

$$[U, S, V] = \operatorname{SVD}(E) \quad E = USV^T \quad (5.71)$$

Where U and V are orthogonal  $m \times m$  matrices

$$R = VU^T \quad (5.72)$$

Both data sets will be re-center for finding the optimal rotation, that both centroids are at the origin. Therefore, the whole process can be summarized as: firstly, the computation of the weighted centroids of both point sets  $q$  and  $p$ . Secondly, the computation of the distance between each point to the centroid and set in X and Y matrices. Thirdly, the computation of the covariance matrix,  $S = XWY^T$ . Fourthly, the computation of the singular value decomposition  $S = U\Sigma V^T$  to find the rotation  $R = VU^T$ . Finally, the computation of the optimal translation  $T = q - Rp$

### 5.3 Point Cloud based Affine Registration

It is not possible to deal with geometric distortion using rigid registration, as it required more degrees of freedom to deal with. Affine registration is the image processing technique that allows to deform the

image to better fit the data. It is a nonlinear coordinate transformation that describes 12 DOF, which includes three rotation, three translation, three scaling and three shear [34]. The three scaling and three shear allows changing the geometry of the original image. By this way, affine registration overcome the limitations in the rigid transformation.

The affine transform  $T$  takes  $p = (p_1, p_2, \dots, p_n) \in \mathbb{R}^d$  to  $q = (q_1, q_2, \dots, q_n)$  written as [33]

$$q = R * p + c \quad (5.73)$$

Where  $p$  points are the centers of the moving data set,  $q$  are the center of the fixed data set,  $c$  corresponds to translation, and  $R$  includes rotation, scaling and shear. The affine transformation become linear if  $c$  is zero. Fig 5.3 c shows affine transformation.

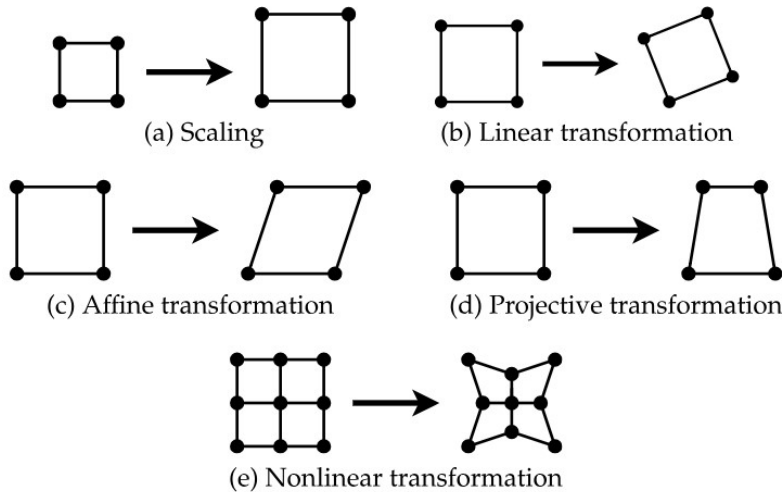


Fig 5. 3: Transformation types <sup>(13)</sup>

## 5.4 Non-Rigid Registration (NRR):

Handling distortion in the images is a changing task for medical image processing. It requires more degrees of freedom than the rigid registration [37]. Although, object might be rigid, if distortion is present, least squares rigid motion SVD method unable to deal with the problem. Non-rigid registration is the image processing technique that capable to handle images with distortion. The non-rigid registration can be expressed,

$$T(r) = r + d(r) \quad (5.74)$$

where, parameters are described as transformation  $T(r)$ , deformation  $d(r)$ , and  $r$  is  $(x, y, z)$ . As it is a nonlinear registration technique which uses image intensities for computing the transformation. The transform maps the points in the moving reference coordinate to the corresponding points in the fixed reference coordinate. There are several methods to achieve non-rigid registration. However, here in

this study, non-rigid iterative closest point (ICP) is used for computing the transform between CT and ultrasound images.

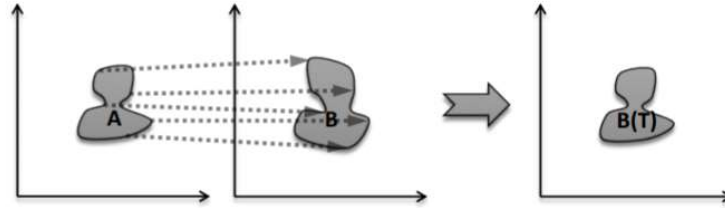


Fig 5. 4: Non-rigid registration: Vector field (aka deformation field) T is computed from A to B <sup>(15)</sup>

Non-rigid registration ICP:

Iterative closest point optimizer can be express as

$$E_{tot} = E_{plane} + \lambda E_{point} \quad \text{where, } \lambda \approx 0.1 \quad (5.75)$$

Point to point metric [30], Fig 5.5,

$$E_{point} = \sum_i ||(Rx_i + t - c_i)||^2 \quad (5.76)$$

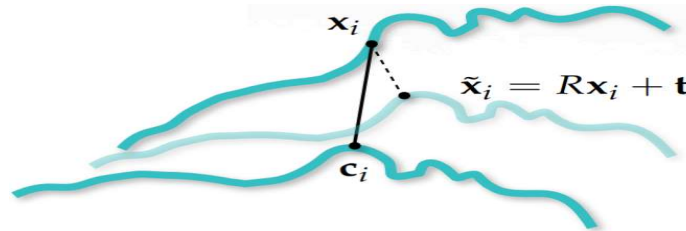


Fig 5. 5: Graphical representation of the energy term for point <sup>(14)</sup>

where,  $c_i$  is the point set in target,  $x_i$  point set in source, translation vector  $t$ , and rotation matrix  $R$ .

Energy equation of plane show below (Chen and Medioni'91), Fig 5.6,

$$E_{plane} = \sum_i ||n_i^t (Rx_i + t - c_i)||^2 \quad [ \sin(\theta) \approx \theta, \cos(\theta) \approx 1 ] \quad (5.77)$$

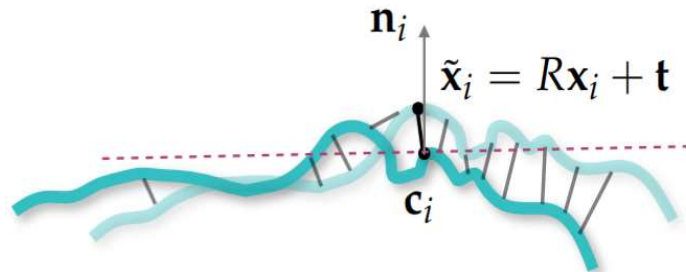


Fig 5. 6: Graphical representation of the energy term for plane <sup>(14)</sup>

Eq 5.78 is the non-linear energy minimizer equation [36]. It Where,  $E_{smooth}$  regularizes the deformation locally and  $E_{rigid}$  measures deviation from rigid motion

$$E_{tot} = E_{plane} + \alpha_{point}E_{point} + \alpha_{rigid}E_{rigid} + \alpha_{smo} E_{smooth} \quad (5.78)$$

The  $E_{rigid}$  is the energy of rigid. It penalized the deviation of each transformation from a pure rigid motion [35]. It defines as

$$E_{rigid} = \sum_i Rot(A_i) \quad (5.79)$$

$$\text{where, } Rot(A) = (a_1^t a_2)^2 + (a_1^t a_3)^2 + (a_2^t a_3)^2 + (1 - a_1^t a_1)^2 + (1 - a_2^t a_2)^2 + (1 - a_3^t a_3)^2 \quad (5.80)$$

$a_1, a_2,$  and  $a_3$  are the column vector of  $A_i$ .

$$E_{smooth} = \sum_i \sum_{j \in N(i)} \|A_i(x_j - x_i) + x_i + b_i - (x_j + b_j)\|_2^2 \quad (5.81)$$

where,  $N(i)$  consists of all nodes that share an edge with node  $i$ .

Correspondence:

Now correspondence is considered for getting final objective function of the optimization. Here, the coupled optimization [35].

$$E = \alpha_{rigid}E_{rigid} + \alpha_{smooth}E_{smooth} + \alpha_{fit}E_{fit}^* + \alpha_{conf}E_{conf} \quad (5.82)$$

It minimizes deformation energy, alignment error and regions of overlap.

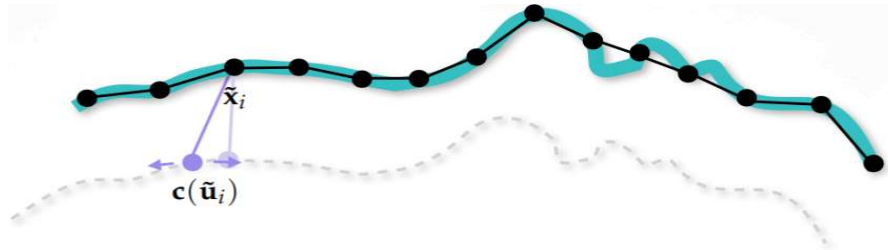


Fig 5. 7: Graphical representation of the term  $E_{fit}^{*}$  <sup>(14)</sup>

The  $E_{fit}^*$  and  $E_{conf}$  terms can be defined by, Fig 5.7,

$$E_{fit}^* = \sum_{i=1}^n \omega_i^2 \|\tilde{x}_i - c(\tilde{u}_i)\|_2^2 \quad (5.83)$$

$$E_{conf} = \sum_{i=1}^n (1 - \omega_i^2)^2 \quad (5.84)$$

where,  $c(\tilde{u}_i)$  is the function that maps from the parameter domain back to the three-dimensional position. The reliability of correspondence is depending on the values of  $\omega_i$ , where  $\omega_i$  close to one indicate a reliable correspondence and values close to zero indicate that no appropriate correspondence is found.



# Chapter 6

## Results and Discussion

This chapter presents the results of point to point based landmark registration, where 3D slicer opensource software was used for landmark registration. Therefore, a matlab program was developed for finding intersection point of pedicle screw in both side (left and right) of all vertebra of pig spine using the results obtained from landmark registration. In addition, the angle in LR axis and SI axis was found for guiding the pedicle screw placement. Finally, it was successfully placed pedicle screws in both sides of all vertebra.

### 6.1 Pedicle Screw Placement Process

Pedicle screw placement process includes steps,

- 1) Firstly, the point to point base landmark registration or fiducial registration initiated by choosing four landmarks on pedicle screw (Fig 6.1).
- 2) Therefore, four landmarks were chosen for each pedicle of vertebra.
- 3) Then, Fiducial registration was done between landmarks of pedicle screw and landmarks on pedicle of vertebra model developed from CT, were development of vertebrae from CT is shown in chapter four. Here, landmarks on pedicle screw is moving reference and landmarks on pedicle of vertebra is fixed reference.
- 4) After the fiducial registration, we got a rotation and transformation matrix of registered pedicel screw and root mean square (RMS) error.
- 5) In this step, an intersection point for pedicle screw and an angle in LR and an angle in SI axis is calculated using the output of the fiducial registration. Here, the out file is extracted from 3D slicer as .mat file and a MATLAB program was developed for calculation using the output file.

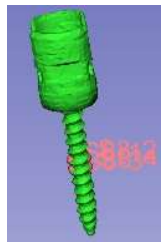


Fig 6. 1: Landmarks on pedicle screw

### 6.1.1 Fiducial Registration

Here, rigid registration is done between landmarks on pedicle screw and landmark on pedicle of vertebra using fiducial registration. After the registration, a transformation matrix describes the new location of landmarks on pedicle screw by rotation and translate. Therefore, using the transformation the angle in LR axis, the angle in SI axis and the intersection point for pedicle screw is calculated.

#### Left Pedicle of Vertebra 1

$$\text{Rotation, } R = \begin{bmatrix} 0.78 & 0.62 & 0 \\ -0.62 & 0.78 & 0 \\ 0 & 0 & 1 \end{bmatrix} \quad \text{Translation, } t = \begin{bmatrix} -0.55 \\ -194.11 \\ -395.01 \end{bmatrix} \quad (6.1)$$

Angle in LR axis,  $\alpha = 38.65^\circ$ , Angle in SI axis,  $\gamma = 1.1^\circ$ ,

$$\text{Intersection point, } I = \begin{bmatrix} 15.25 \\ -174.35 \\ -395.01 \end{bmatrix} \quad (6.2)$$

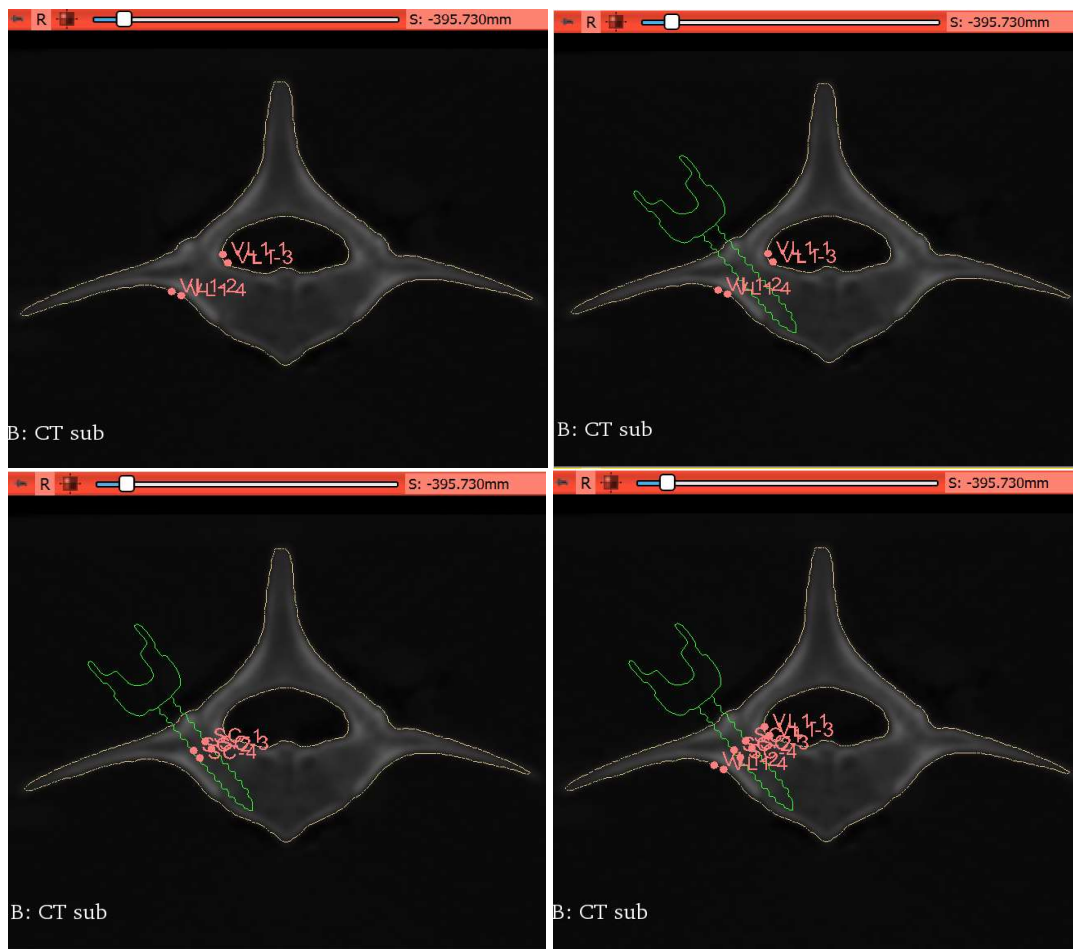


Fig 6. 2: Left axis view of left pedicle of vertebra 1: a) Top left: Landmarks on vertebra, b) Top right: Pedicle screw placed into vertebra, c) Bottom left: Translated Landmarks on pedicle screw, and d) Bottom right: Vertebra after the registration

Root mean square (RMS) Error = 4.67221

## Right Pedicle of Vertebra 1

$$\text{Rotation, } R = \begin{bmatrix} 0.82 & -0.57 & 0 \\ 0.57 & 0.82 & 0 \\ 0 & 0 & 1 \end{bmatrix} \quad \text{Translation, } t = \begin{bmatrix} -13.63 \\ -194.54 \\ -395.01 \end{bmatrix} \quad (6.3)$$

Angle in LR axis,  $\alpha = 34.5^\circ$ , Angle in SI axis,  $\gamma = 2.4^\circ$ ,

$$\text{Intersection point, } I = \begin{bmatrix} -27.39 \\ -174.51 \\ -395.01 \end{bmatrix} \quad (6.4)$$

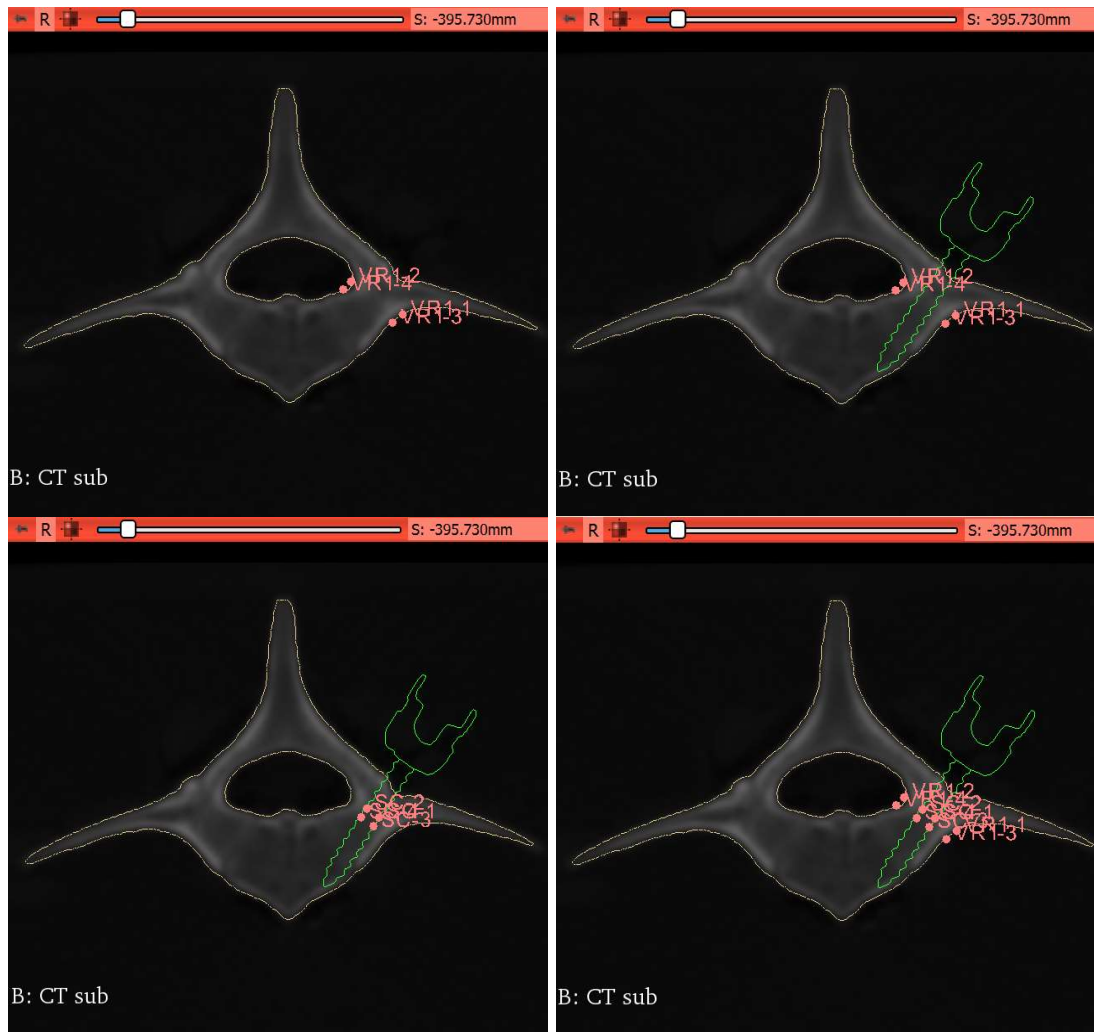


Fig 6. 3: Left axis view of right pedicle of vertebra 1: a) Top left: Landmarks on vertebra, b) Top right: Pedicle screw placed into vertebra, c) Bottom left: Translated Landmarks on pedicle screw, and d) Bottom right: Vertebra after the registration

Root mean square (RMS) Error = 4.48032

## Left Pedicle of Vertebra 2

$$\text{Rotation, } R = \begin{bmatrix} -0.83 & 0.56 & 0 \\ 0.56 & 0.83 & 0 \\ 0 & 0 & -1 \end{bmatrix} \quad \text{Translation, } t = \begin{bmatrix} -0.72 \\ -197.50 \\ -358.55 \end{bmatrix} \quad (6.5)$$

Angle in LR axis,  $\alpha = 34.28^\circ$ , Angle in SI axis,  $\gamma = 1.2^\circ$ ,

$$\text{Intersection point, } I = \begin{bmatrix} 14.2 \\ -175.60 \\ -358.55 \end{bmatrix} \quad (6.6)$$

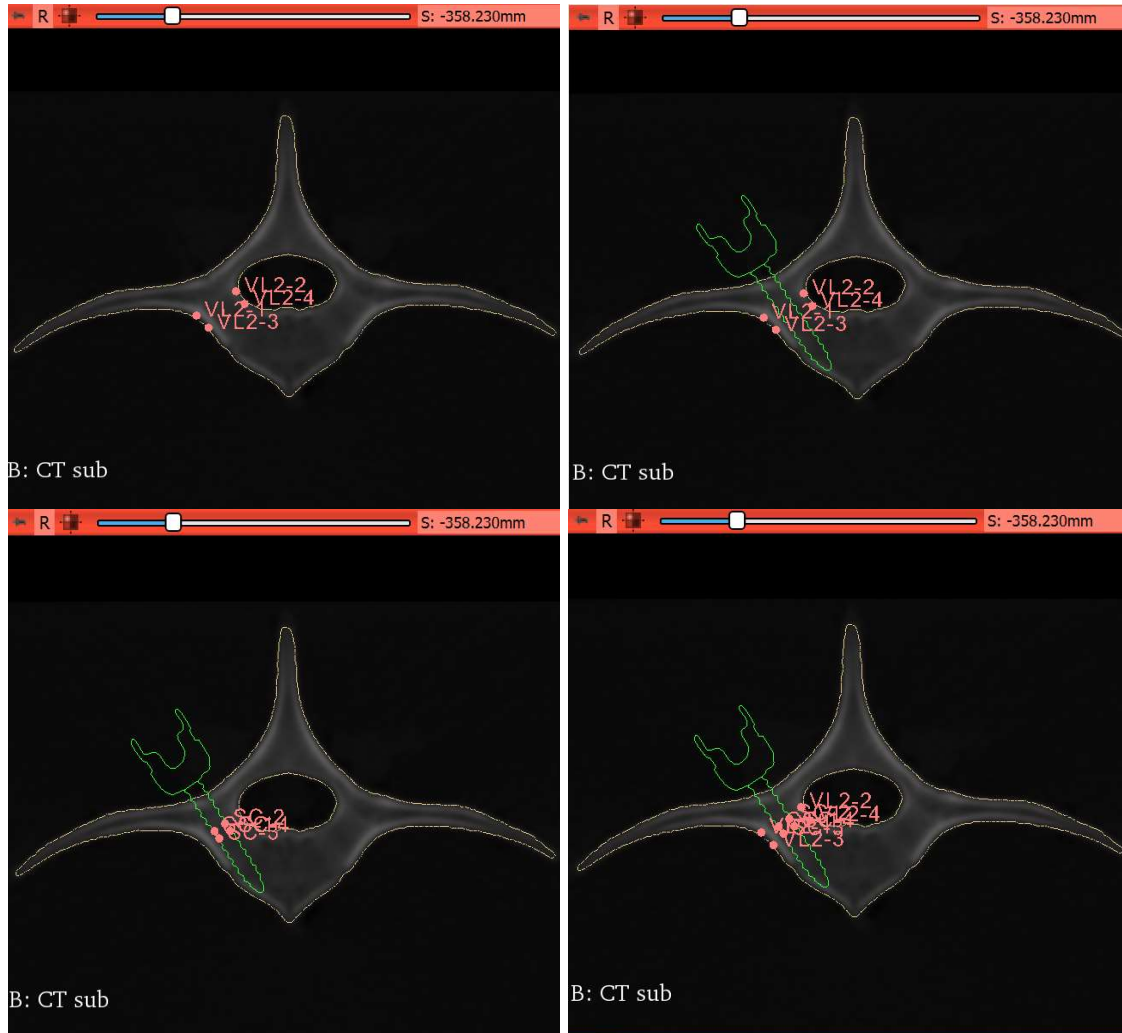


Fig 6. 4: Left axis view of left pedicle of vertebra 2: a) Top left: Landmarks on vertebra, b) Top right: Pedicle screw placed into vertebra, c) Bottom left: Translated Landmarks on pedicle screw, and d) Bottom right: Vertebra after the registration

Root mean square (RMS) Error = 3.86425

## Right Pedicle of Vertebra 2

$$\text{Rotation, } R = \begin{bmatrix} 0.81 & -0.59 & 0 \\ 0.59 & 0.81 & 0 \\ 0 & 0 & 1 \end{bmatrix} \quad \text{Translation, } t = \begin{bmatrix} -11.63 \\ -196.70 \\ -358.73 \end{bmatrix} \quad (6.7)$$

Angle in LR axis,  $\alpha = 35.81^\circ$ , Angle in SI axis,  $\gamma = 2.7^\circ$ ,

$$\text{Intersection point, } I = \begin{bmatrix} -27.14 \\ -175.21 \\ -358.55 \end{bmatrix} \quad (6.8)$$

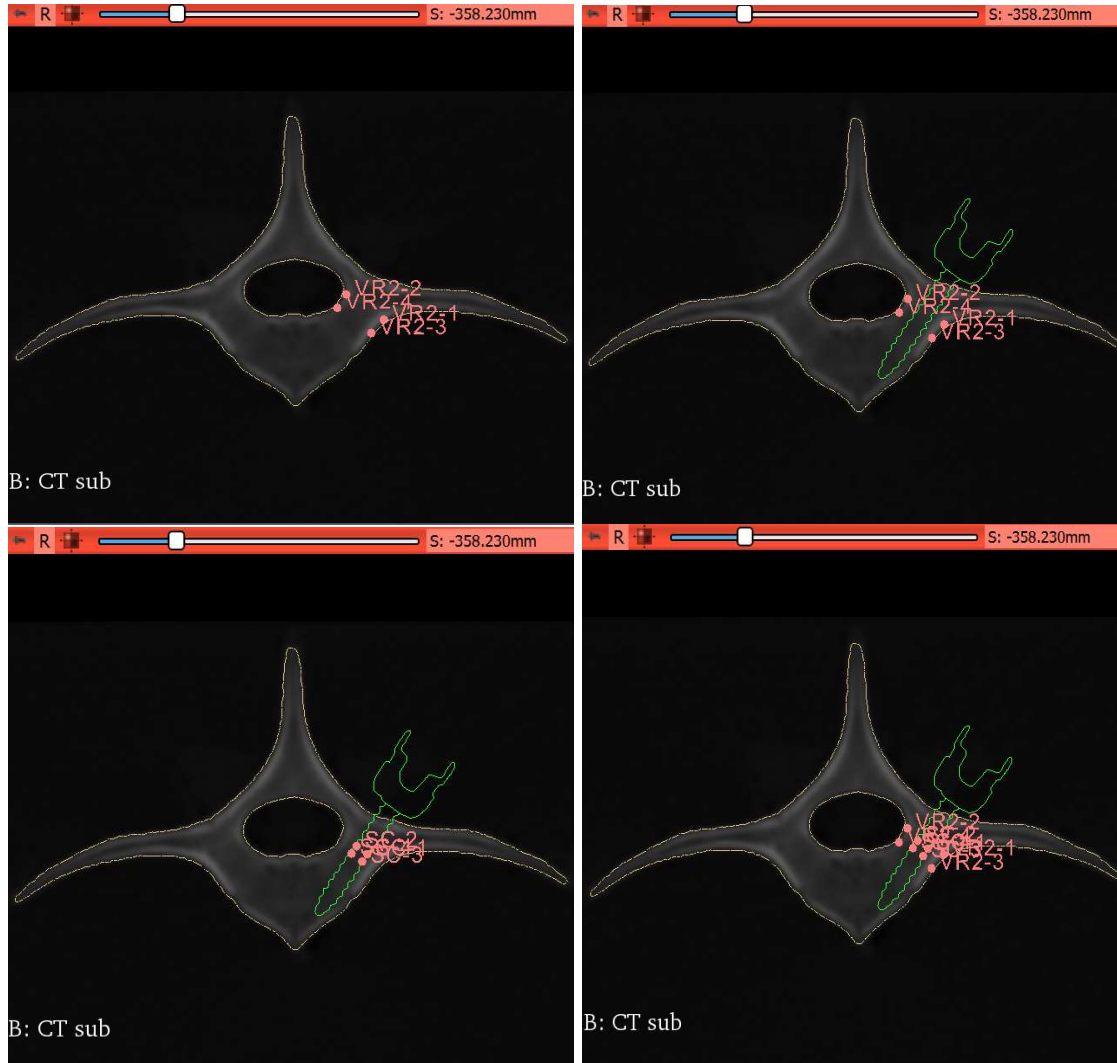


Fig 6. 5: Left axis view of right pedicle of vertebra 2: a) Top left: Landmarks on vertebra, b) Top right: Pedicle screw placed into vertebra, c) Bottom left: Translated Landmarks on pedicle screw, and d) Bottom right: Vertebra after the registration

Root mean square (RMS) Error = 3.65192

### Left Pedicle of Vertebra 3

$$\text{Rotation, } R = \begin{bmatrix} 0.87 & 0.49 & 0 \\ -0.49 & 0.81 & 0 \\ 0 & 0 & 1 \end{bmatrix} \quad \text{Translation, } t = \begin{bmatrix} 0.03 \\ -198.09 \\ -319.76 \end{bmatrix} \quad (6.9)$$

Angle in LR axis,  $\alpha = 29.03^\circ$ , Angle in SI axis,  $\gamma = 2^\circ$ ,

$$\text{Intersection point, } I = \begin{bmatrix} 12.84 \\ -175 \\ -319.76 \end{bmatrix} \quad (6.10)$$

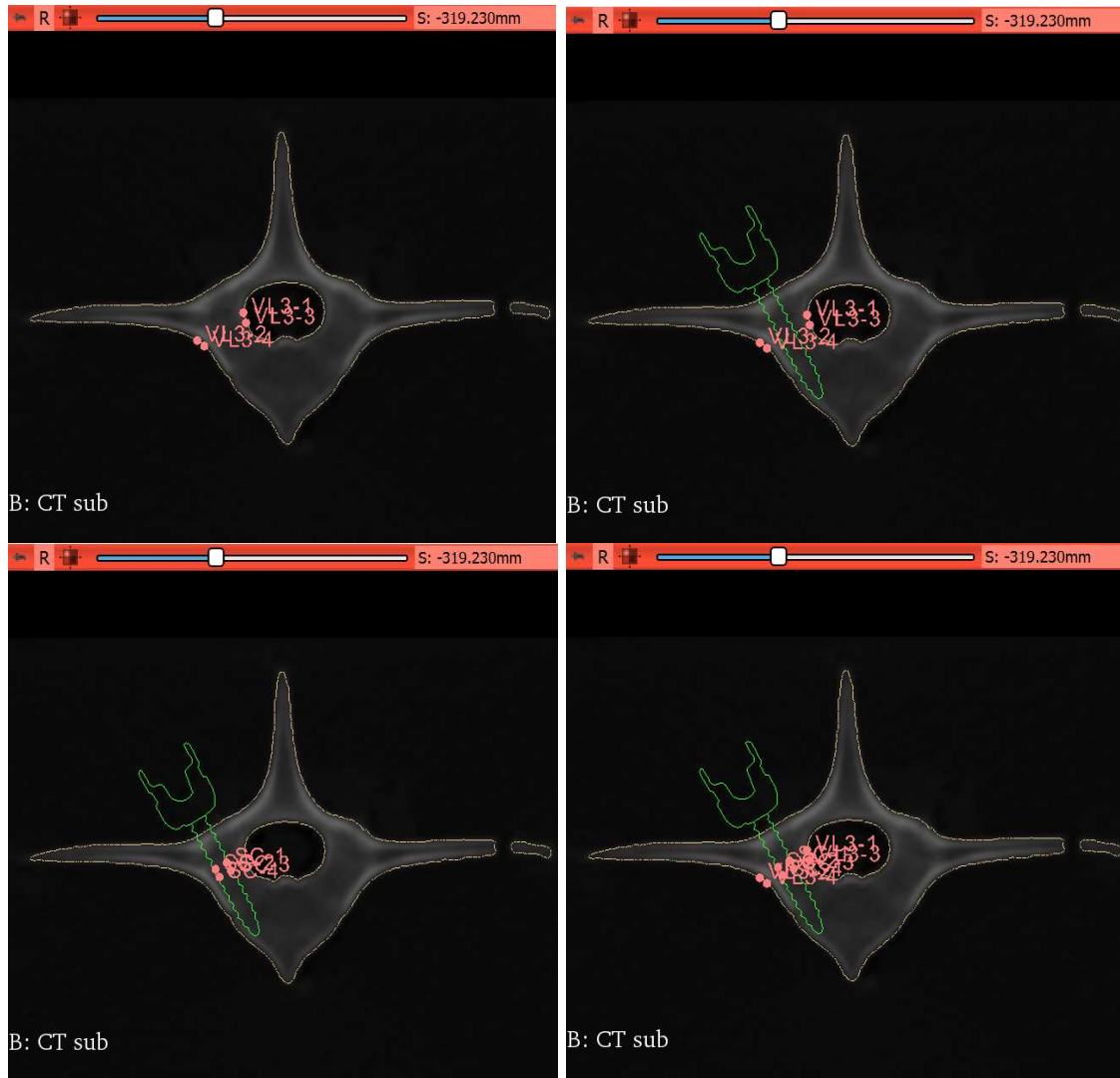


Fig 6. 6: Left axis view of left pedicle of vertebra 3: a) Top left: Landmarks on vertebra, b) Top right: Pedicle screw placed into vertebra, c) Bottom left: Translated Landmarks on pedicle screw, and d) Bottom right: Vertebra after the registration

Root mean square (RMS) Error = 4.42712

### Right Pedicle of Vertebra 3

$$\text{Rotation, } R = \begin{bmatrix} -0.88 & 0.49 & 0 \\ -0.47 & 0.88 & 0 \\ 0 & 0 & -1 \end{bmatrix} \quad \text{Translation, } t = \begin{bmatrix} 12.56 \\ -199.04 \\ -319.76 \end{bmatrix} \quad (6.11)$$

Angle in LR axis,  $\alpha = 27.76^\circ$ , Angle in SI axis,  $\gamma = 1.4^\circ$ ,

$$\text{Intersection point, } I = \begin{bmatrix} -25.28 \\ -174.88 \\ -319.76 \end{bmatrix} \quad (6.12)$$

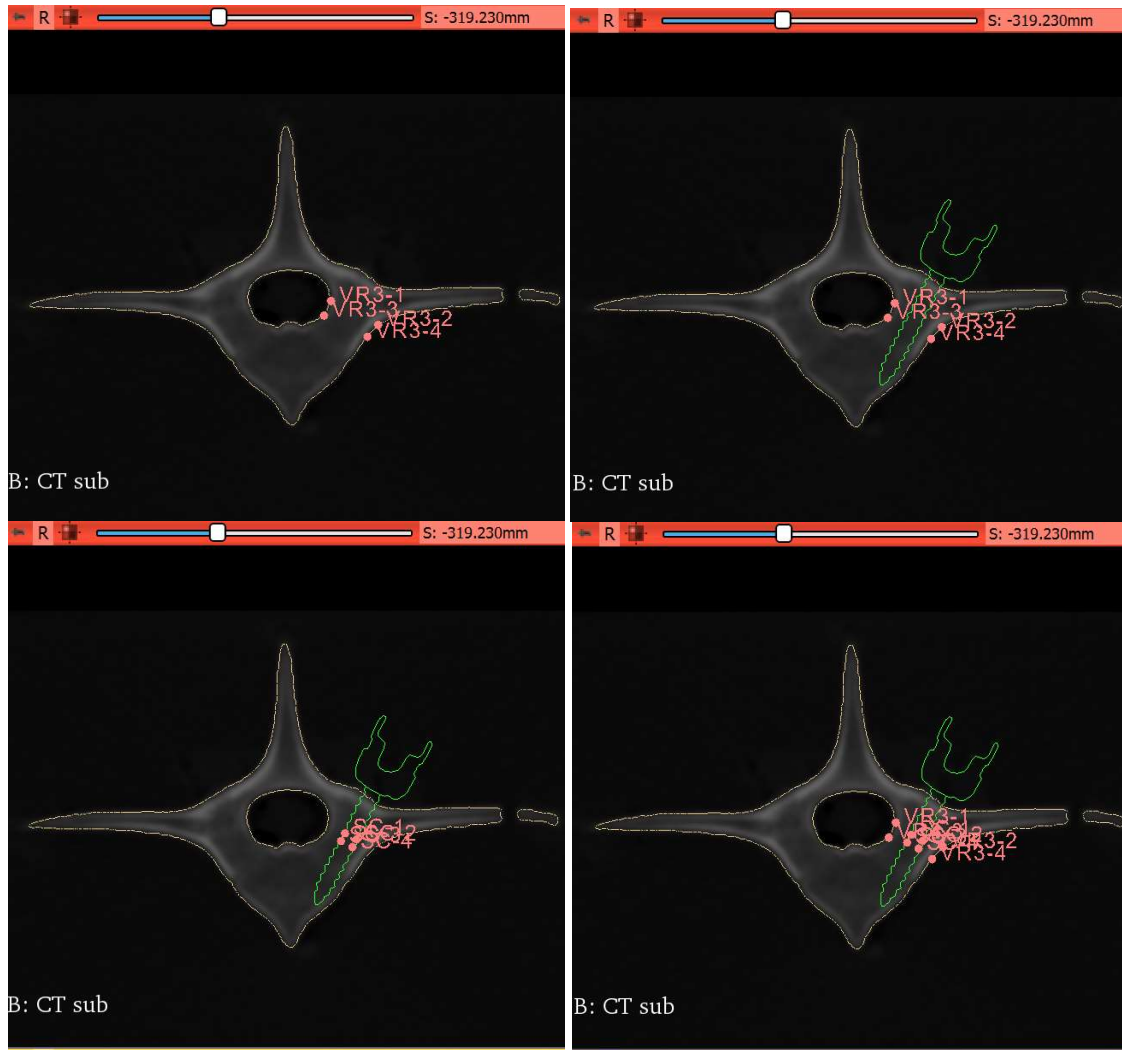


Fig 6. 7: Left axis view of right pedicle of vertebra 3: a) Top left: Landmarks on vertebra, b) Top right: Pedicle screw placed into vertebra, c) Bottom left: Translated Landmarks on pedicle screw, and d) Bottom right: Vertebra after the registration

Root mean square (RMS) Error = 4.44003

## Left Pedicle of Vertebra 4

$$\text{Rotation, } R = \begin{bmatrix} -0.84 & 0.55 & 0 \\ 0.55 & 0.84 & 0 \\ 0 & 0 & -1 \end{bmatrix} \quad \text{Translation, } t = \begin{bmatrix} -3.19 \\ -200.71 \\ -283.17 \end{bmatrix} \quad (6.13)$$

Angle in LR axis,  $\alpha = 33.28^\circ$ , Angle in SI axis,  $\gamma = 2.6^\circ$ ,

$$\text{Intersection point, } I = \begin{bmatrix} 11.41 \\ -178.47 \\ -283.17 \end{bmatrix} \quad (6.14)$$

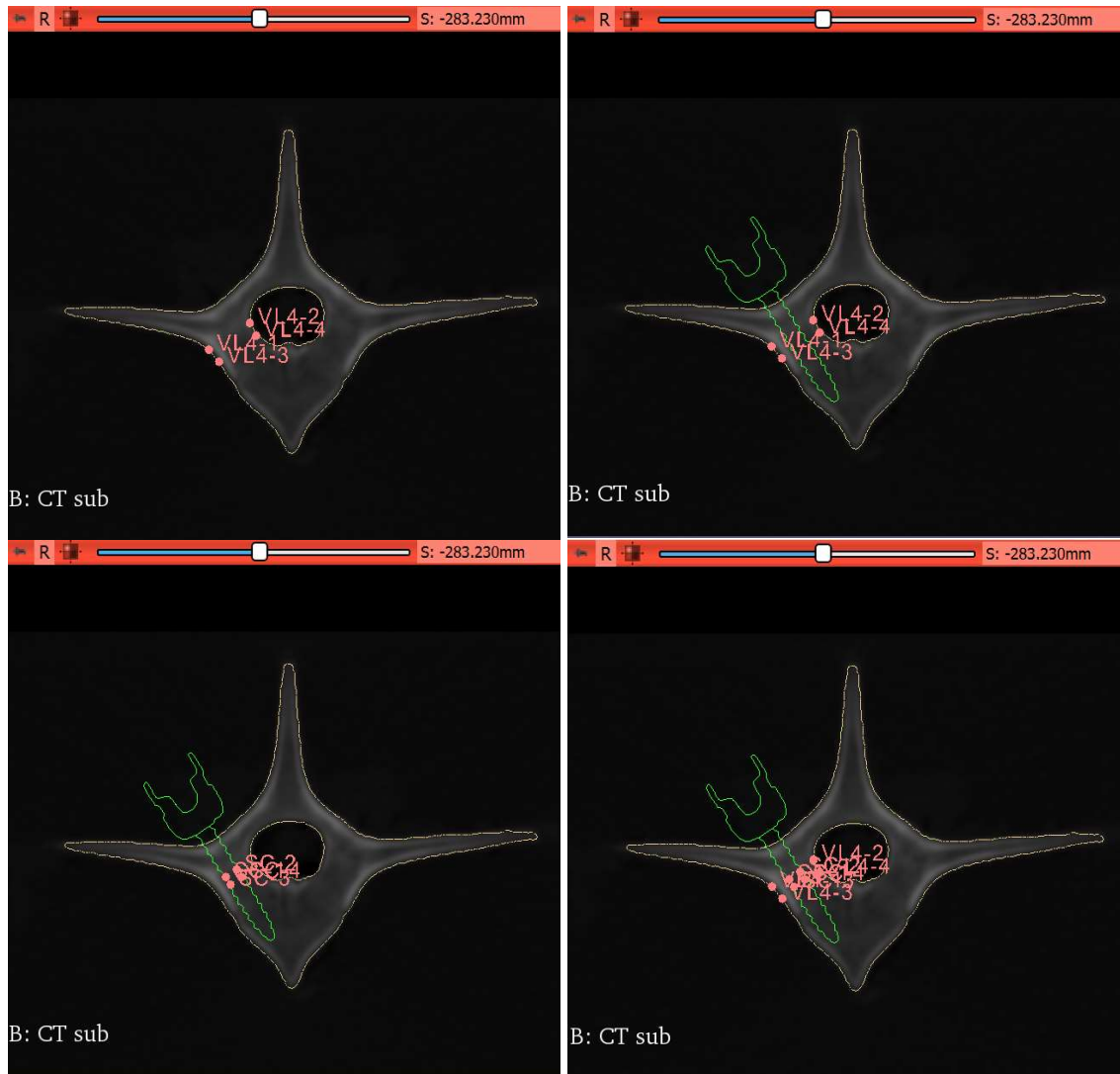


Fig 6. 8: Left axis view of left pedicle of vertebra 4: a) Top left: Landmarks on vertebra, b) Top right: Pedicle screw placed into vertebra, c) Bottom left: Translated Landmarks on pedicle screw, and d) Bottom right: Vertebra after the registration

Root mean square (RMS) Error = 3.99611

## Right Pedicle of Vertebra 4

$$\text{Rotation, } R = \begin{bmatrix} 0.90 & -0.43 & 0 \\ 0.43 & 0.90 & 0 \\ 0 & 0 & 1 \end{bmatrix} \quad \text{Translation, } t = \begin{bmatrix} -12.18 \\ -200.64 \\ -283.17 \end{bmatrix} \quad (6.15)$$

Angle in LR axis,  $\alpha = 25.38^\circ$ , Angle in SI axis,  $\gamma = 2.6^\circ$ ,

$$\text{Intersection point, } I = \begin{bmatrix} -23.50 \\ -176.79 \\ -283.17 \end{bmatrix} \quad (6.16)$$

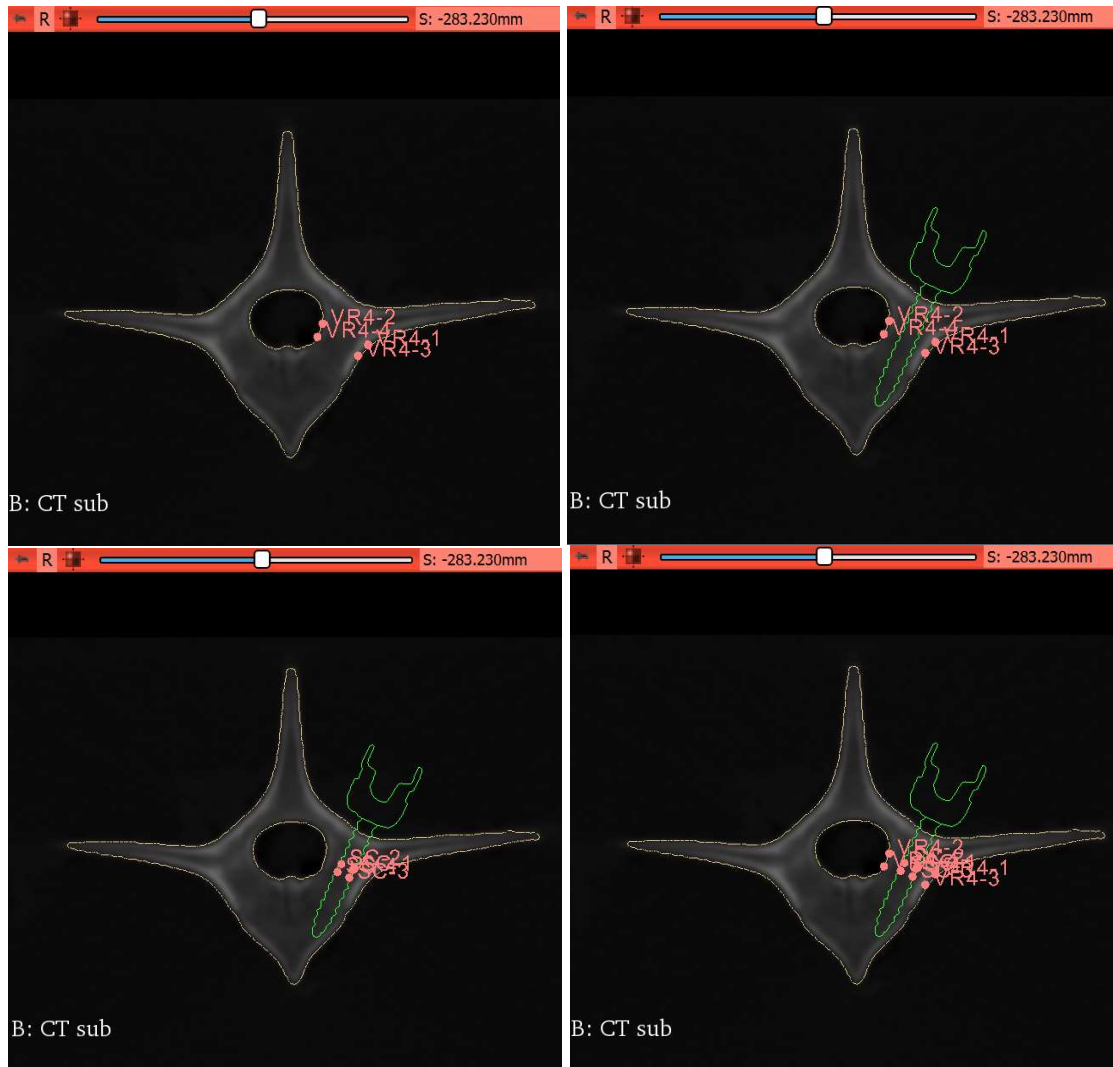


Fig 6. 9: Left axis view of right pedicle of vertebra 4: a) Top left: Landmarks on vertebra, b) Top right: Pedicle screw placed into vertebra, c) Bottom left: Translated Landmarks on pedicle screw, and d) Bottom right: Vertebra after the registration

Root mean square (RMS) Error = 4.08929

## Left Pedicle of Vertebra 5

$$\text{Rotation, } R = \begin{bmatrix} -0.86 & 0.50 & 0 \\ 0.50 & 0.86 & 0 \\ 0 & 0 & -1 \end{bmatrix} \quad \text{Translation, } t = \begin{bmatrix} -2.97 \\ -201.45 \\ -246.81 \end{bmatrix} \quad (6.17)$$

Angle in LR axis,  $\alpha = 30.21^\circ$ , Angle in SI axis,  $\gamma = 2.7^\circ$ ,

$$\text{Intersection point, } I = \begin{bmatrix} 9.61 \\ -179.84 \\ -246.81 \end{bmatrix} \quad (6.18)$$

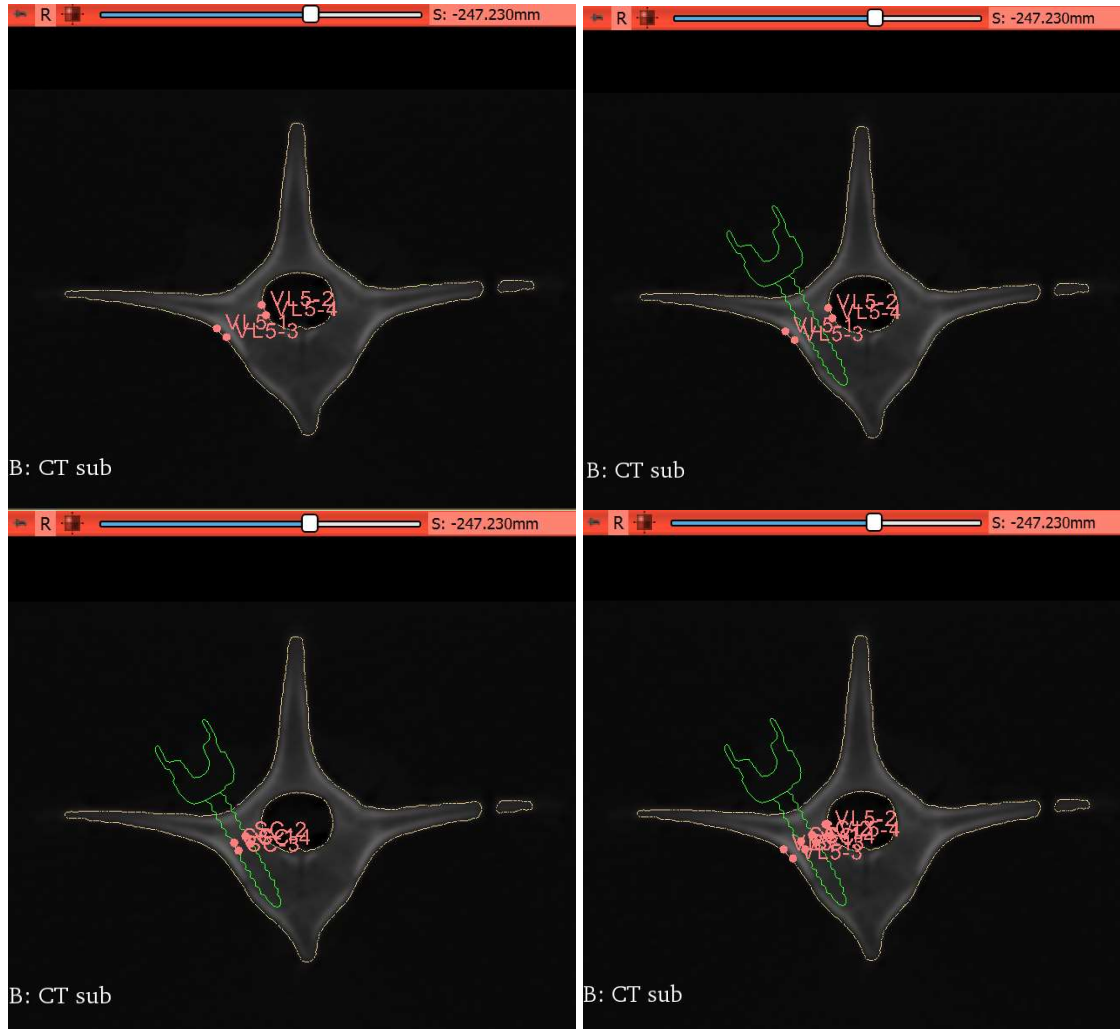


Fig 6. 10: Left axis view of left pedicle of vertebra 5: a) Top left: Landmarks on vertebra, b) Top right: Pedicle screw placed into vertebra, c) Bottom left: Translated Landmarks on pedicle screw, and d) Bottom right: Vertebra after the registration

Root mean square (RMS) Error = 4.00776

## Right Pedicle of Vertebra 5

$$\text{Rotation, } R = \begin{bmatrix} 0.89 & -0.46 & 0 \\ 0.46 & 0.89 & 0 \\ 0 & 0 & 1 \end{bmatrix} \quad \text{Translation, } t = \begin{bmatrix} -11.96 \\ -201.50 \\ -246.81 \end{bmatrix} \quad (6.19)$$

Angle in LR axis,  $\alpha = 27.33^\circ$ , Angle in SI axis,  $\gamma = 1.6^\circ$ ,

$$\text{Intersection point, } I = \begin{bmatrix} -23.99 \\ -178.22 \\ -246.81 \end{bmatrix} \quad (6.20)$$

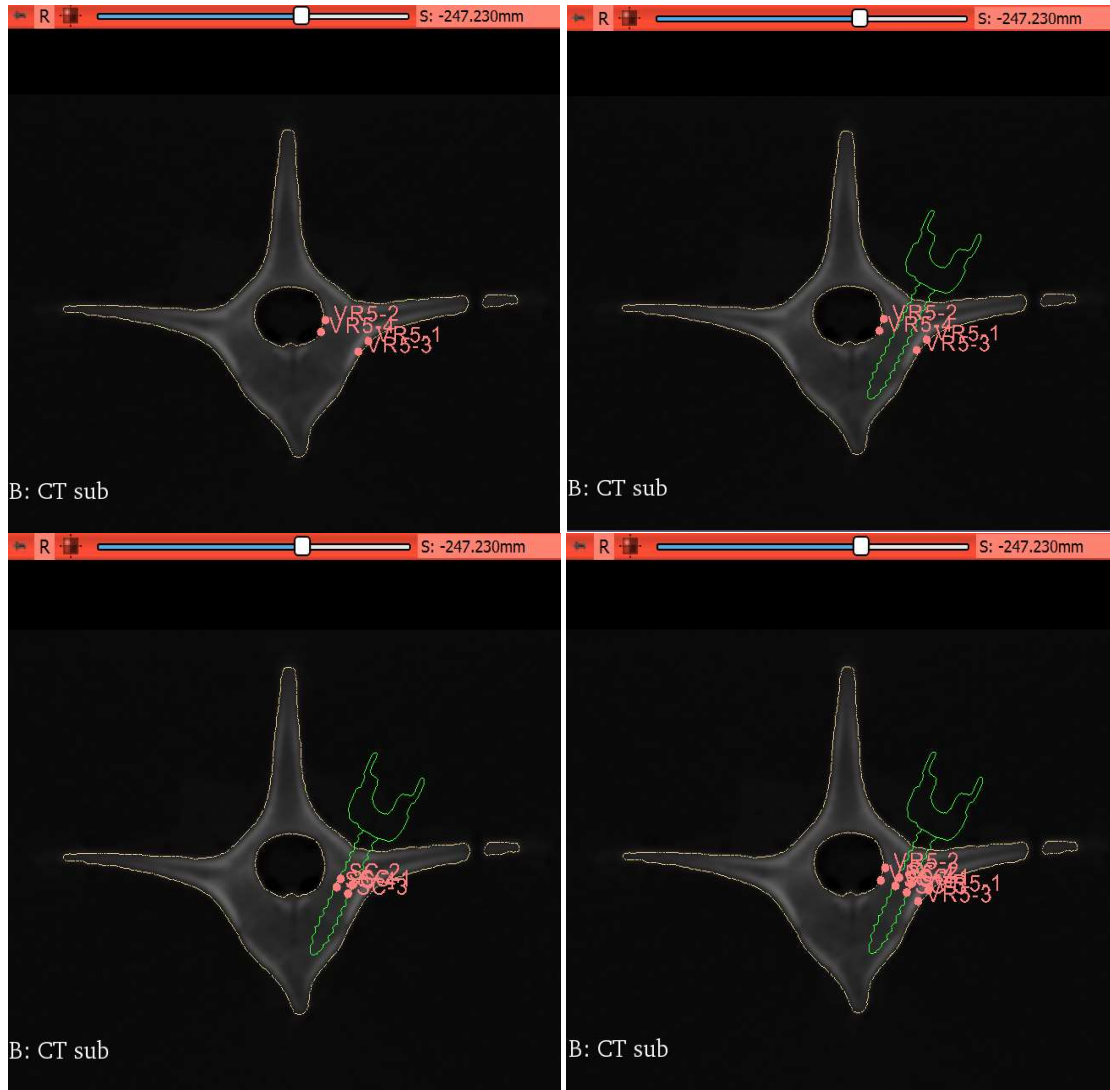


Fig 6. 11: Left axis view of right pedicle of vertebra 5: a) Top left: Landmarks on vertebra, b) Top right: Pedicle screw placed into vertebra, c) Bottom left: Translated Landmarks on pedicle screw, and d) Bottom right: Vertebra after the registration

Root mean square (RMS) Error = 3.78972

## Left Pedicle of Vertebra 6

$$\text{Rotation, } R = \begin{bmatrix} 0.93 & 0.38 & 0 \\ -0.38 & 0.93 & 0 \\ 0 & 0 & 1 \end{bmatrix} \quad \text{Translation, } t = \begin{bmatrix} -1.36 \\ -202.63 \\ -210.76 \end{bmatrix} \quad (6.21)$$

Angle in LR axis,  $\alpha = 22.08^\circ$ , Angle in SI axis,  $\gamma = 2.9^\circ$ ,

$$\text{Intersection point, } I = \begin{bmatrix} 7.17 \\ -181.88 \\ -210.76 \end{bmatrix} \quad (6.22)$$

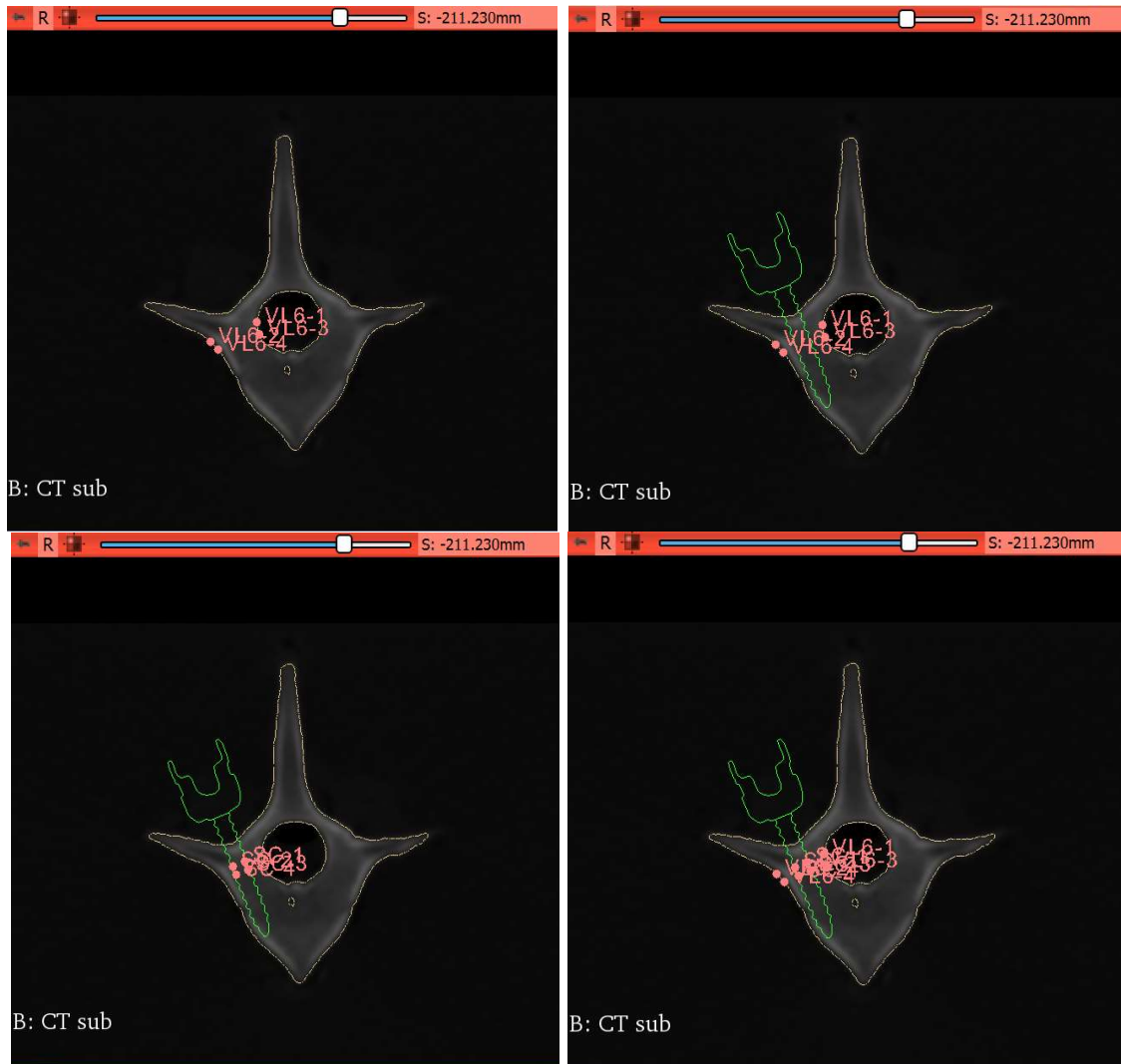


Fig 6. 12: Left axis view of left pedicle of vertebra 6: a) Top left: Landmarks on vertebra, b) Top right: Pedicle screw placed into vertebra, c) Bottom left: Translated Landmarks on pedicle screw, and d) Bottom right: Vertebra after the registration

Root mean square (RMS) Error = 4.04822

## Right Pedicle of Vertebra 6

$$\text{Rotation, } R = \begin{bmatrix} 0.97 & -0.25 & 0 \\ 0.25 & 0.97 & 0 \\ 0 & 0 & 1 \end{bmatrix} \quad \text{Translation, } t = \begin{bmatrix} -16.28 \\ -202.45 \\ -210.76 \end{bmatrix} \quad (6.23)$$

Angle in LR axis,  $\alpha = 14.2^\circ$ , Angle in SI axis,  $\gamma = 1.8^\circ$ ,

$$\text{Intersection point, } I = \begin{bmatrix} -22.05 \\ -179.67 \\ -210.76 \end{bmatrix} \quad (6.24)$$

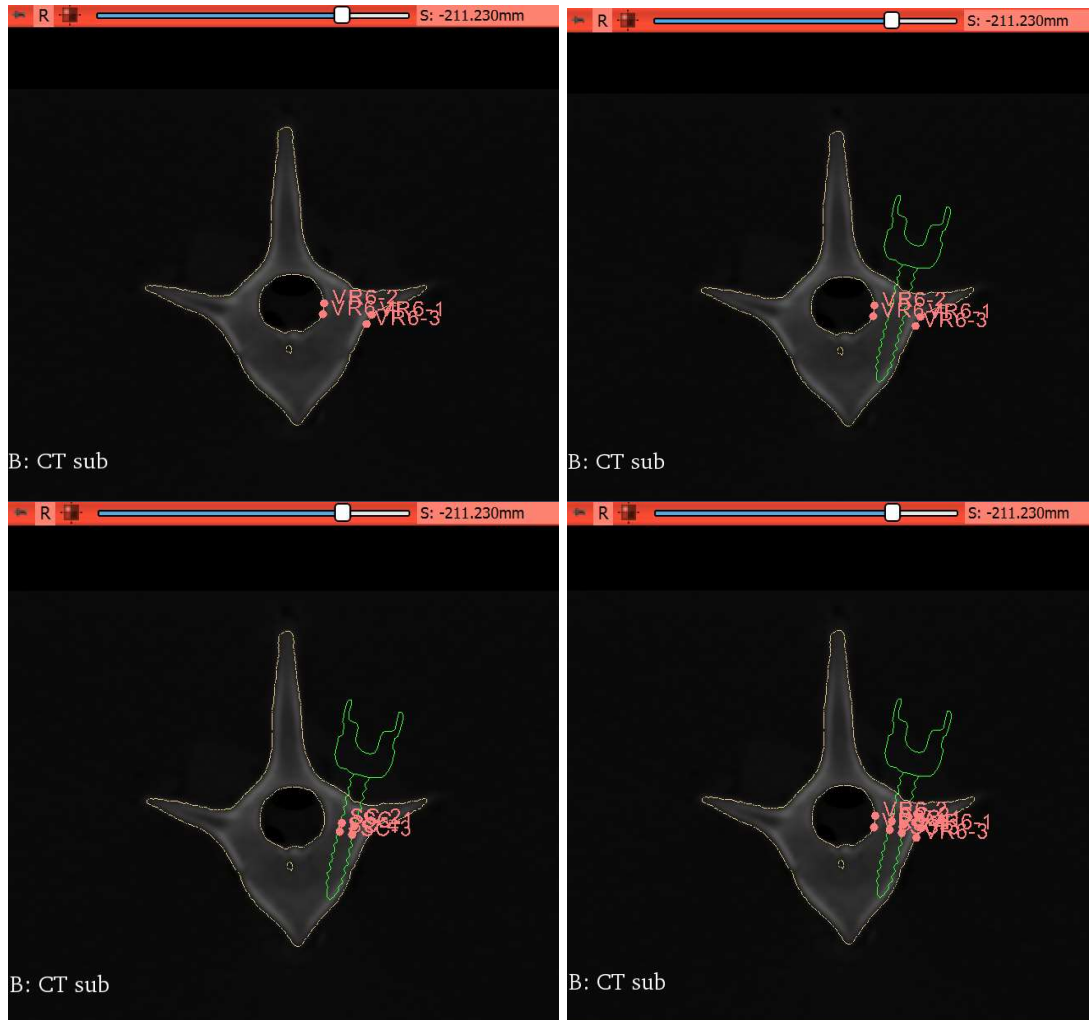


Fig 6. 13: Left axis view of right pedicle of vertebra 6: a) Top left: Landmarks on vertebra, b) Top right: Pedicle screw placed into vertebra, c) Bottom left: Translated Landmarks on pedicle screw, and d) Bottom right: Vertebra after the registration

Root mean square (RMS) Error = 3.99116

## Left Pedicle of Vertebra 7

$$\text{Rotation, } R = \begin{bmatrix} -0.91 & 0.42 & 0 \\ 0.42 & 0.91 & 0 \\ 0 & 0 & -1 \end{bmatrix} \quad \text{Translation, } t = \begin{bmatrix} -4.31 \\ -205.94 \\ -175.73 \end{bmatrix} \quad (6.25)$$

Angle in LR axis,  $\alpha = 24.72^\circ$ , Angle in SI axis,  $\gamma = 1.2^\circ$ ,

$$\text{Intersection point, } I = \begin{bmatrix} 5.64 \\ -184.32 \\ -175.73 \end{bmatrix} \quad (6.26)$$

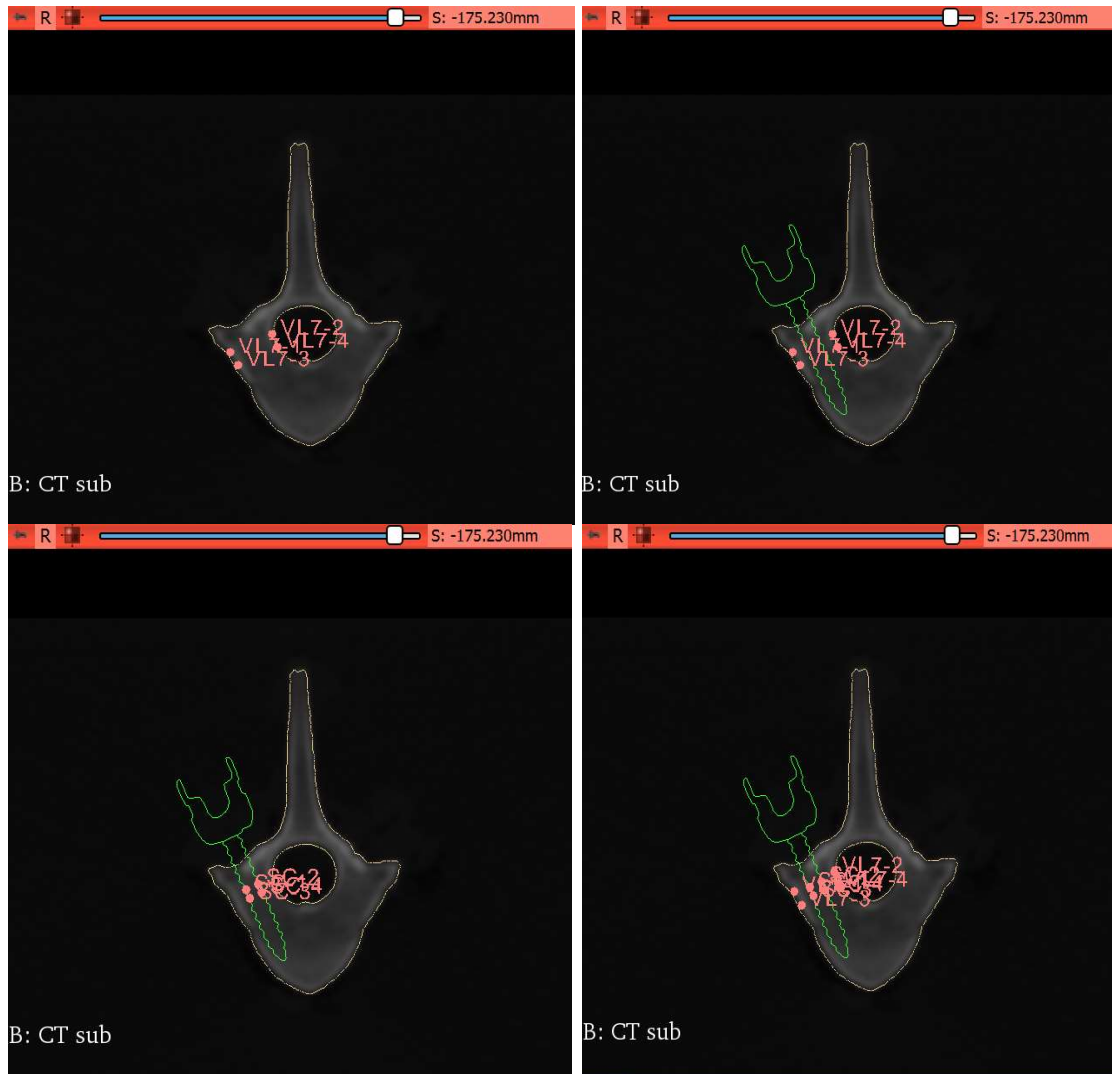


Fig 6. 14: Left axis view of left pedicle of vertebra 7: a) Top left: Landmarks on vertebra, b) Top right: Pedicle screw placed into vertebra, c) Bottom left: Translated Landmarks on pedicle screw, and d) Bottom right: Vertebra after the registration

Root mean square (RMS) Error = 3.63028

## Right Pedicle of Vertebra 7

$$\text{Rotation, } R = \begin{bmatrix} -0.94 & -0.34 & 0 \\ -0.34 & 0.94 & 0 \\ 0 & 0 & -1 \end{bmatrix} \quad \text{Translation, } t = \begin{bmatrix} -15.31 \\ -205.51 \\ -176.21 \end{bmatrix} \quad (6.27)$$

Angle in LR axis,  $\alpha = 19.8^\circ$ , Angle in SI axis,  $\gamma = 2.4^\circ$ ,

$$\text{Intersection point, } I = \begin{bmatrix} -23.1 \\ -183.87 \\ -176.21 \end{bmatrix} \quad (6.28)$$

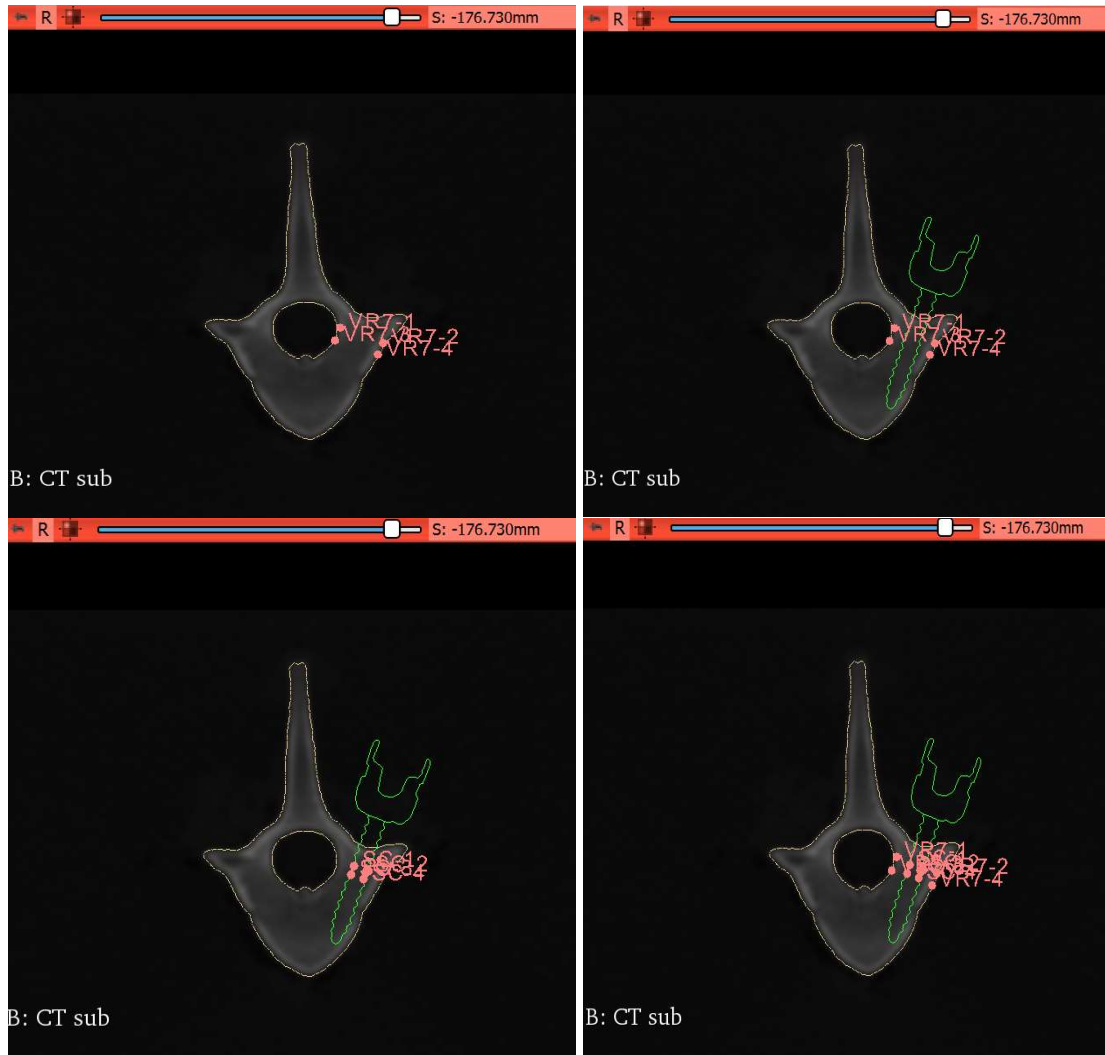


Fig 6. 15: Left axis view of right pedicle of vertebra 7: a) Top left: Landmarks on vertebra, b) Top right: Pedicle screw placed into vertebra, c) Bottom left: Translated Landmarks on pedicle screw, and d) Bottom right: Vertebra after the registration

Root mean square (RMS) Error = 3.71733

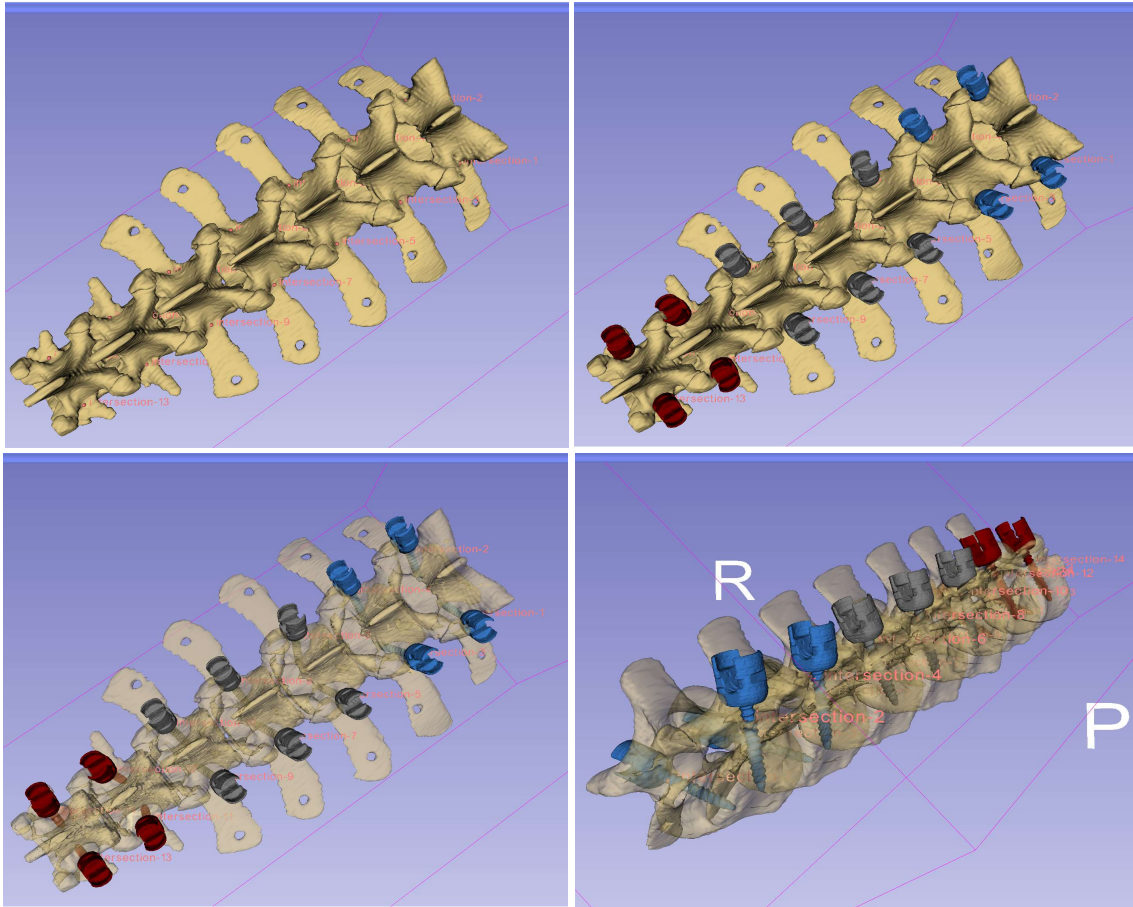


Fig 6. 16: a) Top left: intersection markups placed on vertebra in posterior view, b) Bottom left: Pedicle screw placed into semitransparent vertebra posterior view, c) Top right: Pedicle screw placed into vertebra posterior view, and d) Bottom right: Pedicle screw placed into semitransparent vertebra left view

### 6.1.2 Discussion

All of the pedicle screws were successfully mapped into the intraoperative coordinate frame. The registrations resulted the pedicle screws placed sufficiently accurately into the vertebra, where none of the screw perforated the pedicle walls. As the root mean square (RMS) error for each registration is pretty similar, around  $4 \pm 0.4$ . For all the vertebra, Fig (d) shows the placement of the translated landmarks on screw inside the pedicle. The result of this study is sufficient for satisfying our goal, the pedicle screws placement. As it is based on Closed form solution model [30], which provides absolute orientation to the least square problems by measuring the difference between the centroid of the coordinates in one system and the rotated and scaled centroid of the coordinates in the other system. In addition, the result agrees with the study done by Ungi et al.[40].

## 6.2 Registration between CT and US

The point to point base landmark registration is done between CT based virtual vertebral model (Fig 6.17a) and US imaging based virtual model of inverse image of vertebra (Fig 6.17b). Here, both models are for vertebra no 2 and 3 (table 4.1).

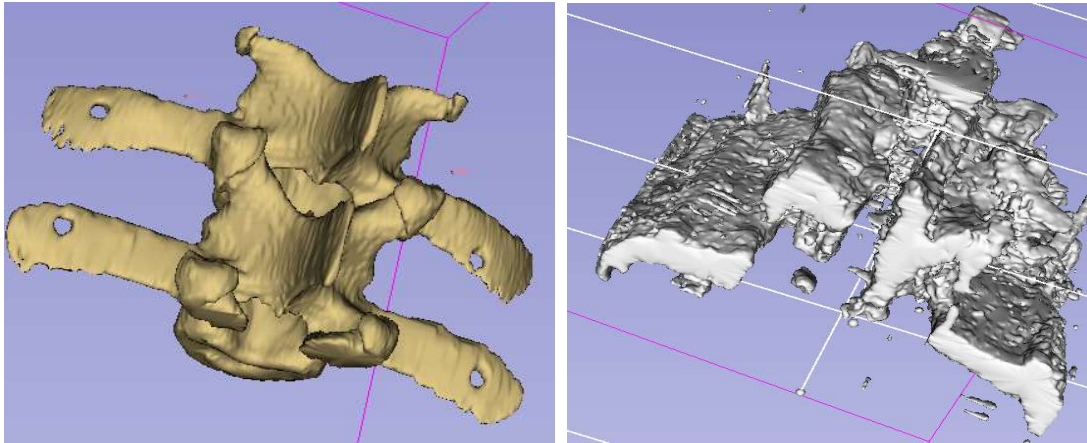


Fig 6. 17: Vertebra no 2 and 3: a) CT model, b) US model inverse image of the vertebra

The registration initiated by choosing six landmarks on top of the CT based vertebral model and six landmarks on bottom of the US imaging based vertebral model. Therefore, non-rigid landmarks registration was done between the landmarks of CT based vertebral model and the landmarks of US imaging based vertebral model. Here, landmarks on CT based vertebral model is moving reference and landmarks on US imaging based vertebral model is fixed reference.

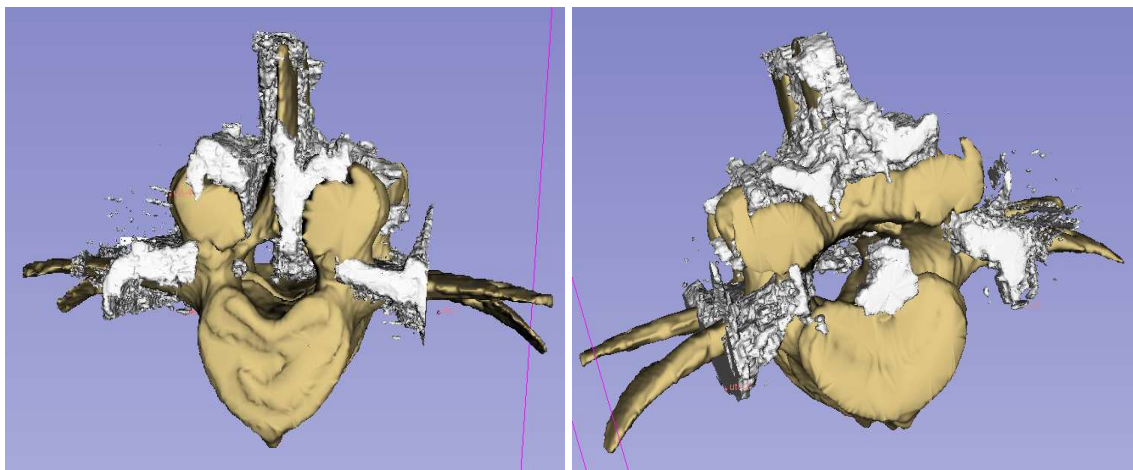


Fig 6. 18: Registration between CT model and US model: a) view from Superior axis, b) view from Inferior axis

The result of the registration is presented by rotation and transformation matrix and root mean square (RMS) error.

$$\text{Rotation, } R = \begin{bmatrix} 0.04 & 2.59 & 0.28 \\ -0.09 & 0.28 & -2.59 \\ -2.60 & 0.03 & 0.09 \end{bmatrix} \quad \text{Translation, } t = \begin{bmatrix} 365.62 \\ -1186.73 \\ 156.44 \end{bmatrix} \quad (6.29)$$

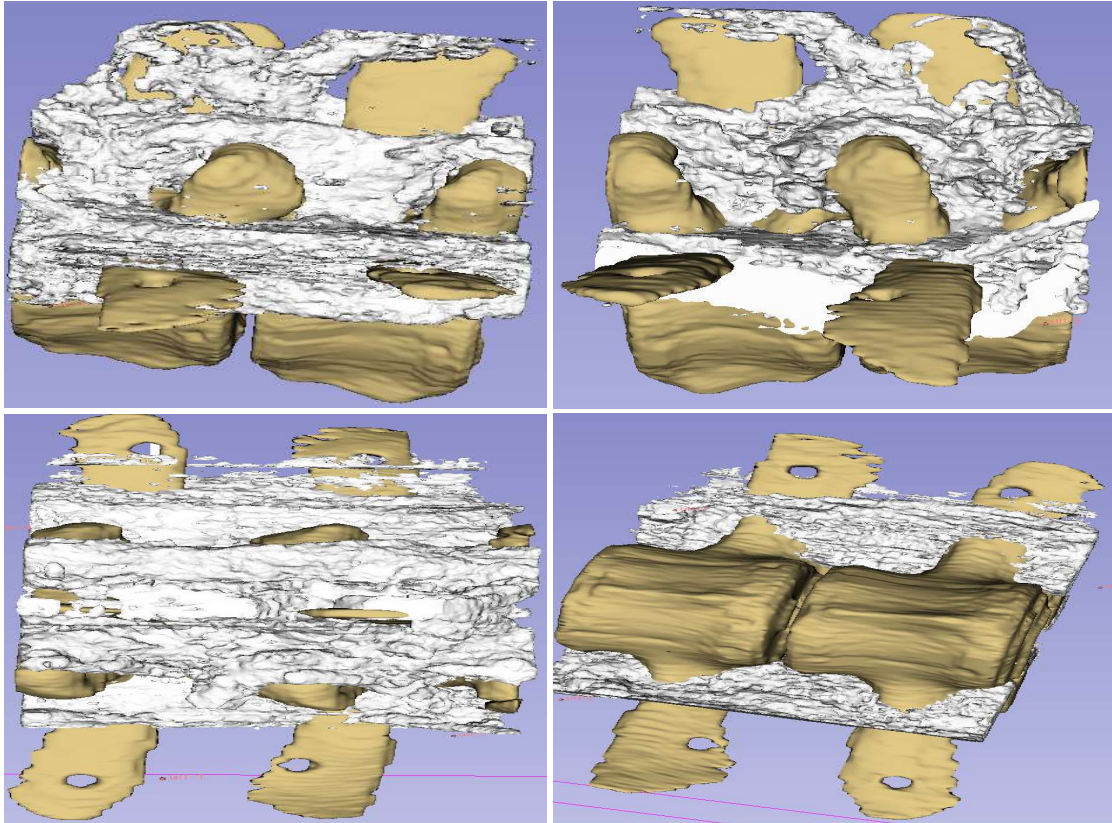


Fig 6. 19: Registration between CT model and US model: a) Top left: view from Left axis, b) Bottom left: view from Posterior axis, c) Top right: view from Right axis, and d) Bottom right: view from Anterior axis

Root mean square (RMS) Error = 20.645

### 6.1.2 Discussion

The transformation of the CT based vertebral model is represented by the resultant rotation and translation matrix. It is clearly seen in Fig 6.18 and 6.19 that CT based vertebral model and US imaging-based model of inverse image of vertebra is successfully registered and after the registration both the model match fairly. However, the RMS error is higher. It is due to ultrasound imaging are very noisy.

# Chapter 7

## Conclusions and Future Work

Image guided navigation improves the accuracy of minimally invasive pedicle screw placement during the surgery on spine. The navigation on spine surgery consists of 3D virtual model reconstruction of spine and real-time tracking of spine. While, with the help of virtual 3D model surgeon can make pre-operative planning and the real-time tracking allows surgeon to visualize current anatomy of patient's spine. This study aimed to establish a surgical navigation technique for pedicle screw placement in vertebrae. In particular, this study was designed to address two questions. First, how to reconstruct 3D virtual model of spine or vertebrae column? Second, can this study accurately able to map preoperative pedicle screw plans into the intraoperative coordinate frame into pedicle? With respect to the first question, CT and ultrasound imaging based 3d model of a pig column phantom was reconstructed using 3D slicer open-source software. For model reconstruction: CT images were acquired and cropped for getting region of interest (ROI) or vertebrae. After getting the cropped vertebrae, HU intensity values-based threshold segmentation was performed for constructing 3d virtual model of vertebrae. Since, CT imaging modality is the most suitable for bone detection and it enhances the compact bone contrast. Moreover, the HU intensity value of bone is higher in relation to the other soft tissues. In this study, CT based 3d model of vertebrae was constructed by segmenting with a HU intensity value ranging from 265 to 1300 as threshold. The same procedure was followed in constructing ultrasound-based model. However, ultrasound-based model is the inverse image of the vertebrae, as ultrasound does not pass through the bone, but reflected. With regard to the second question, all of the pedicle screws were successfully placed into the pedicles of vertebra, where none of the screw intersected the pedicle walls. Landmark registration was done between landmarks of pedicle screw and landmarks on pedicle of vertebra model developed from CT, where four landmarks were chosen respectively on pedicle screw and on pedicle of vertebrae. The registration result was sufficiently accurate, as the root mean square (RMS) error for each registration was around  $4 \pm 0.4$ . It was sufficient for satisfying our goal, the pedicle screws placement. In addition, this thesis produced similar results to that of Ungi et al.[40].

However, this study is not without limitation. First, landmarks on pedicle screw and pedicle of vertebra were initiated manually in landmark registration. It caused the registration affected by operator error. Future development in landmark registration should initiate landmarks automatically. Second, this study was done on pig spine which is similar, but not same as human spine. Additionally, this study is a theoretical approach, as no screws were physically placed on pig spine. I leave it to the future study where physical screw placement error will be considered. Although, the physical screw placement would reduce the accuracy of theoretical approach, it would be more reliable. Despite the fact that physical

placement error was not considered, this is a proof of concept study, where the results are adequate for making foundation to the future study.

## Bibliography

- [1] Image processing. [online], June 2018, <https://www.engineersgarage.com/articles/image-processing-tutorial-applications>
- [2] Digital image. [online], June 2017, <http://faraday.ee.emu.edu.tr/ee583/Lectures/EE%20583-Lecture01.pdf>
- [3] Gamma ray. [online], July 2018. [https://www.wikilectures.eu/w/Physical\\_principle\\_of\\_imaging\\_with\\_gamma-rays](https://www.wikilectures.eu/w/Physical_principle_of_imaging_with_gamma-rays)
- [4] X-ray. [online], July 2018. <https://en.wikipedia.org/wiki/X-ray>
- [5] Microwave imaging. [online], July 2018. [https://en.wikipedia.org/wiki/Microwave\\_imaging](https://en.wikipedia.org/wiki/Microwave_imaging)
- [6] Infrared. [online], July 2018. <https://en.wikipedia.org/wiki/Infrared>
- [7] Radio frequency. [online], June 2018. [https://en.wikipedia.org/wiki/Radio\\_frequency](https://en.wikipedia.org/wiki/Radio_frequency)
- [8] Ultrasound. [online], September 2018. <https://en.wikipedia.org/wiki/Ultrasound>
- [9] History of medical imaging. [online], July 2018. <https://www.itnonline.com/article/eclectic-history-medical-imaging>
- [10] Anatomy of the spine. [online], August 2018. <https://mayfieldclinic.com/pe-anat spine.htm>
- [11] History of ultrasound. [online], August 2018. <https://www.livescience.com/32071-history-of-fetal-ultrasound.html>
- [12] Ultrasound. [online], August 2018. <https://science.howstuffworks.com/ultrasound1.htm>
- [13] Ultrasonography. [online], August 2018. <http://www.vetfolio.com/diagnostics/basic-principles-of-ultrasonography>
- [14] DICOM. [online], July 2018. <https://www.dicomstandard.org/>
- [15] DICOM history. [online], July 2018. <https://www.dicomstandard.org/history/>
- [16] DICOM. [online], June 2018. <https://en.wikipedia.org/wiki/DICOM>
- [17] Morphological image processing. [online], July 2018. <https://www.dspguide.com/ch25/4.htm>
- [18] Image processing. [online], August 2018. <https://www.cs.auckland.ac.nz/courses/compsci773s1c/lectures/ImageProcessing.html/topic4.htm>
- [19] Kaur, D., Kaur, Y. "Various Image Segmentation Techniques: A Review". International Journal of Computer Science and Mobile Computing, Vol.3, Issue. 5, pp 809-814, ISSN 2320-088X.
- [20] Image registration. [online], September 2018. <https://www.sciencedirect.com/topics/neuroscience/image-registration>
- [21] Image registration. [online], September 2018. [https://en.wikipedia.org/wiki/Image\\_registration](https://en.wikipedia.org/wiki/Image_registration)
- [22] Image registration. [online], October 2018. <https://www.comp.nus.edu.sg/~cs4243/lecture/register.pdf>
- [23] A. Ardeshir Goshtasby: 2-D and 3-D Image Registration for Medical, Remote Sensing, and Industrial Applications, Wiley Press, 2005, ISBN: 978-0-471-64954-0.

- [24] Francisco Paulo Marques de Oliveira. Emparelhamento e alinhamento de estruturas em visão computacional: Aplicações em imagens médicas. Master's thesis, Faculdade de Engenharia da Universidade do Porto, 2008/2009.
- [25] Yuheng, S., Hao, Y. Image Segmentation Algorithms Overview, SiChuan University, Sichuan, ChengDu. <https://arxiv.org/ftp/arxiv/papers/1707/1707.02051.pdf>
- [26] Medical imaging. [online], July 2018. <https://www.fda.gov/radiation-emittingproducts/radiationemittingproductsandprocedures/medicalimaging/ucm115357.htm>
- [27] 3D model. [online], June 2018. <https://formlabs.com/blog/3d-printed-medical-models/>
- [28] Dias, J. M. R. S., Sistema de Navegação Cirúrgico para Colocação de Parafusos Pediculares, Internship report, Instituto Superior Técnico of Lisbon, Portugal, 2014
- [29] Teodoro, P. D. D., Robust Surface Reconstruction and US Bone Registration for Hip Resurfacing Surgery, PhD Thesis, Instituto Superior Técnico of Lisbon, Portugal, 2015
- [30] Horn, B.K.P., Closed-form solution of absolute orientation using unit quaternions, Journal Optical Society America, Vol. 4, No. 4, April 1987, Page 629-642.
- [31] Ashburner, J. and Friston, K. J., Rigid Body Registration, Chapter 2. <https://www.fil.ion.ucl.ac.uk/spm/doc/books/hbf2/pdfs/Ch2.pdf>
- [32] Sorkine-Hornung, O. and Rabinovich, M. Least-squares Rigid Motion using SVD. Department of Computer Science, ETH Zurich, page 1-5, January 2017.
- [33] Affine registration. [online], September 2018. <http://pages.stat.wisc.edu/~mchung/teaching/768/reading/lecture06-affine.pdf>
- [34] Image registration. [online], October 2018. [http://www.fis.uc.pt/data/20072008/apontamentos/apnt\\_177\\_0.pdf](http://www.fis.uc.pt/data/20072008/apontamentos/apnt_177_0.pdf)
- [35] Hao, L., Rpbert, W.S., and Mark, P. Global Correspondence Optimization for Non-Rigid Registration of Depth Scans. Eurographics Symposium on Geometry Processing 2008, Pierre Alliez and Szymon Rusinkiewicz (Guest Editors), Vol 27, no 5.
- [36] Non-rigid registration. [online], September 2018. [http://resources.mpi-inf.mpg.de/deformableShapeMatching/EG2011\\_Tutorial/slides/2.3%20Non-Rigid%20Registration.pdf](http://resources.mpi-inf.mpg.de/deformableShapeMatching/EG2011_Tutorial/slides/2.3%20Non-Rigid%20Registration.pdf)
- [37] Mark Holden Derek L G Hill, Philipp G Batchelor and David J Hawkes. Medical image registration. Technical Report 46, INSTITUTE OF PHYSICS PUBLISHING, 2000.
- [38] Surgical navigation systems. [online], July 2018. <http://www.medtronic.com/us-en/healthcare-professionals/products/neurological/surgical-navigation-systems/stealthstation.html>
- [39] G Widmann, Image-guided surgery and medical robotics in the cranial area. Biomed Imaging Interv J. 2007 Jan-Mar; 3(1): e11.
- [40] Ungi, T. and Schwab H., J. Tracked Ultrasound Snapshots in Percutaneous Pedicle Screw Placement Navigation: A Feasibility Study. Clinical Orthopedics Related Research (2013) 471:4047–4055 DOI 10.1007/s11999-013-3239-5
- [41] Computed tomography. [online], August 2018. <https://www.nibib.nih.gov/science-education/science-topics/computed-tomography-ct>
- [42] J. R. Caldas Pinto. Components of a vision system. [Online], first semester 2016.
- [43] Patricia Figueiredo. Biomedical imaging. [Online], <https://fenix.tecnico.ulisboa.pt/downloadFile/282093452002431/04-MI-MEBiom-US.pdf>.

- [44] Krzysztof Iniewski. MEDICAL IMAGING, Principles, Detectors, and Electronics. John Wiley Sons, 2009.
- [45] Richmond, Caroline (2004). "Obituary – Sir Godfrey Hounsfield". BMJ. 329 (7467): 687. doi:10.1136/bmj.329.7467.687
- [46] Dr J.M. Rocchisani. Medical imaging. Sorbonne Paris Cité, November 2016.
- [47] Brief history of ct. [Online], July 2018. <http://www.impactscan.org/CThistory.htm>
- [48] A. M. Cormack. Representation of a function by its line integrals, with some radiological applications. Journal of Applied Physics, 34(9):2722-2727, 1963.
- [49] A. M. Cormack. Representation of a function by its line integrals, with some radiological applications. ii. Journal of Applied Physics, 35(10):2908-2913, 1964.
- [50] Image processing. [online], October 2018. <https://sisu.ut.ee/imageprocessing/book/1>
- [51] Andre Sales Cunha Peres. Desenvolvimento de protocolos de neuronavegação para estudos de estimulação magnética transcraniana e suas aplicações em voluntários controlados e pacientes com acidente vascular cerebral. PhD thesis, Faculdade de filosofia de ciencias e letras de Ribeirão Preto, 2012.
- [52] Daniel Rueckert and Paul Aljabar. Non-rigid registration of medical images: Theory, methods and applications. Technical report. Available: <http://citeseerx.ist.psu.edu/viewdoc/download?doi=10.1.1.465.1968&rep=rep1&type=pdf>.
- [53] History of ultrasound. [online], August 2018. <https://www.ultrasound-schools-info.com/history/>



## Picture Reference

- (1) [online], July 2018. [http://www.pinsdaddy.com/dot-line-screen\\_9jYSKxG5t5m\\*8BuQK%7CSZyZaosqSwGbRrp2pqKGj0nwg/](http://www.pinsdaddy.com/dot-line-screen_9jYSKxG5t5m*8BuQK%7CSZyZaosqSwGbRrp2pqKGj0nwg/)
- (2) [online], August 2018. [https://link.springer.com/chapter/10.1007/978-1-4471-4850-0\\_35](https://link.springer.com/chapter/10.1007/978-1-4471-4850-0_35)
- (3) [online], August 2018. <http://www.arcsoft.com/topics/photostudio-darkroom/what-is-color-space.html>
- (4) [online], August 2018. <https://www.quora.com/How-does-a-CT-scan-work-Does-it-mean-a-group-of-x-rays-What-is-the-use-of-a-CT-scan-Where-is-it-used>
- (5) [online], September 2018. [https://www.researchgate.net/figure/1-X-ray-attenuation-of-single-and-multi-component-materials\\_fig1\\_300815290](https://www.researchgate.net/figure/1-X-ray-attenuation-of-single-and-multi-component-materials_fig1_300815290)
- (6) [online], September 2018. <https://www.cmu.edu/me/xctf/xrayct/index.html>
- (7) [online], September 2018. <https://www.shutterstock.com/search/vertebrae>
- (8) [online], September 2018. <https://en.wikipedia.org/wiki/Vertebra>
- (9) [online], September 2018. [https://www.ncbi.nlm.nih.gov/books/NBK363066/figure/CDR0000774255\\_\\_392/](https://www.ncbi.nlm.nih.gov/books/NBK363066/figure/CDR0000774255__392/)
- (10) [online], September 2018. <https://web.eecs.umich.edu/~fessler/course/516//cu-ultra.pdf>
- (11) [online], September 2018. <https://www.cs.auckland.ac.nz/courses/compsci773s1c/lectures/ImageProcessing-html/topic4.htm>
- (12) [online], October 2018. <http://dev.biologists.org/content/139/17/3071>
- (13) [online], October 2018. <https://epsil.github.io/fisheye/>
- (14) [online], October 2018. <http://www.hao-li.com/teaching/geometricComputingSeminar/IntroductionToNonRigidRegistration.pdf>
- (15) [online], October 2018. [https://www.cs.cmu.edu/~galeotti/methods\\_course/DeformableRegistration.pdf](https://www.cs.cmu.edu/~galeotti/methods_course/DeformableRegistration.pdf)